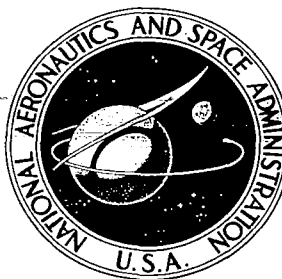


**NASA CONTRACTOR
REPORT**

NASA CR-1655



NASA CR-1655

LOAN COPY: RETURN TO
AFWL (WLOL)
KIRTLAND AFB, N MEX

**PROBING THE SOLAR CORONA
WITH SPACECRAFT RADIO SIGNALS**

by W. Wells, R. Marquedant, and H. Hodara

Prepared by

TETRA TECH, INC.

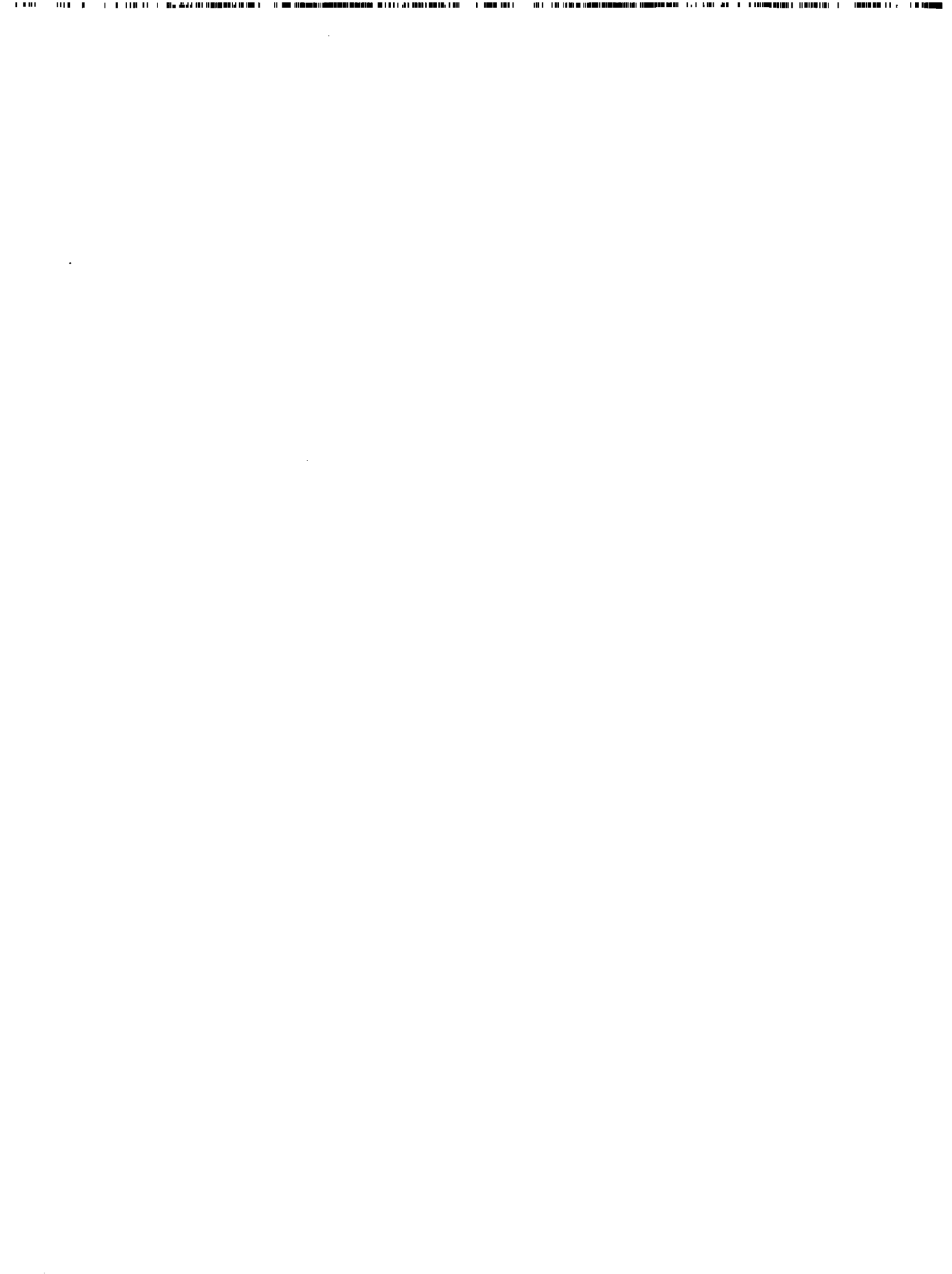
Pasadena, Calif. 91107

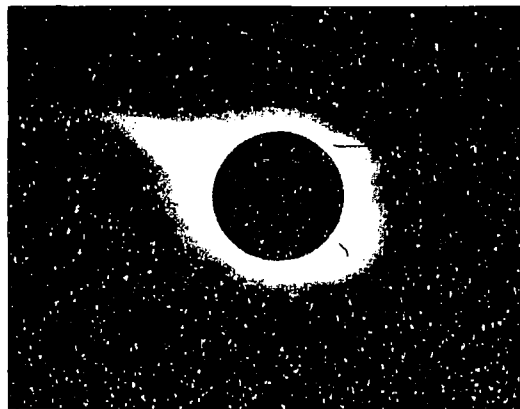
for Langley Research Center



0060878

| | | | | | |
|---|--|--|--|--|--|
| 1. Report No. NASA CR-1655 | | 2. Government Accession No. | | 3. Recipient's Catalog No. | |
| 4. Title and Subtitle PROBING THE SOLAR CORONA WITH SPACECRAFT RADIO SIGNALS | | | | 5. Report Date October 1970 | |
| | | | | 6. Performing Organization Code | |
| 7. Author(s) W. Wells, R. Marquedant, and H. Hodara | | | | 8. Performing Organization Report No. TC-163 | |
| 9. Performing Organization Name and Address Tetra Tech, Incorporated 630 North Rosemead Boulevard Pasadena, California 91107 | | | | 10. Work Unit No. 856-10-00-01-23 | |
| 12. Sponsoring Agency Name and Address National Aeronautics and Space Administration Washington, D.C. 20546 | | | | 11. Contract or Grant No. NAS 1-9167 | |
| | | | | 13. Type of Report and Period Covered Contractor Report | |
| | | | | 14. Sponsoring Agency Code | |
| 15. Supplementary Notes | | | | | |
| 16. Abstract The cancelled MIT Sunblazer program was reviewed to see if a mission of this general type should be performed especially with the Scout booster, and if so, how it should differ from Sunblazer. Review of present knowledge of the corona shows that the region near the Sun (a few solar radii) and the direction out of the ecliptic plane should be probed. Large scale density and velocity structure should be studied, and an attempt made to see whether the solar wind originates in small disturbances or large areas of the Sun's surface. Radio links were analyzed as were the connections between measurable radio parameters and their information content regarding the corona, its structures and parameters. As a result the use of two microwave carrier frequencies is recommended, probably S- and X-band, but no lower frequency than S-band. An uplink propagation experiment (like the Stanford Pioneer VII) followed by data reduction on the spacecraft and downlink telemetry seems preferable to insure reception with a strong signal-to-noise ratio. However, factors beyond the scope of this study could alter this conclusion in favor of a downlink, which greatly simplifies the craft and gives raw data at multiple ground stations. A novel passive attitude control scheme for spin-stabilized spacecraft is recommended for this mission. The spin axis points stably toward the Sun, but lags slightly in following the Sun's apparent angular movement. Sun sensors can give instantaneous roll angle if this information is desired. The required torque derives from solar pressure acting on vanes that are fixed with respect to the craft. <i>1. Solar Corona</i> | | | | | |
| 17. Key Words (Suggested by Author(s)) Solar propagation 2. Radio astronomy Solar occultation experiment Solar plasma effects | | | | 18. Distribution Statement Unclassified - Unlimited | |
| 19. Security Classif. (of this report) Unclassified | | 20. Security Classif. (of this page) Unclassified | | 21. No. of Pages 160 | |
| | | | | 22. Price* \$3.00 | |





The Solar Corona, 31 August 1932. Near sunspot minimum corona has short curved polar streamers and long equatorial extensions. (Photo by P. A. McNally, Georgetown College Observatory)



The Solar Corona, 12 November 1966. Also Venus appears overexposed northeast of the Sun. (High Altitude Observatory)

Frontispiece. The Solar Corona appears to launch streams of hot gas into interplanetary space.

TABLE OF CONTENTS

| | |
|--|-----|
| Introduction | 1 |
| Conclusions and Recommendations | 10 |
| Present Knowledge of the Solar Corona | 15 |
| Spacecraft Radio Propagation Experiments | 35 |
| Relating Radio Measurements to Corona Properties | 51 |
| Propagation Link Analysis | 73 |
| Critique of the MIT Sunblazer Study | 123 |
| Passive Spacecraft Attitude Control | 129 |
| Recommended Mission | 141 |
| Appendix 1 | 143 |
| Appendix 2 | 146 |
| Appendix 3 | 148 |
| Appendix 4 | 150 |
| Appendix 5 | 152 |
| References | 154 |

INTRODUCTION

The original aim of the Sunblazer program is illustrated in Fig. 1. The radio signal propagating along the line-of-sight from spacecraft to Earth can probe much closer to the Sun than any spacecraft can. To probe closely the Sunblazer does not have to withstand intense heat nor does it have to be propelled with an unusually high impulse to overcome the centrifugal potential barrier (i. e., remove Earth's orbital velocity and fall in close to the Sun). Instead, the impulse removes only a fraction of the Earth's orbital velocity, and the craft falls into an elliptical orbit with a period shorter than a year, such as the 3/4-year orbit that MIT selected. The relative motion between spacecraft and Earth then has the frequency of the "beat" between the two orbital rates ($4/3$ orbit/year - 1 orbit/year = $1/3$ orbit/year). The superior conjunction, when the spacecraft passes behind the Sun, occurs after a half period of the beat frequency ($\frac{1}{2} \times 3$ years/relative orbit = 1.5 years = 18 months).

Figures 2 and 3 show two 3/4-year orbits with 18 months to conjunction, one for July launch and one for December (near the time of Earth's aphelion and perihelion respectively). These orbits, reproduced from the Sunblazer report, are in a rotating coordinate system in which the Sun and Sun-Earth line are fixed. Each loop occurs at the spacecraft's aphelion. By putting one of these loops behind the Sun, the MIT orbit achieves the advantage of a triple conjunction as illustrated in the solar encounter profile view above each orbit diagram. Triple conjunction prolongs the important period in which the Sun-Earth line-of-sight probes the region close to the Sun. The way these orbits are projected on the paper, West is on the right and North is down in the encounter profile view. Each dot represents ten days. From a purely orbital point of view, the July launch is superior, because the probe spends slightly more time behind the Sun. However, this puts conjunction in January, so the conjunction experiments would take place in the winter when the Sun is low in the sky and days are short, unless the tracking stations are in the Southern Hemisphere. For this reason a December or February launch is probably preferable. The February launch orbit looks much like the December, except the orbit loop is near the East limb of the Sun instead of the West. January launch is poor because the orbit loop is mostly occulted by the Sun's disc.

The distance denoted by b in Fig. 1 is very important to our analysis and discussions, because it is the distance from the Sun to the part of the corona which is densest and therefore has the strongest effect on radio propagation. This distance has been called "impact parameter," "solar elongation," "path offset" and probably other names. We call it "path offset," adhere to the symbol b , and follow the convention of measuring it in solar radii, 696 Mm, which we shall abbreviate "solrad." We also use "solrad" to denote the angle ϵ in units of 0.266° , the angular radius of the Sun as seen from Earth.

Probing the corona with radio signals is not new; we review experiments in which probing was accomplished with celestial radio sources

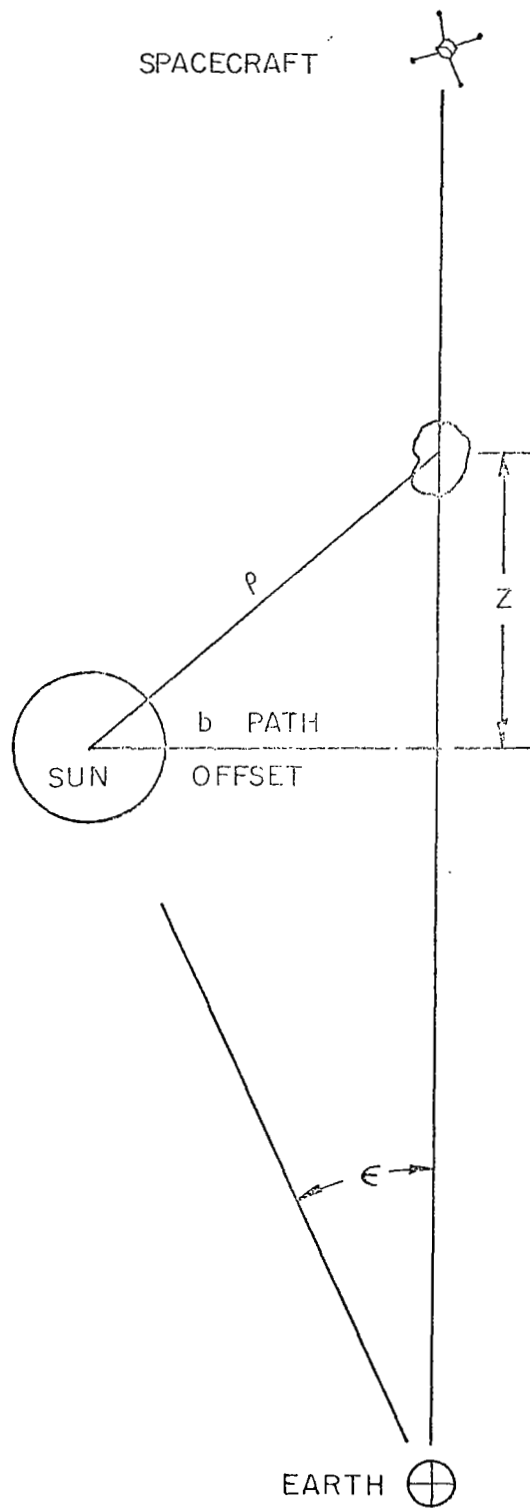
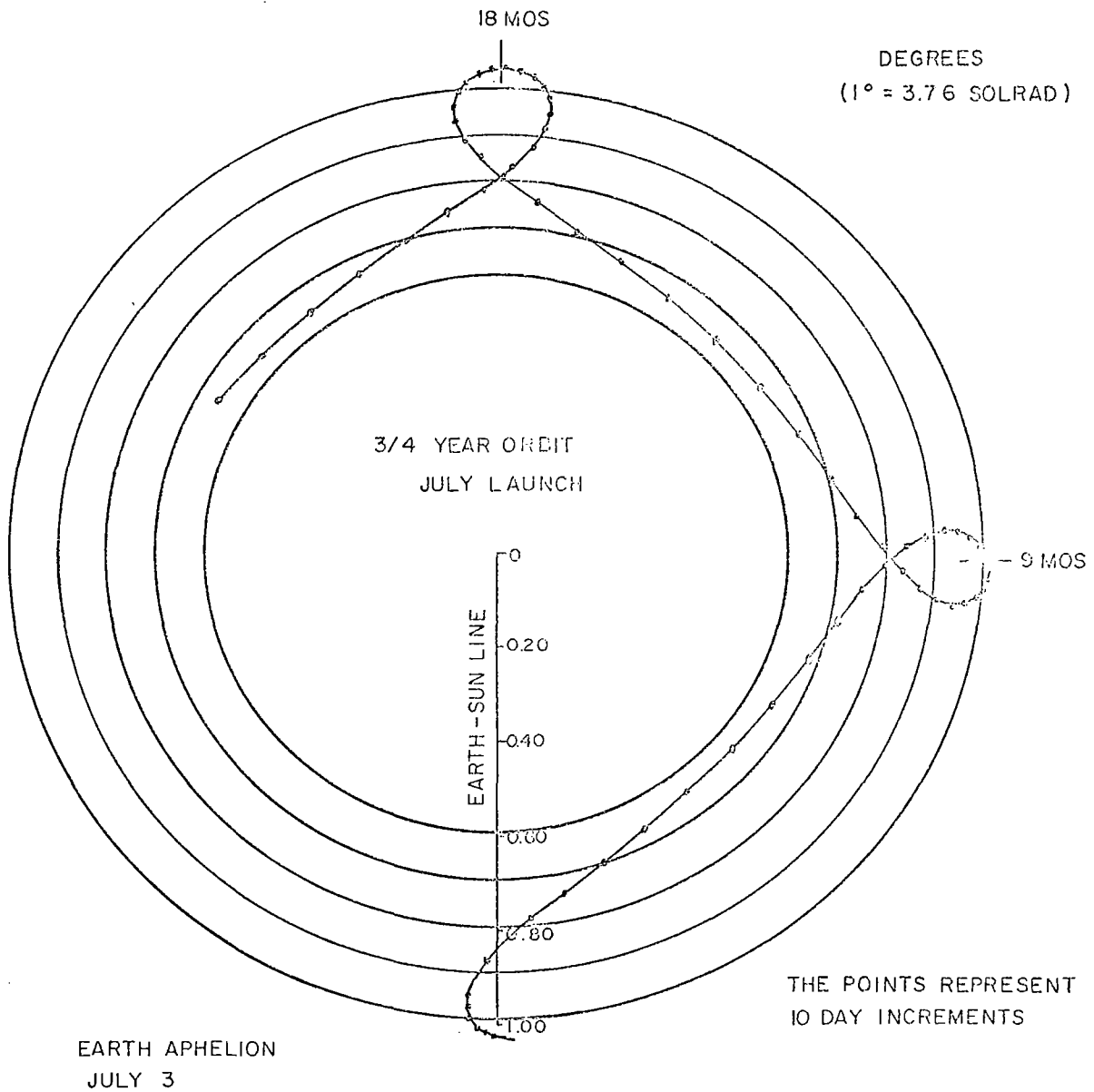
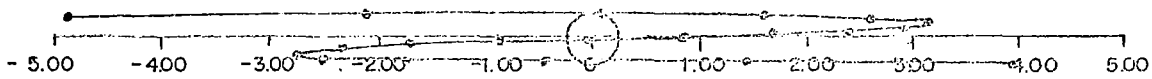


Figure 1 Geometry of Sunblazer radio probing

SOLAR ENCOUNTER PROFILE



SUNBLAZER ORBIT

Figure 2 Sunblazer Orbit diagrams

SOLAR ENCOUNTER PROFILE

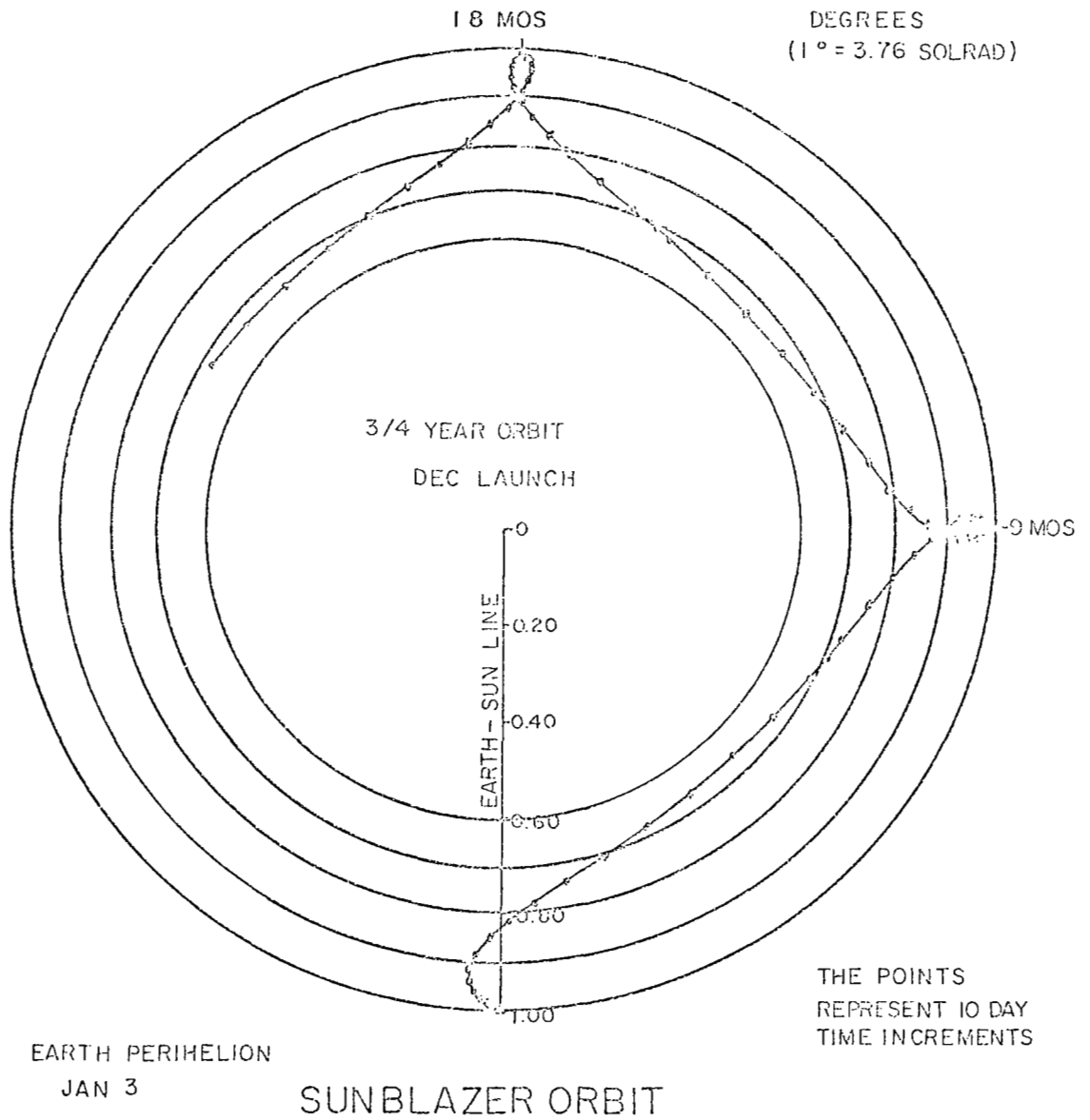
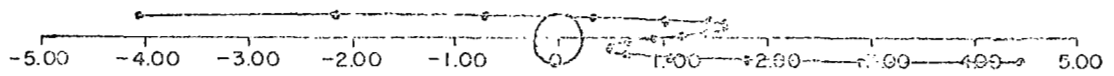


Figure 3 Sunblazer Orbit diagrams

(radio stars) and with spacecraft, which were designed for other purposes, but happened to pass behind the corona after their mission was over but the radio was still active.

Radio astronomers have deduced much about streams and blobs of plasma in the corona by statistically studying the scintillation (radio power fluctuations) of the signal. However, the difference between studies with the incoherent signal from a celestial source and the coherent one from a spacecraft is very crudely analogous to studying small objects by their shadows or by making holograms of them. The geometric shadow is mostly lost in the far field by diffraction around the edges of the objects, but the hologram retains phase information that allows reconstruction of the original wavefront. The analogy is very limited however, because our scan of the wavefront is mostly one-dimensional (holograms are two-dimensional), and because the corona refuses to hold still while we scan the amplitudes and phases (with relative orbital velocity).

A measure that only a coherent source can give is the total columnar electron density, I , i. e., the number of electrons in a column of unit cross-section that extends from spacecraft to Earth. This quantity is measured through the total radio phase shift or the pulse delay time that results from the plasma refractive index. This index is accurately given by the formula in Table I, which includes a wide variety of quantities frequently used in this report.

The MIT Sunblazer study was based on the capabilities of the Scout booster. We adhere to this constraint owing to the relative economy of Scout launches. The probe is considered to be spin stabilized and Sun-oriented, since the Sun provides the only reference direction easily located with simple sensors from the unguided spinning condition of the payload after injection by the Scout. The Scout spin rate is 140 to 180 rpm which must be despun to about 1 rpm before the payload's attitude is controllable by solar pressure. Two graphs show the payload capability in 3/4-year orbit, 58 to 75 pounds at 0.65 a. u. However, these graphs refer to the ecliptic plane, and it is very desirable to probe the corona out-of-plane as far as possible. Hence, these masses should be regarded as upper limits. Figure 4 is the payload graph for 5 stages without Algol III, and Fig. 5 with Algol III.

WALLOPS ISLAND LAUNCH

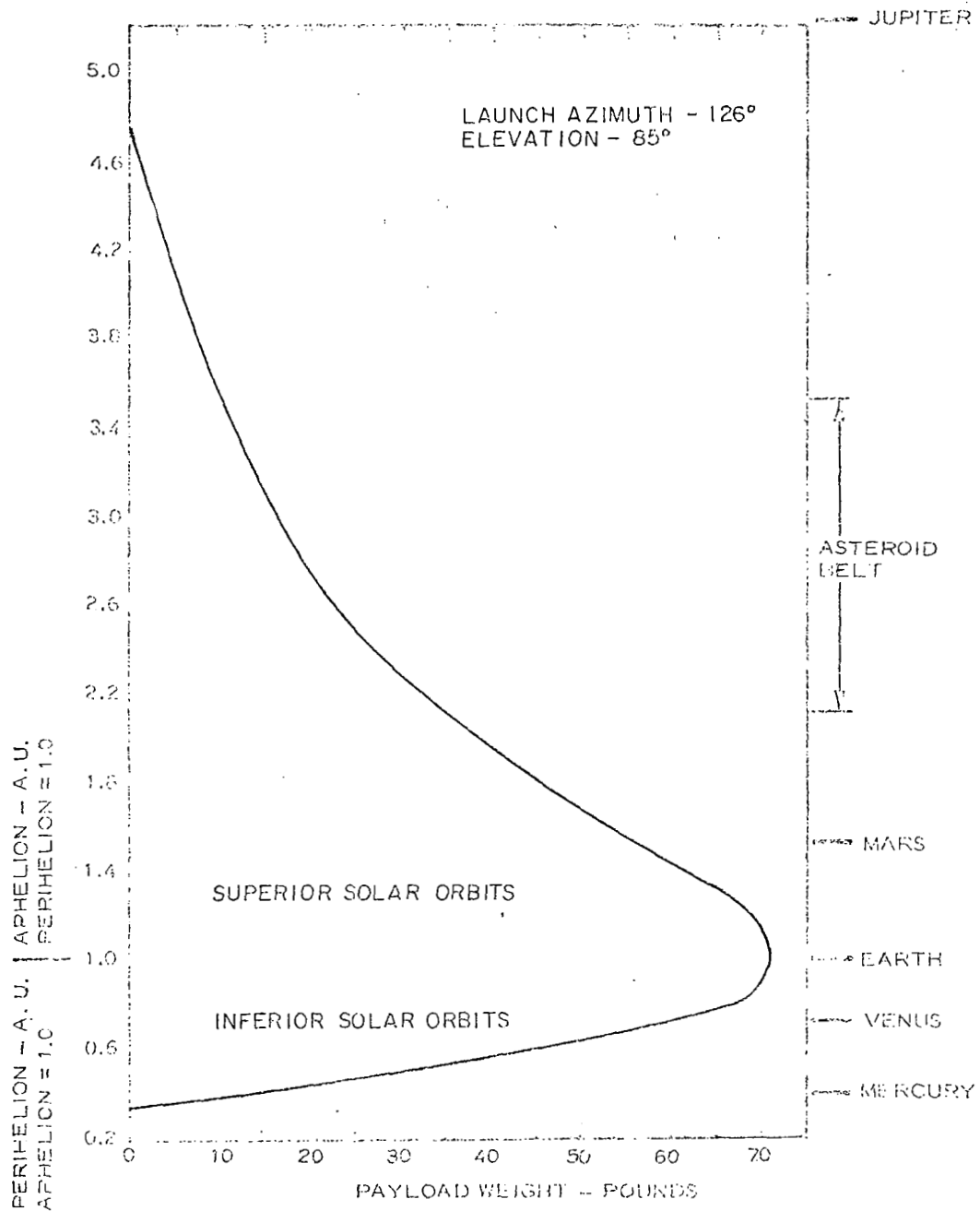


Figure 4 SOLAR PERFORMANCE - FIVE-STAGE SCOUT

Wallops Island Launch

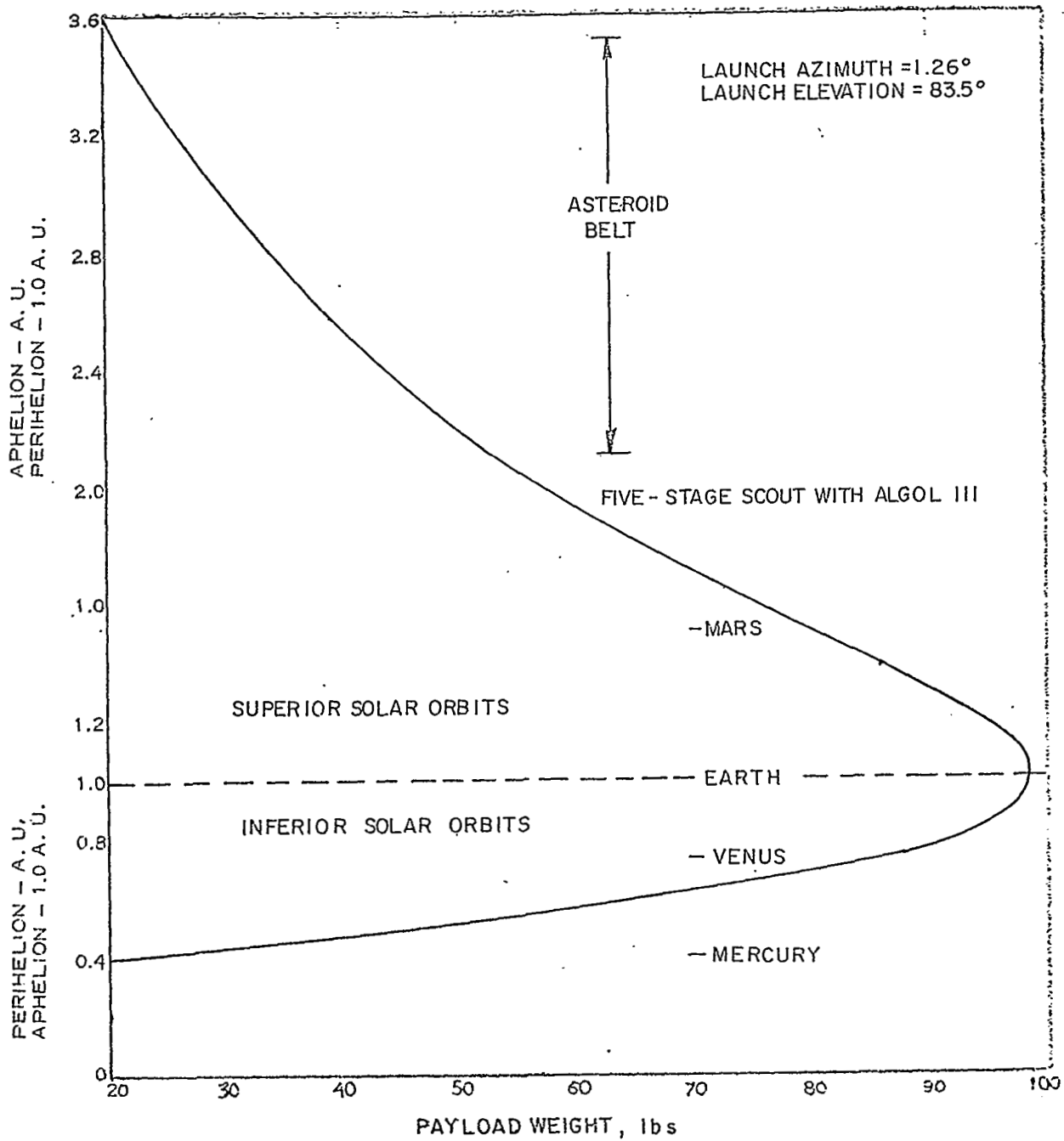


Figure 5 Solar Performance - Five Stage Scout with Algol III

TABLE I

FREQUENTLY USED QUANTITIES

SUN: Visible radius of sun (solrad for short) = 696 Mm
Angular radius seen from Earth (also solrad) = 0.266°
 $= 4.64 \text{ mradian} = (1/3.8^\circ)$
Rotation period of Sun (equatorial) = 25 day (sidereal)
 $= 27 \text{ days (synodic)}$
Radius of Sun at S-band freq. = 4 solrad = 1°
Phase of 11 year sunspot cycle:
Minima in 1954, 1965
Maxima in 1959, 1970

SOLAR RADIATION:

Particles:

Velocity of fast event = 1500 km/sec
Velocity of solar wind = 300 km/sec at Earth, slower near the Sun.
Solar wind density = 3-10 protons/cm³, bursts of 70 at times
Plasma refractive index,

$$n_{pg} = \frac{c}{v_{pg}} \left(1 \mp \frac{40.3 \times 10^6 N_e}{f^2} \right), \text{ where}$$

p = phase, g = group, N_e = electron density in cm^{-3} , and f = frequency in Hz

Sunlight:

Solar const at earth 1.35 kwatts/m^2 $\pm 10\%$ random fluctuations every few days.

EARTH:

Radius of earth = 6.38 Mm
Earth's orbital velocity = 30 km/sec = 2π rad/yr
 $= 1^\circ/\text{day}$
 $= 2.0 \times 10^{-7}$ rad/sec.
Earth's escape velocity = 11.2 km/sec
Orbit radius = 1 a.u. = 1496 Mm = 215 solrad

HARDWARE:

MIT sunblazer: 28 lbs, 20" diam. 6.8" height
Scout Booster: Spins 140 to 180 rpm, payload 25 to 75 lbs
depending on 4 or 5 stages, with or without
Algol III, distance orbit goes out of ecliptic plane.

Frequently Used Quantities (continued)

JPL Ground Facilities
at S-Band:

Noise Temp. - 27°K lowest
210 ft paraboloid antenna - 61.8 db gain
85 ft paraboloid antenna - 54 db gain

Power Loss at Range of
2 a.u.:

omni to 210 ft antenna, -207db
omni to 85 ft antenna, -215db

UNITS AND CONVERSION FACTORS:

1 arc sec = $4.85\mu\text{rad}$
1 mrad = $3'26''$, $3.44'$
1 year = $3.156 \times 10^7 \text{ sec} \approx \pi \times 10^7 \text{ sec}$
1 day = $8.640 \times 10^4 \text{ sec}$
1 rad/sec = 9.549 rpm

CONCLUSIONS AND RECOMMENDATIONS

The major features of the Sunblazer experiments as proposed by MIT are

- * two frequencies in the VHF band, 70 MHz and 80 MHz,
- * a downlink propagation experiment using high-power pulses and pseudorandom codes,
- * a special purpose receiving facility at El Campo, Texas with a large VHF dipole array having 50 db gain.

The large dipole array is required at the frequency MIT selected for lack of existing facilities with sufficient gain. In contrast to MIT our studies emphasize the economy of using presently available antennas and the advantages of many participant tracking stations to maintain a nearly continuous track and thereby observe infrequent solar events, most of which would be missed by part-time tracking.

Conclusions

Frequency. -Our strongest conclusion is that solar probes employing radio propagation should employ much higher frequencies than those recommended by MIT. In fact they should employ the highest of the frequency bands readily available for space communication in the NASA deep space net, most likely S- and X-band frequencies using the 85 foot paraboloid antennas. The reasons for this choice are many and compelling. The most cogent of them are:

- * A review of the status of knowledge concerning the solar corona shows that the most important questions to be answered pertain to the region only a few solar radii (solrad) from the Sun's surface. Much of this region would be effectively opaque to the lower radio frequencies. Even at S-band the Sun's radio radius extends to 4 solrad. At lower frequencies the opaque radius is unknown, but evidence suggests that it extends at least as far as 7 solrad at VHF.
- * Of existing facilities throughout the world which may be available for a cooperative effort, there seems to be an abundance of 85 foot paraboloids with high gain in the S-band region. The availability of the multiple facilities assures maximum data from the mission and the observation of most of the solar events that occur during the mission.
- * At higher frequencies a combination of antenna gain and reduced noise more than compensates for the decreased plasma interaction between the radio signal and the plasma. Hence, high frequency permits more accurate experimental measurements.

- * Very important advantages result from performing propagation experiments in the so-called weak scattering regime in which the irregularities in the solar plasma do not perturb the phase of the radio wavefront more than 1 radian rms. Even X-band is not high enough frequency to maintain this desirable condition in the inner corona. The trouble with strong scattering is that the mathematical solution of the propagation problem is so difficult that little confidence is placed in the relationship between corona parameters and radio measurements. Given a set of observed radio propagation measurements one cannot solve the propagation problem even with the largest digital computers for all possible models of the corona to see if more than one model would explain the given radio data. Moreover, large angle multiple scattering of radio rays tends to blur the detailed features of single scattering functions, which plays a more dominant role in the weak scattering regime.
- * Solar experiments conducted at JPL using Mariner IV and Pioneer VI have proven that the solar corona may be studied by techniques that are now standard for deep space even though those particular spacecraft were designed for other purposes and not optimized for the solar experiment. Hence, extra cost and development risk would needlessly result from non-standard frequencies or techniques. The best techniques are those that are standard specifically for deep space as opposed to satellites in near space. X-band is being developed for deep space telemetry; although it is not yet standard as is S-band.

Link Direction. -We also conclude that the propagation experiment should be done on the uplink from ground to spacecraft instead of the downlink. This is not as strong a conclusion as the one regarding the choice of frequencies, because many complex factors are involved in this decision.

In many ways a downlink experiment would be preferable because it would permit the experimenter to examine the raw data and eliminate the need for a separate telemetry link. By contrast an uplink experiment requires that the data be at least partially reduced automatically on board the spacecraft so that the results of the reduction have fewer bits of information. The reduced data can be transmitted to Earth on a slow data-rate telemetry link. This was the mode of operation in the Stanford Pioneer VII experiment. However, the overriding consideration is the large amount of power that can be transmitted on the uplink. For example, it is straightforward to transmit about 3.3 w from a spacecraft or 100 kw from the ground, or with more difficulty 10 w and 300 kw. In either example the ratio is 3×10^4 . Other considerations reduce this uplink advantage, especially receiver noise, (see the Link Analysis section), but the point here is that the power ratio is the overriding effect that favors the uplink. No matter how powerful the link, more power is always useful to prevent loss of signal during the more intense solar disturbances, to maintain track during deep signal fades resulting from scintillation, and

to relieve tracking schedules by bringing stations with smaller antennas on the line.

An important consideration in performing the experiment on the uplink is to carefully design logic circuitry for the data reduction required on the spacecraft. This should allow for every known type of solar event or corona phenomenon, so that important data will not be lost merely because the experimenter did not have access to raw data. The logic and telemetry will cost an appreciable amount in terms of time and money, but this expense is cost effective in view of the added benefits, the overall cost of a space mission, and the very little extra weight that this circuitry adds to a craft. Today there is considerable precedent for digital core storage of data, solid-state logic circuits, and complex data encoding on-board spacecraft.

The Spatial Extent of Corona Phenomena. -A weakness in the corona studies to date is the weak indirect methods that had to be used to determine the spatial extent of phenomena in the corona. Since the corona is moving radially out from the Sun at high speed, it is difficult to decide with certainty whether an event that crosses the line-of-sight is a long event moving especially fast or a short event moving relatively slowly. An independent method is needed to measure either the velocity or size of each event, so that both the velocity and size may then be deduced from the time in which each event crosses the line-of-sight.

We tried to devise various schemes for multiple lines-of-sight to a single craft so that each event could be observed to cross each line and velocity calculated from the time difference. The only workable method we found is multiple ground stations. The Cambridge group of radio astronomers (Hewish, et al) has observed radio sources with multiple stations and has cross-correlated the results to determine the velocity of the solar wind.

These considerations weaken the case for an uplink experiment, since any number of participants can observe simultaneously on a downlink without interfering with each other, or with proper functioning of the spacecraft. Since two carrier frequencies are required for any plasma probe experiment, two ground stations may participate in an uplink experiment, one on each frequency. However, these must be cooperative stations, because the carrier modulations must be synchronized, and the carriers should be harmonically related. More than two uplink participants require extra equipment on the spacecraft.

Corona Phenomena. -We conclude that the most important measurements are those which give clues to how and where the solar wind originates on the surface of the Sun, the density and velocity structures above the polar regions of the Sun, i. e., out of the plane of the ecliptic, and the size and shape of the larger scale inhomogeneities in the solar corona.

Recommendations

To measure the corona parameters deemed the most important we recommend the detailed design and construction of a payload for a Scout mission that is optimized for the following measurements listed in order of importance:

- * The measurement of columnar electron density by the phase modulation technique used at Stanford in the Pioneer VII experiment.
- * Counted cycles of relative phase difference between two harmonically related carriers for precise measurement of changes in electron content during the tracking period.
- * Phase jitter statistics correlated with scintillation statistics to evaluate the parameters of scattering in homogeneities with more precision than radio astronomers can attain with scintillation only.
- * Correlation between links involving two or more ground stations spaced 50 kilometers or so apart. The cross correlations of such signals yield data on the velocity structure of the solar corona.
- * Scattering measurements, i. e. the measurement of the apparent angular size of the coherent radio source, the blur circle that results from scattering of radio rays as detected with radio interferometers.

The last two measurements have been carried out extensively by radio astronomers using celestial radio sources, and are therefore of lesser importance. However, there is value in making these measurements simultaneously with the others, so that the cross-correlations yield more detail about the corona parameters, or possibly discriminate between plausible models of the corona.

We tentatively recommend an uplink system at S- and X-band using phase modulation for the electron density measurement as in the Stanford experiment. Although the frequency selection is clear cut, the uplink choice cannot be made firm until more is known about participating ground stations and additional parametric analysis is performed on weight, volume and cost of the required telemetry system. We recommend a spin-stabilized probe with the passive attitude control system as described in the Attitude Control section.

We recommend an orbit with a triple superior conjunction behind the solar corona, much like the orbits studied in the MIT Sunblazer

program. However, the conjunction should occur in the summer for maximum tracking time at the stations in the higher latitudes, and the orbit should be chosen for the maximum excursion out of the ecliptic plane, i. e., the maximum allowed by payload weight and booster thrust.

PRESENT KNOWLEDGE OF THE SOLAR CORONA

In this section we summarize the state of the current knowledge about the corona and interplanetary medium. The purpose is to identify areas in which more knowledge is needed, particularly if it is the kind of knowledge that may be gained with a small radio probe. The plasma that radiates from the Sun begins on the surface in a wide variety of temporary structures called enhancements, streamers, condensations, plumes, rays and flares. Some of the solar wind may even originate in much broader areas than those occupied by these structures; this is one of the major questions remaining to be answered. The denser part of the plasma which may be photographed during eclipse constitutes the K corona. In addition there is an F corona which is merely inner zodiacal light and is of no concern to us here except as it interferes with measurement of the plasma. Recall that zodiacal light is sunlit dust concentrated in the ecliptic plane. As the plasma goes beyond the visible corona, it is usually called the interplanetary medium, and the steady component thereof is known as solar wind. This wind was discovered in a curious way by noting that something was blowing the tails of comets from their expected direction behind the comet.

The Solar Wind

Comets frequently have two tails, type 1 which is plasma or ionized material, and a type 2 tail that consists of dust and other debris; see Fig. 6. When type 1 tails were originally observed to behave strangely, attempts were made to explain this in terms of solar pressure, i. e., light pressure. Biermann proved that radiation pressure alone is insufficient to explain the observations, and for this demonstration he is usually credited with the discovery of solar wind. The wind direction is observed to fluctuate 5 to 10 degrees from radial and can even point the comet tail forward; that is, the tail's offset from the radial direction can point ahead of the comet by a very small angle instead of behind it. Brandt (Ref. 1) has conducted the most detailed studies of comets. He found that the solar wind speed varies in a manner that correlates with geomagnetic activity and is more or less independent of the sun spot cycle. The mean speed is about 500 kilometers per second and the minimum 150 ± 50 km/s. Speeds usually range 300 to 500 km/s and may be higher during periods of intense geomagnetic activity. All these figures are for distances from the Sun on the order of 1 a.u. Although many comets penetrate deep into the solar system for close encounters with the Sun, none of the data on these is accurate enough to deduce the velocity of the inner solar wind.

The solar wind was theoretically predicted and has been extensively studied by Parker (Refs. 2 & 3), who coined its name. Weak magnetic field

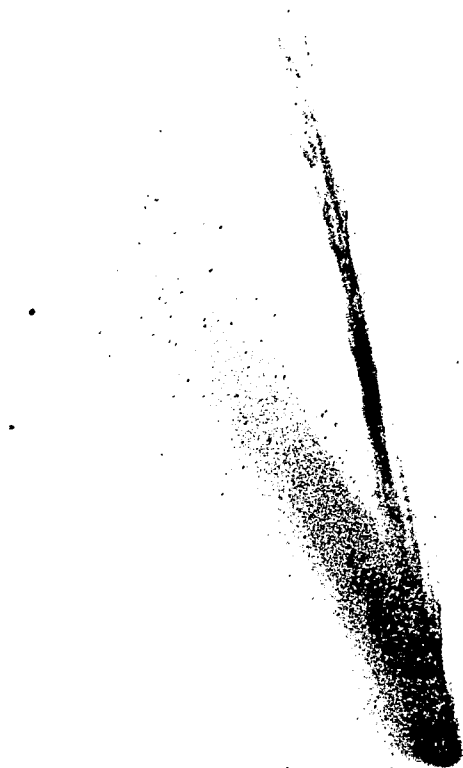


Figure 6 Photo from J. C. Brandt (Ref. 1)

permeates the solar plasma. The lines of force are propelled radially outward by the solar wind, but they generally remain connected to the Sun's surface. From spacecraft data we know that the field strength is 2 to 40×10^{-5} gauss at 1 a.u. The wind may have 0.4 to 80 ions/cm³, averaging about 5 , and their velocity ranges 300 to 900 km/s averaging 375 to 500 in agreement with comet studies. The main sources of wind lie in the region of 10 to 25 degrees north heliographic latitude, and the wind arriving at the Earth comes from 1.6° east of the Sun owing to the initial tangential velocity of the Sun's rotation.

The latitude range of the solar sources is known by studying the synodic period. The period is the apparent rotation period of the Sun as observed from Earth. Since the Sun is a ball of gas it is not required to have the same rotation rates at all latitudes as a rigid body would, and in fact the rate does vary with latitude. Thus studies of long-lived solar phenomena determine the heliographic latitude of events which are not visible on the Sun's disc by noting the latitude signature in the periodicity of the recurring observation.

Axford (Ref. 4) describes the solar wind as a supersonic flow, Mach 5 to 10 , since the divergence of the wind, the gravity and the low pressure in interstellar space combine to imitate a nozzle in the supercritical condition. He notes that solar wind is a crude thermostat on the corona maintaining it at 1 to 2 million degrees Kelvin. The more or less radial magnetic field tends to confine the flow to relatively thin tubes or jets. The high variability in the wind presumably reflects the highly variable conditions on the surface of the Sun at the foot of each stream tube. The streams have some nonradial movement which is presumably caused by interference of slow and fast streams, tubes expanding and contracting with the pressure, and tangential movement caused by rotation of the Sun, which twists the stream tubes into an Archimedean spiral like the familiar water sprinkler.

The Archimedean spiral obeys the equation

$$\frac{\omega - \omega_0}{\Omega} = \frac{r - r_0}{u} \quad (1)$$

where r is radial distance from the Sun, u is solar wind velocity (always radial), Ω is the Sun's angular velocity, and ω is heliographic longitude. Parker and others have shown theoretically that u increases rapidly with r near the Sun, then levels off and is roughly independent of r beyond 10 or 20 solrad. Parker finds that u ranges from 250 to 900 km/s depending on assumed temperatures. At 1 a.u. this velocity gives a spiral angle near 45° to radial. This angle is not to be confused with the particle velocity angle which averages only 1.6° from radial.

Think of the particles as beads on a spiral string that represent a magnetic field line. The beads slide radially outward while the spiral rotates.

Parker finds that mean free paths in the solar wind are of the order 1 a.u.; that is, the plasma is almost collisionless on the scale of the inner solar system. The implications of a collision-free plasma are interesting because various fluctuations and deviations from thermal equilibrium do not dissipate in the manner one expects with colliding particles. For example anisotropy along the magnetic field is allowed as is different temperature of the electrons and ions. The latter are rapidly cooled by adiabatic expansion and are expected to be cooler than the electrons. However, the persistence of small fluctuations in the solar wind density is greater than one would expect even for a collisionless plasma. The observations of these fluctuations will be discussed in connection with their effects on radio propagation. Probably the observed fluctuations at 1 a.u. will eventually be explained as fresh turbulence generated far from the Sun by the interaction of fast and slow streams and by plasma instabilities.

Synoptic studies (Ref. 5) have correlated both the magnetic field and the various properties of the plasma to the Sun's rotation rate. These studies show that the field and plasma properties are strongly sectorized by solar longitude. Ness identifies three time scales of events in the plasma:

1. micro-structure, less than 1 hour - shock waves and discontinuities in the density and magnetic field.
2. meso-structure, 1 to 100 hours - includes filaments, kinks.
3. macro-structure, greater than 100 hours - sectoring, length of filaments.

In summary the detailed features of the solar wind have a large amount of micro-structure, numerous filaments of magnetic field and high electron density separated by MHD (magnetohydrodynamic) discontinuities. Quasi-stationary structures are sectorized by heliographic longitude. These evolve and die with the eleven-year solar cycle.

Geomagnetic Storms

The magnetic storm on the Earth is another manifestation of solar plasma. In the "sudden commencement" storm the horizontal magnetic field on Earth increases in minutes. This is followed by a larger decrease which requires about a day. After several days the magnetic field returns to normal. This behavior has been correlated with visible flares on the Sun, and the time delay between the events has been timed to infer a surge of wind density with velocities in the range 1000 to 3000 km/s. A different

type of magnetic storm known as an "M-region event" recurs every 27 days. The source of these storms is not obvious, but it is known to come from low solar latitudes, since the synodic period at the solar equator is 27.3 days.

When a major visible flare gives rise to a geomagnetic storm, the intensity of that storm depends upon the heliographic longitude of the flare. This dependence is sharp enough to show that the ejecta are columnated in a jet and not spread over roughly 2π steradians from the position of the flare. When the source of geomagnetic disturbances has been identified on the Sun and is observed to rotate behind the Sun and back more than once, then it is possible to determine the velocity of the solar wind component by phase delay between the magnetic disturbance and the 27-day synodic period. This calculation yields velocities in the range 250 to 500 km/s. Clearly the solar plasma has considerable structure with both fast and slow streams.

The Visible Corona

The solar wind begins in the corona regions immediately surrounding the Sun as shown in the frontispiece photographs. These photographs are taken during eclipses of the Sun, and the outer regions of the corona give the distinct impression of a gas being launched into space. Higher resolution photographs of the corona (e. g., those taken on the Swathmore expedition of 1930) were described by Newkirk as having the appearance of a corona that was carefully groomed with a fine comb. The intensity of the coronal green line (5300 Å) has proven to be a good index of its kinetic temperature and its plasma emission.

The electron density in the visible corona has been measured carefully by eclipse photometry. The radiance has been measured as far out as 30 solrad. However, conversion of the radiances to reliable electron density is complex and very difficult. First the conversion assumes that all of the K corona is the result of Thompson scattering of sunlight, an assumption that is probably valid. More serious is the background of F corona or inner zodiacal light which ruins estimates of electron density beyond about 10 solrad. Polar electron densities may be about half the equatorial density (Ref. 6). Ney (Ref. 7) could fit his data from the 1959 solar maximum without assuming any electrons above 70° heliographic latitude. In short the high latitude electron density estimates are most uncertain. The density structure measured by photometry will be summarized after we describe other techniques by which density is measured.

Spacecraft Particle Experiments

Very valuable contributions to our knowledge of the solar wind have been made by the direct measurement of particle properties at

various spacecraft, both satellites and deep space probes. These experiments measured electron density, ion velocity and magnetic field in the region from Venus to Mars and especially near Earth. The wind velocity measurements agree with data from comet tails and other techniques and are found to range from about 300 to 800 km/s most frequently with the mean about 400 to 500 km/s.

A frequently cited work on this subject is the paper by Neugebauer and Snyder (Ref. 8) in which they present the results from Mariner II on its way to Venus. Their data show an increase in the solar flux at a rate greater than r^{-2} , but of course it is impossible to separate temporal variations from spatial ones. An interesting correlation appears when their data are examined on a 27-day periodic plot, which brings out the effects of solar rotation. The periodic display shows persistent sections of solar longitude in which the flux has greater velocity and reduced density for several rotations. The velocity depends much more strongly on longitude than on distance from the Sun. Mariner II found a normal ion flux of 3 protons/cm³ with enhancements as high as 70 p/cm³, which often recurred in 27 days. Some enhancements lasted several consecutive days. If a wind velocity of 400 km/s is assumed to be common at 1 a.u. then the observed enhancements correspond to lumps of dense plasma as large as 4 to 20 Mm.

Measurements of the interplanetary magnetic field by spacecraft show a remarkably stable field strength in the range 4 to 7×10^{-5} gauss. However, the sign of a field can reverse in a time interval from 10 minutes to several hours. The streaming angle of the magnetic field usually corresponds to an Archimedean spiral for velocities in a range 300 to 700 km/s. From the duration of the fields of the same orientation, Newkirk concludes that the width of a magnetic bundle lies between 0.3 to 3 Gm. Correlation (Ref. 9) between the direction of the interplanetary field and the arrival of cosmic rays suggested that the magnetic tubes of force have overall dimensions from 0.7 to 6 Gm.

Strong et al (Ref. 10) studied data from the Vela II satellite. They find that the solar wind varies from the radial direction $\pm 10^\circ$ with an average of 1.5° east in agreement with comet data (Ref. 11). In fact the solar wind has been studied by spacecraft so thoroughly in the 1 a.u. region that in our recommendations we favor experiments that emphasize the inner solar system. Axford gives a summary of spacecraft experiments reproduced here as Table II.

A cross correlation measured between the direction of the interplanetary magnetic field at 1 a.u. and the direction of the magnetic field on the photosphere by Ness and Wilcox 1964, (Ref. 12) shows a decided correlation peak at a delay of $4.5 \pm .5$ days. This interval converts directly to a wind velocity of 385 ± 45 km/s, which agrees with the direct measurement of 378 km/s on the IMP I satellite (Refs. 13 & 14).

TABLE II

| Vehicle | Designation | Launch Date | Experimenters |
|---------------|-------------------------|-------------|--|
| Lunik-II | 1959 χ | 2-IX-59 | Ac. Sci. (U.S.S.R.) ^h |
| Lunik-III | 1959 θ | 4-X-59 | Ac. Sci. (U.S.S.R.) |
| Venus-I | 1961 γ 1 | 12-II-61 | Ac. Sci. (U.S.S.R.) |
| Explorer-10 | 1961 K | 25-III-61 | M.I.T. ^a |
| Explorer-12 | 1961 ν | 16-VIII-61 | Ames ^b |
| Mariner-II | 1962 α g1 | 27-VIII-62 | J.P.L. ^c |
| Explorer-14 | 1962 β γ 1 | 3-X-62 | Ames |
| Mars-I | 1962 β v1 | 1-XI-62 | Ac. Sci. (U.S.S.R.) |
| IMP-1 | 1963 46A | 27-XI-63 | Ames, M.I.T., G.S.F.C. ^e |
| (Explorer-18) | | | |
| Vela-2a, -b | 1964 40A/B | 17-VII-64 | Los Alamos ^f |
| OGO-1 | 1964 54A | 5-IX-64 | Ames, M.I.T., G.S.F.C., A.F.C.R.L. ^d |
| IMP-2 | 1964 60A | 4-X-64 | Ames, M.I.T., G.S.F.C. |
| (Explorer-21) | | | |
| Mariner-IV | 1964 77A | 28-XI-64 | M.I.T., J.P.L. |
| Zond-2 | 1964 78C | 30-XI-64 | Ac. Sci. (U.S.S.R.) |
| IMP-3 | 1965 42A | 29-V-65 | Ames, M.I.T., G.S.F.C. |
| (Explorer-28) | | | |
| Vela-3a, -b | 1965 58A/B | 20-VII-65 | Los Alamos |
| Venus-II | 1964 91A | 12-XI-65 | Ac. Sci. (U.S.S.R.) |
| Venus-III | 1965 92A | 16-XI-65 | Ac. Sci. (U.S.S.R.) |
| Pioneer-VI | 1965 105A | 16-XII-65 | Ames, M.I.T., Stanford ^e |
| Luna-10 | 1966 27A | 31-III-66 | Ac. Sci. (U.S.S.R.) |
| OGO-3 | 1966 49A | 7-VI-66 | Ames, M.I.T., G.S.F.C., A.F.C.R.L. |
| IMP-4 | 1966 56A | 1-VII-66 | M.I.T., G.S.F.C. |
| (Explorer-33) | | | |
| Pioneer-VII | 1966 74A | 17-VIII-66 | Ames, M.I.T., Stanford |
| IMP-5 | 1967 51A | 24-V-67 | |
| Venus-IV | 1967 58A | 12-VI-67 | |
| Mariner-V | 1967 50A | 14-VI-67 | M.I.T., Stanford |
| A-IMP | 1967 | 19-VII-67 | M.I.T. |
| (Explorer-35) | | | |
| Vela-4a, -b | 1967 | | Los Alamos |

^a M.I.T. = Massachusetts Institute of Technology, (Bridge, Rossi, Lazarus, Egidi, Pai, Olbert, Dilworth, Bonetti, Lyon, Vasyliunas, Binsack, Scherb, Moreno, Jacobson, Davis).

^b Ames = Ames Research Center (N.A.S.A.), (Bader, Wolfe, Silva, McKibbin, Mason, Myers),
^c G.S.F.C. = Goddard Space Flight Center (N.A.S.A.), (Serbu, Maier).

^d A.F.C.R.L. = Air Force Cambridge Research Laboratories, (Sagaiyn, Smiddy).

^e Stanford = Stanford University, Stanford Research Institute, (Eshleman, Garriott, Leadbrand, Peterson, Howard, Kochler, Long, Lusignan).

^f Los Alamos = Los Alamos Scientific Laboratory, (Strong, Asbridge, Hundhausen, Bame, Gilbert, Gosling, Coon, Felthausen, Hones, Singer, Olson, Heckman).

^g J.P.L. = Jet Propulsion Laboratory, California Institute of Technology, (Snyder, Neugebauer).

^h Ac. Sci. (U.S.S.R.) = Academy of Sciences of the U.S.S.R., Moscow, (Gringauz, Bezrukh, Ozerov, Rybchinsky, Balandina, Shklovskii, Moroz, Kurt, Khokhlov, Musatov, Bordovskii, Shyutte, Rytov, Remizov).

List of spacecraft, both satellites and probes, for which experimental measurements of the interplanetary plasma have been published in the literature, after Axford (Ref. 4).

This subsection has been restricted to the properties of the plasma measured at the location of the spacecraft and not the radio propagation experiments that integrate the effects of the plasma along the line-of-sight from spacecraft to Earth, as discussed in the next main section.

Overall Density and Velocity Structure

From one to ten solrad the overall electron density of the corona is found by eclipse photometry. In the neighborhood of 200 solrad (near 1 a.u.) the density is found from direct spacecraft measurements. In between we have little to go on except the studies of natural radio sources (radio stars) viewed through the interplanetary medium. In principle the interplanetary medium causes a number of seeing effects, namely refraction, attenuation, scattering and scintillation. However, refraction and attenuation are so small that they have not been used for quantitative work. Scattering and scintillation will be discussed at greater length in connection with Radio Propagation through the interplanetary medium. For this subsection we are concerned only with observations of scattering when the propagation path offset is from 10 to 80 solrad.

By making some rather poor assumptions, these scattering data allow a crude extrapolation of the electron density curve in the missing region between photometric and space probe data. Erickson 1964 (Ref. 15) has reviewed scattering theory. To extract overall density from these data it is necessary to assume (a) the scattering of the corona is equivalent to a thin phase changing screen, an approximation that is valid at high enough radio frequency as discussed under Radio Propagation; (b) the scale length of the scattering irregularities in the plasma increases in direct proportion to r , the distance from the Sun; (c) the fractional amplitude of the scattering fluctuations (blobs) and the fraction of space which they occupy is independent of r . Then to the extent that these assumptions are valid

$$\Delta \theta = C f^{-2} \bar{n}_e(b), \quad (2)$$

where $\Delta \theta$ is the apparent half width of the radio source as a result of scattering of the radio rays, C is an undetermined constant evaluated by matching the calculated density to the photometric density near 10 solrad, f is the radio frequency, \bar{n}_e is the average electron density evaluated at b the offset distance of the propagation path from the Sun; see Fig. 1. The resulting values of \bar{n}_e are too high when carried to 200 solrads where spacecraft data are available. The most suspect assumption is (c). Parker finds in his theoretical studies that there should be smoothing of the scattering fluctuations. Also assumption (b) about the single scale size of the scattering fluctuations (blobs) in plasma density is poor because the blobs are expected to be elongated along the direction of the magnetic field.

The combined results regarding overall density measurements of the equatorial corona from photometry, theory and spacecraft measurements are shown in Fig. 7 . Our knowledge of the polar corona is meager in comparison to the equatorial.

We turn now to the overall velocity structure of the solar wind. The velocity of the outer wind is of course well established by good agreement between spacecraft and comet data. As we noted earlier some comets venture close to the Sun but unfortunately the data are not accurate enough for velocity measurements there. In fact measurements of inner wind velocity are few and ambiguous. Although the movement of certain features has been observed, the particle velocity is not readily related to the features of which the particle is a part. The Sun has been observed by radar from 25 to 50 MHz and it was hoped that doppler shifts in the radar return would give the velocity of the inner plasma. Reflections from irregularities at speeds up to 200 km/s have been observed but interpretation is very difficult. Chrisholm and James conclude that at 38 MHz the corona resembles a spiny Christmas tree ornament from which we see occasional specular reflections. For a review, see Ref. 16.

Bohlin et al (Ref. 17) observed the spiral curvature of a single high-latitude streamer and thereby calculated the velocity distribution of the inner corona by Eq. (1). However, this technique has the weakness that it necessarily assumed the initial velocity to be entirely radial. Figure 8 is taken from Newkirk (Ref. 18). This figure summarizes the various measurements and theories we have discussed, except for Parker's theory which falls close to the curve labeled N. The wind velocity data is not accurate enough to discriminate between various theories. The differences between streamers and inter streamer space are unknown.

An interesting comparison of the orders of magnitude of various velocities in space is the following:

| | | |
|-----------------------------------|---|--------------|
| Earth satellite orbital velocity | = | 8 km/sec. |
| Earth's orbital velocity | = | 30 km/s |
| Solar wind | = | 300 km/s |
| Ejecta from solar storm max. vel. | = | 3,000 km/s |
| Velocity of light | = | 300,000 km/s |

Structures Near the Sun

Table III taken from Newkirk's review article is a summary of characteristic structures in the solar corona. These structures have been studied primarily by photography, but notice that the last column remarks on the radio emissions from some of them. In planning new spacecraft missions the helmet streamers and polar plumes attract our attention because they extend to many solar radii, and their density is of the order of $10 \times$ background density. They have not yet been detected by radio emissions, so a study of these structures by radio propagation

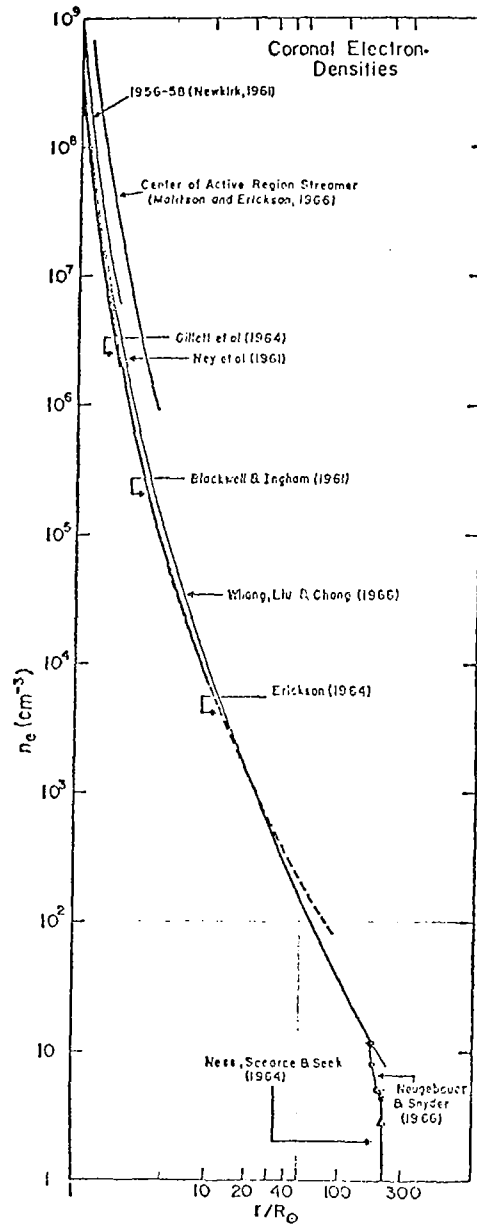


Figure 7 A compilation of electron densities in the equatorial solar corona derived from a variety of techniques. No attempt has been made to rectify data made during different portions of the sunspot cycle. A single theoretical model [Whang, Liu & Chang 1966 (Ref. 19)] of the density structure in the solar wind appears for comparison. Newkirk (Ref. 18).

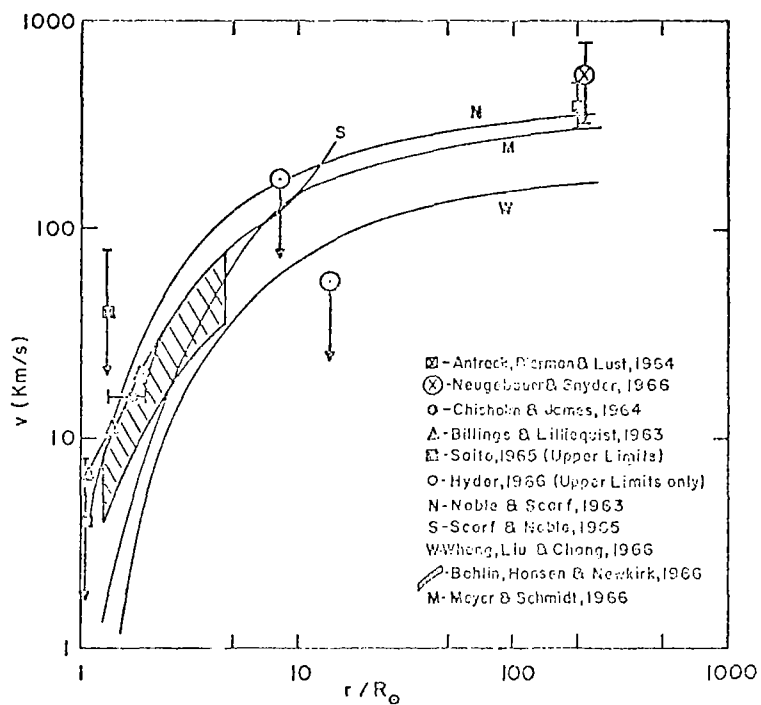


Figure 8 Estimates of the velocity of the solar wind at various distances compared with several theoretical models. \square - comet tail data; \otimes - spacecraft data, Mariner II; shaded region - curvature of a single streamer; M - most recent improved theory. Newkirk (Ref. 18).

TABLE III
SUMMARY OF CHARACTERISTICS OF CORONAL STRUCTURES

| Structure | Diameter at $1 R_{\odot}$ | Extent in height | Typical density enhancement | Typical density at $1.1 R_{\odot}$ (cm^{-2}) | Typical temperature ($10^6 \text{ } ^\circ\text{K}$) | Typical age of region | Lifetime | Associated surface feature | Associated coronal emission-line feature | Associated radio, X-ray, and UV feature |
|---------------------------|---------------------------|--|------------------------------|---|--|-----------------------|--------------------------------------|---|--|---|
| Active-region enhancement | 200,000 km (5-7 min arc) | 200,000 km ($0.3 R_{\odot}$) | up to $2\times$ | 4×10^8 | 1.5 to 2 | 2 weeks | 2-3 weeks | young active-region plage | green and red line enhancement | "plage" |
| Active-region streamer | 300,000 km (5-7 min arc) | many R_{\odot} | 2 to $5\times$ | 10^9 | 2 | 3 weeks | 2-3 weeks | | | |
| "Permanent" condensation | 50,000 to 130,000 km | 80,000 km | $5\times^a$ | 10^9 | 2-3 | 3 weeks | several days | most vigorous active regions, type E sunspot, plage | green and red line enhancement | small bright "button" within plage |
| Sporadic condensation | 20,000 km | 20,000 to 80,000 km (may appear as isolated cloud above surface) | 50-500 \times | 10^8 - 10^{11} | 4-5 | 3 weeks | fraction of an hour to several hours | often associated with flares and loop prominences | yellow line (5674 Å Ca XIV), continuum | gradual rise at cm radio wavelengths, post-flare enhancements in X rays |
| Helmet streamer | 300,000 km | many R_{\odot} | upper limit of 7-25 \times | ^b | 1.5-2 | 8 weeks | many months | prominence, extended magnetic fields | ? | ? |
| Equatorial streamer | 300,000 km | many R_{\odot} | — | $2-4\times 10^8$ | 1.5-2 | ? | months to years | 15 hours | ? | ? |
| Polar plume | 30,000 km | many R_{\odot} | 4-8 \times^a | 5×10^8 | 1.2 | ? | ~ 15 hours | bright polar faculae | ? | ? |
| Narrow ray | 30,000 km | many R_{\odot} | ? | ? | ? | ? | ? | ? | ? | ? |

^a Because of uncertainty in true electron densities over the pole, this figure may represent a lower limit.

^b Density enhancement seldom appears close to surface.

Newkirk (Ref. 18).

is worthwhile. Note in the lifetime column that the solar plume is short lived, about 15 hours. This short time constant emphasizes the need for more or less continuous tracking when the line-of-sight in the propagation experiment passes close to the Sun.

The polar plume bears a striking resemblance to lines of force about a bar magnet. The polar regions of the Sun are more a patchy collection of magnetic regions than a true dipole. Newkirk notes that lines of force are seldom if ever symmetrical around the Sun's rotation poles. Wyndham (Ref. 20) finds a dipole-like alignment of blobs (short for scattering inhomogeneities) in the polar corona out to 5 or 10 solrad as observed with a radio source behind the corona. This suggests that polar rays keep their identity far into the interplanetary medium.

Bursts of radio noise from the Sun have been studied and are believed to originate in disturbed plasma from solar flares. In these bursts the frequency drifts toward low frequency which is quite naturally interpreted as the reduction in plasma frequency while the excited plasma spreads as it travels up from the Sun. Type II bursts are characterized by a slow frequency drift and velocities in the range of 1000 km/s. These are believed to be hydromagnetic shock waves. Type III radio bursts are believed to be caused by bursts of very energetic particles. The velocity of the ejecta can approach the velocity of light. Values of electron density derived from radio bursts are usually high, a fact which probably results from the biased selection of the most energetic bursts. Figure 9 (Ref. 22) shows the points from type II and III radio bursts to lie along the highest density curve. Below that are the densities from optical observation of streamers, and lowest of all are the densities derived from theoretical models for the maximum of the solar cycle.

Natural Radio Sources (Radio Stars)

The solar corona has been extensively studied by listening to radio sources which chance to pass behind the corona. We have already noted that the refraction and attenuation of the radio rays are too weak for quantitative information. However, the scattering and scintillation have yielded valuable results. The scattering of rays means that the radio image of the source is blurred, and the blur is resolved in one dimension by observations with radio interferometers. Scintillation means that the power level of the signal fluctuates in a random manner, and the statistics may be analyzed for clues to the statistics of the corona.

Radio Scattering. -A recent summary of scattering data has been given by Slee (Ref. 21). Slee's data at 85.5 MHz combined with data from Erickson scaled to the same frequency give half power widths from 1/10 to 1/100 minute of arc. After changing the units we present the same data in Fig. 10. Slee observed many sources and found the radio scattering corona to be elliptical, elongated in the solar equatorial plane. Evidence

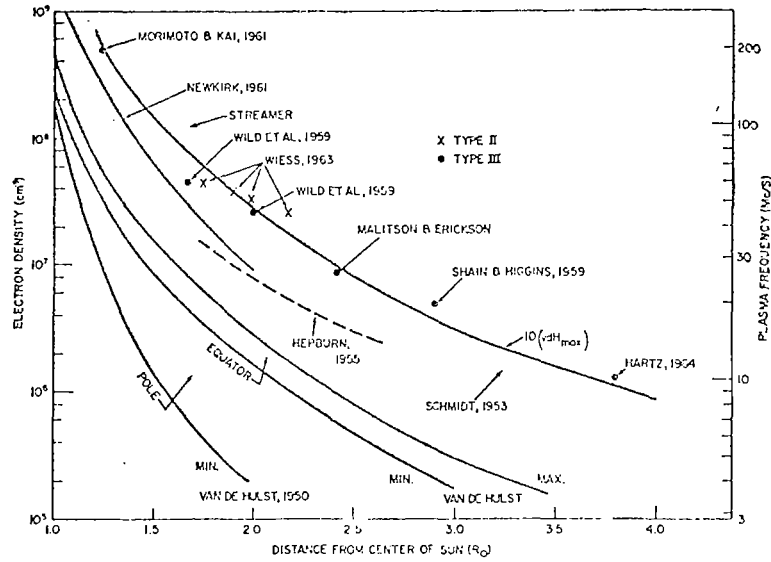


Figure 9 Radio-burst measurements require electron densities over active regions to be enhanced ~ 10 times those in the model derived for the equator by van de Hulst. The fact that optical observation of streamers (Newkirk, Hepburn & Schmidt) yields slightly lower densities than the radio data is probably caused by the preferential occurrence of bursts in the most active (and most dense) regions. (From Malitson & Erickson 1966)(Ref. 22).

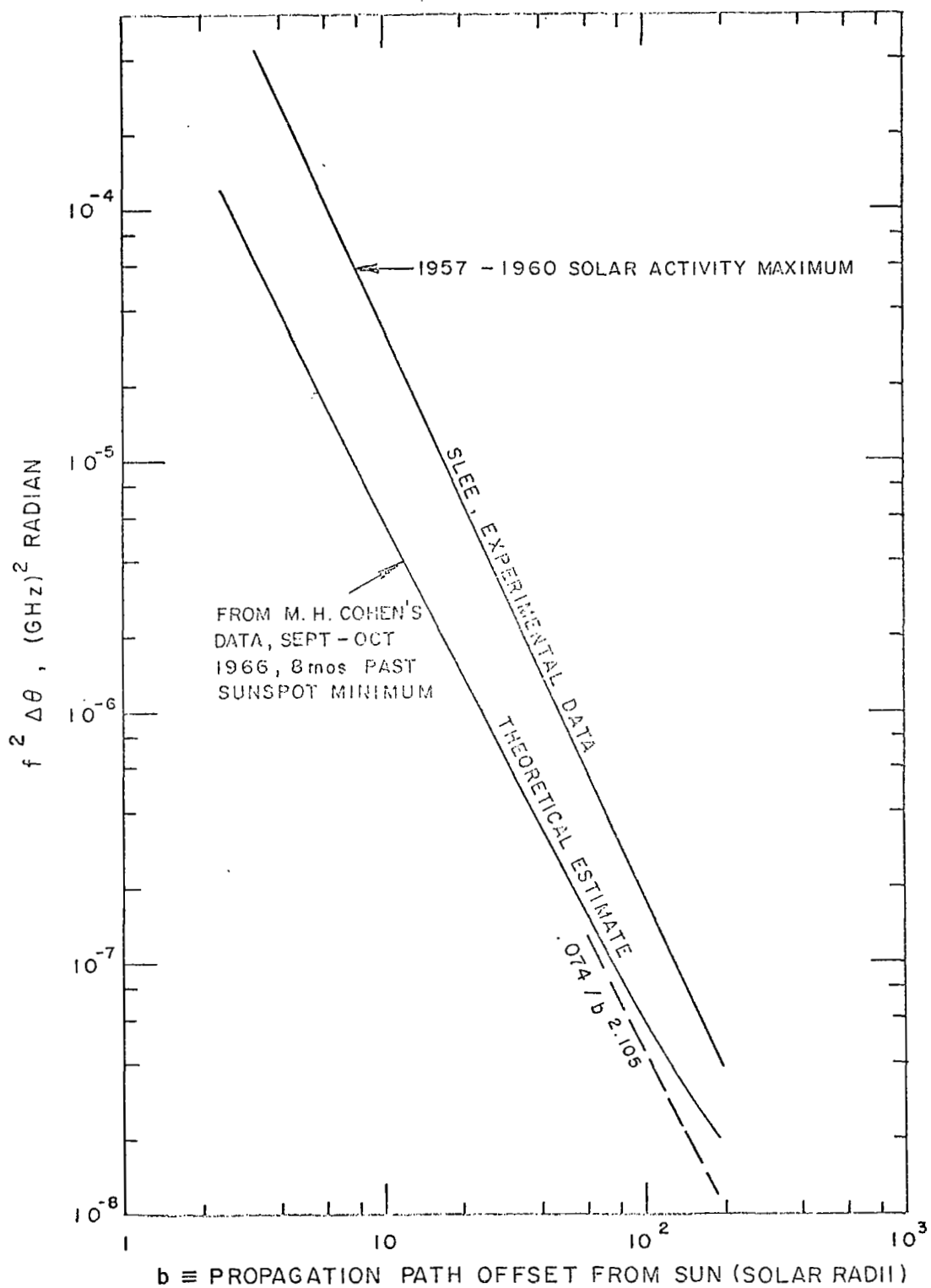


Figure 10

suggests that the elongation was related to a visible active belt. He also found significant random changes in 24 hour intervals. Radio scattering is observed to be anisotropic (Ref. 23) in the direction that supports the conclusion that the blobs are filaments extended in the direction along the magnetic field.

Axford (Ref. 4) summarizes the main results of radio scattering as follows:

1. The size of the blurred image varies with the solar cycle, especially close to the Sun.
2. The angular size of the blobs, i. e., the lateral size of the filaments is less than about 6 arc seconds (corresponding to an upper limit of about 5000 km at 0.3 a.u.).
3. The scattering becomes more pronounced near the solar equator.
4. The mean elongation of blobs is largely radial from the Sun but with substantial variations at times.
5. The mean scattering angle varies as the square of the wavelength.
6. The mean scattering angle varies with distance from the Sun as r^β where β is in the range 1.3 to 2.3 depending on the phase of the solar cycle and the latitude.

Radio Scintillation. - Hewish et al (Ref. 24) and Cohen et al (Ref. 25) have extensively studied the statistics of corona blobs by measuring the statistics of interplanetary scintillations. Salpeter (Ref. 26) gives an excellent theoretical description of the scintillation which converts the statistics of the blobs into the statistics of the received signal power, and his theory has been used extensively by Cohen et al (Ref. 27) to analyze experimental results. The main properties which Cohen finds are summarized as follows:

1. The scale size of the blobs is on the order of 100 km, a few proton gyro-radii.
2. The r. m. s. electron-density fluctuation varies approximately as inverse square of the distance from the Sun in the range .2 to .9 a.u.
3. The amplitude of the fluctuation is only about 2% of the mean density.

Hewish et al have observed and correlated the scintillation using more than one radio antenna. These show that the observation results from a movement of a diffraction pattern across the surface of the Earth. With two stations 50 km apart they find:

$$u = 50 \text{ km} / 0.1 \text{ sec} = 500 \text{ km/sec}$$

where u is the velocity of the solar wind. Correlation vanishes after the separation of a few hundred kilometers between stations, so we find that the structure is not frozen in the solar wind but it rather is constantly changing as though caused by a random pattern of sound waves. Three receivers suffice to give the speed and direction of the solar wind. Observations by Dennison and Hewish (Ref. 28) indicate that the solar wind is radial within $\pm 15^\circ$ and the average speed is 300 to 500 km/s, values which are consistent with all our other data, for the region observed, namely from 78 to 170 solrad. Figure 11 shows a tendency for the solar wind speed to increase at high heliographic latitudes, which is thought to be real and consistent with comet tail observations.

The interpretation of the radio scattering and scintillation data must be compared with other sources of information about the fine structure of the solar wind, in particular data regarding the sudden accelerations observed in comet tails, and the extent to which cosmic rays have been diffused by passing through magnetic irregularities. To some extent the radio data are in conflict with the other sources of information as discussed by Newkirk (Ref. 18). According to him space probe experiments have definitely discovered an abundance of large percentage density fluctuations having dimensions as large as 4 to 20 Gm at 1 a. u. In the radio data these would be expected to cause larger scale image movements which are not observed. Newkirk further remarks that the extreme anisotropy of flux within a given tube and the abruptness of the tube boundaries require that the magnetic field should be smooth on a scale of 100 Mm, the gyro-radius of the particles. Thus the small scale fluctuations that cause radio scintillations are not expected on this basis. Newkirk remarks:

"Radio source occultations and interplanetary scintillations require the presence of structures with a scale of 5×10^3 km and rule out the existence of fluctuations as large as 10^6 km. On the other hand, direct plasma probes and the inference of density fluctuations from the structure of the interplanetary magnetic field demonstrate unquestionably the presence of structures of dimensions of the order of 10^6 km, and cosmic-ray measurements suggest that irregularities smaller than 10^5 km cannot occur in any great numbers in the entire space between the Sun and the Earth."

His remark about cosmic-ray measurements means that, if the magnetic fields in space are as bumpy as the electron density, then one would

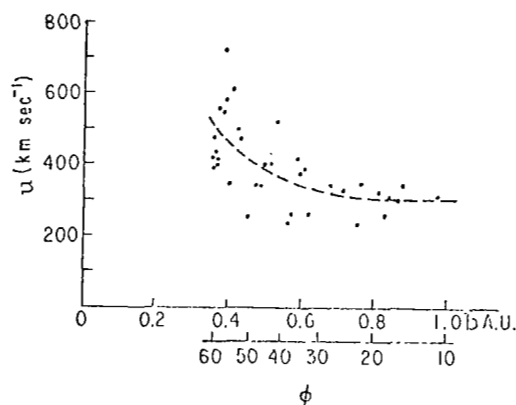


Figure 11 The velocity of the solar wind obtained from observations of interplanetary scintillations of 3C48 using three spaced receivers during February-July 1966 (Dennison and Hewish 1967). b is the minimum distance of the line-of-sight to the source from the Sun, and ϕ is the heliographic latitude (in degrees) of the point of closest approach (it is assumed that most of the scattering is produced at this point). It is believed that the increase in the velocity is entirely due to the change in ϕ , since observations of the Crab nebula (which at the same time was situated at $b \approx 0.5$ a.u., $\phi \approx 5^\circ$) showed the average velocity near the ecliptic plane to be 295 km sec^{-1} , compared with 420 km sec^{-1} derived from observations of 3C48 at the same distance from the Sun. Compare this figure with the results obtained from comet-tail observations.

expect these bumps to cause diffusion of neighboring cosmic rays so that the cosmic ray flux arriving at the Earth is not as well collimated as observed. Newkirk concludes that the cosmic ray data appear to require that the small density blobs are not associated with a corresponding structure in the magnetic field.

Perhaps the crucial part of this conflict in data interpretation is that no radio image dancing is observed over angles of the order of 6 arc seconds and times on the order of minutes. Hewish and Symonds discuss this matter to some extent. A thorough analysis of the phase jitter in a radio propagation experiment could help to resolve these difficulties, because the interpretation of data from natural sources is hampered by incoherence which means that only the intensity fluctuations may be studied, or at most the relative phase at two nearby stations. By contrast the data from radio propagation experiments contain both absolute phase and scintillation which may be correlated for interpretation in terms of a more detailed plasma model.

Other Means for Observing the Solar Corona

We are aware of only two other means that have been used to study the corona, namely planetary radar and spacecraft propagation experiments. The latter is the Sunblazer technique, and therefore the subject of a detailed discussion in the next section. Columnar electron densities, i. e., electron density integrated along the line-of-sight, have been successfully measured by Muhleman et al in planetary radar experiments (Ref. 29). In contrast to spacecraft techniques planetary radar provides a most cost effective means for studying the columnar electron density toward the Sun as far as the orbit of Mercury, about 84 solrad, and away from the Sun as far as the orbit of Mars, and possibly even Jupiter.

The Need for Future Experiments

Our knowledge of the average electron density in the solar corona (see Fig. 7) is extrapolated by theoretical means from about 10 solrad, where photometric techniques leave off, to 200 solrad where direct measurements by space probes begin. If this gap can be filled in by planetary radar to Mercury, then the density is theoretically extrapolated only over a range from 10 to 84 solrad. This gives a fairly complete picture of the density in the plane of the ecliptic; however, our knowledge of the density out of the plane is very poor. We can only agree with Axford who suggests that a spacecraft experiment out of the ecliptic plane would be very useful.

Our knowledge of the velocity structure of the solar wind in the inner solar system is very limited. Recall that the knowledge of the inner velocity structure (Fig. 8) comes from the curvature of a single high latitude streamer and from various theoretical models which must assume some plausible temperature structure of the corona.

Perhaps the multistation experiment by Hewish et al will be repeated at higher frequencies that permit closer approach to the Sun. Recall that in these experiments the correlation between stations gave the velocity of the plasma as each point in its diffraction pattern crossed first one station and then another.

One of the main questions that could be answered with a new radio probe that passes behind the corona is the question of the extent of the solar wind sources. Does this wind arise from a number of small active regions on the Sun, or from much larger areas? Also the very large blobs or intensity enhancements on the scale of megameters should be observed in radio propagation experiments. There is no question but what these have been observed by interplanetary probes, and we need to find out why these large blobs do not appear in the scattering data from radio sources. The spacecraft propagation technique is the natural way to study these large blobs close to the Sun, since the direct measurement is restricted to outer regions that are accessible to spacecraft. The radio source experiments do not give a direct measure of columnar electron density, since this requires a coherent source as will be discussed in the next section.

In summary, the principal needs for new data by spacecraft are measures of all quantities in the immediate vicinity of the Sun, which requires the highest possible frequencies to penetrate and study, the study of large scale electron density enhancements everywhere in the corona, but in particular inside the orbit of Venus, and finally the study of overall density out of the plane of the ecliptic. Radio propagation experiments may or may not give clues to certain old problems such as the connection of the intermediate corona to the surface of the Sun and the mechanisms for heating the corona.

SPACECRAFT RADIO PROPAGATION EXPERIMENTS

Three spacecraft have been the subject of radio propagation experiments to study the solar corona or solar wind through which the signals pass. In two of these the spacecraft passed behind the Sun and thereby allowed studies of the signal passing through the dense part of the solar corona. These events were the superior conjunction of Mariner IV in the spring of 1966 and the solar occultation of Pioneer VI in November of 1968. The third experiment was performed with Pioneer VII while it was on the same side of the Sun as the Earth. Pulses of increased solar wind density were observed passing between the Earth and Pioneer VII at ranges up to about 0.5 a.u. The three experiments are summarized in the subsections below, starting with the most recent and thorough of the three, the solar occultation of Pioneer VI.

The Solar Occultation of Pioneer VI

Pioneer VI was launched on December 16, 1965. Since then it has remained active for the remarkable duration of at least 3.5 years. It passed behind the Sun's disc between November 21-24, 1968. Some of its orbit parameters are as follows.

| | |
|-----------------|----------|
| Period | 311 days |
| Semi-major axis | 134 Gm |
| Eccentricity | 0.0942 |
| Inclination | 0.169° |

In coordinates based on the Earth to Sun line, the orbit of Pioneer VI is the septagon figure shown in Fig.12a. Note that it takes about seven years for one period of the beat frequency between Earth and Pioneer VI; that is after seven years from launch Pioneer VI will be close to Earth again. Figure 12b shows how the orbit of Pioneer VI would look if one could see it passing behind the Sun. The spacecraft is spinning at 58 rpm about an axis perpendicular to the plane of the ecliptic, which means that it is spin stabilized in such a way that it qualitatively resembles another planet.

Pioneer VI transmitted the S-band frequency of 2.292 GHz. The transmitter employed a 7.7 w traveling wave tube. The antenna radiated a linearly polarized signal with the E-field parallel to the spin axis, and therefore perpendicular to the ecliptic plane. The antenna is a Franklin array which radiates an axially symmetric pattern 5° wide at the half power points. The signal received during the period near occultation was 4×10^{-20} w at the 210 foot antenna of JPL's Goldstone tracking facility. During the experiment the frequency drifted about 14 Hz/day,

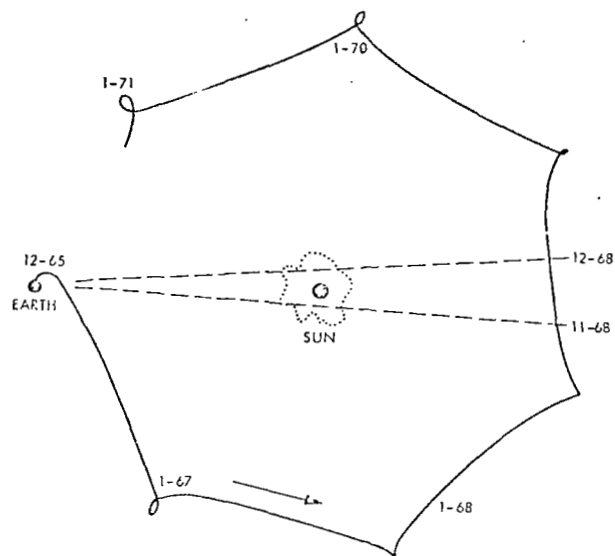


Fig. 12a Projection of Pioneer VI orbit
on plane of ecliptic relative to
Earth-Sun line

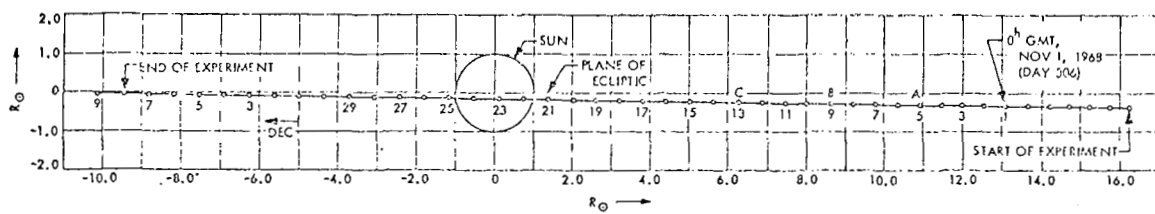


Fig. 12b Projection of Pioneer VI orbit relative to the plane of the ecliptic

The Orbit of Pioneer VI after Levy et al (Ref. 30)

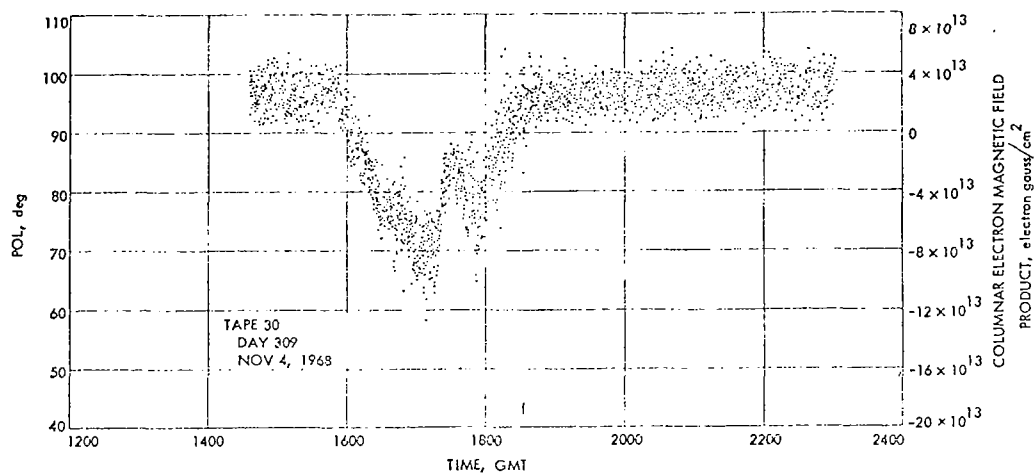
which was presumably due to slow temperature drift of the spacecraft. In addition there was an erratic drift of 1 or 2 Hz which occurred about every 15 minutes.

One of the two experiments involving Pioneer VI was the Faraday rotation experiment performed by Levy et al (Ref. 30). The Faraday effect is the rotation of the plane of polarization of the signal caused by propagation through an electron gas which has a component of magnetic field parallel to the direction of propagation. At the frequency used, 2.292 GHz, one degree of rotation resulted from 3.9×10^{12} gauss-electrons/cm². Note the cm² instead of cm³ because the electron density has been integrated along the entire line-of-sight from spacecraft to Earth. Levy et al devised a closed loop polarimeter which tracked the polarization of the incoming signal. The polarimeter included a special feed for the 210 foot antenna which was rotated under the control of a servo system to null out one of the two orthogonal linear polarizations.

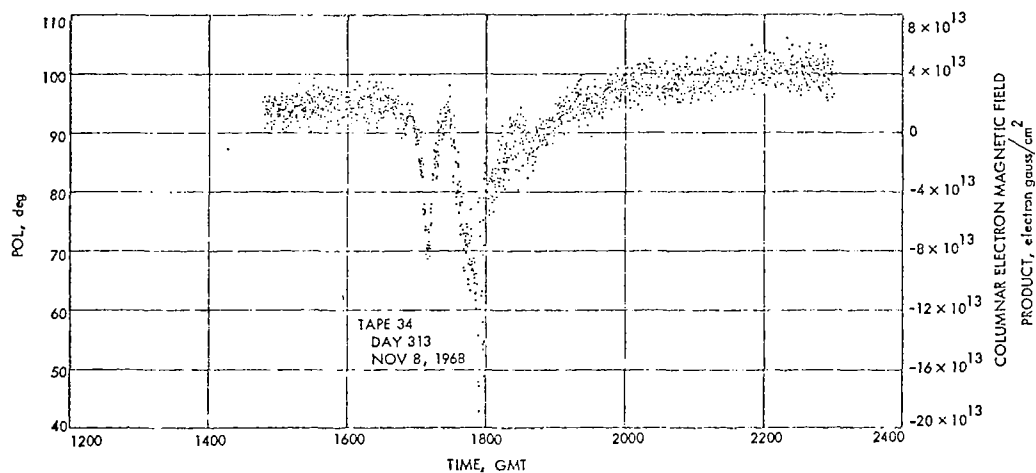
A polarization experiment was performed from October 26 to November 16, 1968 at which time the signal disappeared about one degree (4 solrad or solar radii) from the Sun. From November 21 to 24 the spacecraft was behind the Sun's disc. The signal was reacquired on November 29 about one degree on the other side of the Sun, and the experiment continued from then until December 8, 1968. While the spacecraft was still fairly far from the Sun it was used as a signal source to study the diurnal cycle of Faraday rotation in the ionosphere at the S-band frequency, so the ionospheric effects would not be confused with the solar corona effects. The ionosphere comparison also included Pioneers VII and VIII which were nowhere near passage behind the Sun.

The results of the experiment consist primarily of three intense plasma events at 10.9, 8.6, and 6.2 solar radii, which all occurred before occultation on November 4, 8 and 12 respectively. Each event lasted 1 to 2 hours and rotated the plane 30 to 40 degrees, always in the same direction. By comparison the ionosphere only rotated the polarization through 10 degrees for the full diurnal cycle, and in one of the events the direction of the solar polarization change was opposite to the drift caused by the Earth's ionosphere. Hence there is no chance that ionospheric events were mistaken for solar ones. The polarization plots from Ref. 30 are reproduced here as Fig. 13. The twin peaks on each of these plots (indicating magnetic fields in the same direction) at times an hour apart should be of interest to corona model makers. The times of the three events correlate closely with Goldstein's experiment discussed below and with radio noise bursts near the west limb of the Sun, the limb nearest the spacecraft. Moreover, the events occurred just after a large sunspot had rotated into the west limb, as shown in Figs. 14 and 15.

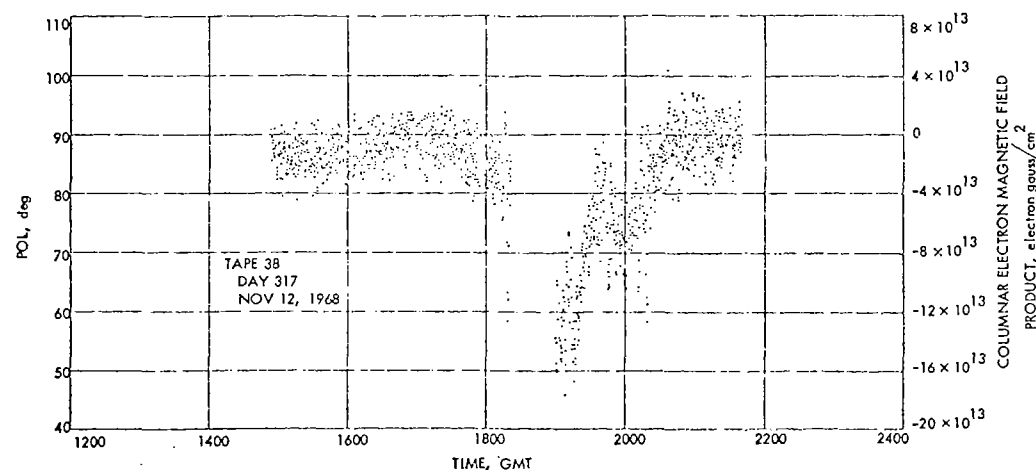
Type III Dekametric noise bursts preceded each of the three principal observations of Faraday rotation events. If one pairs each rotation event



November 4, 1968



November 8, 1968



November 12, 1968

Figure 13 Polarization data after Levy et al (Ref. 30)

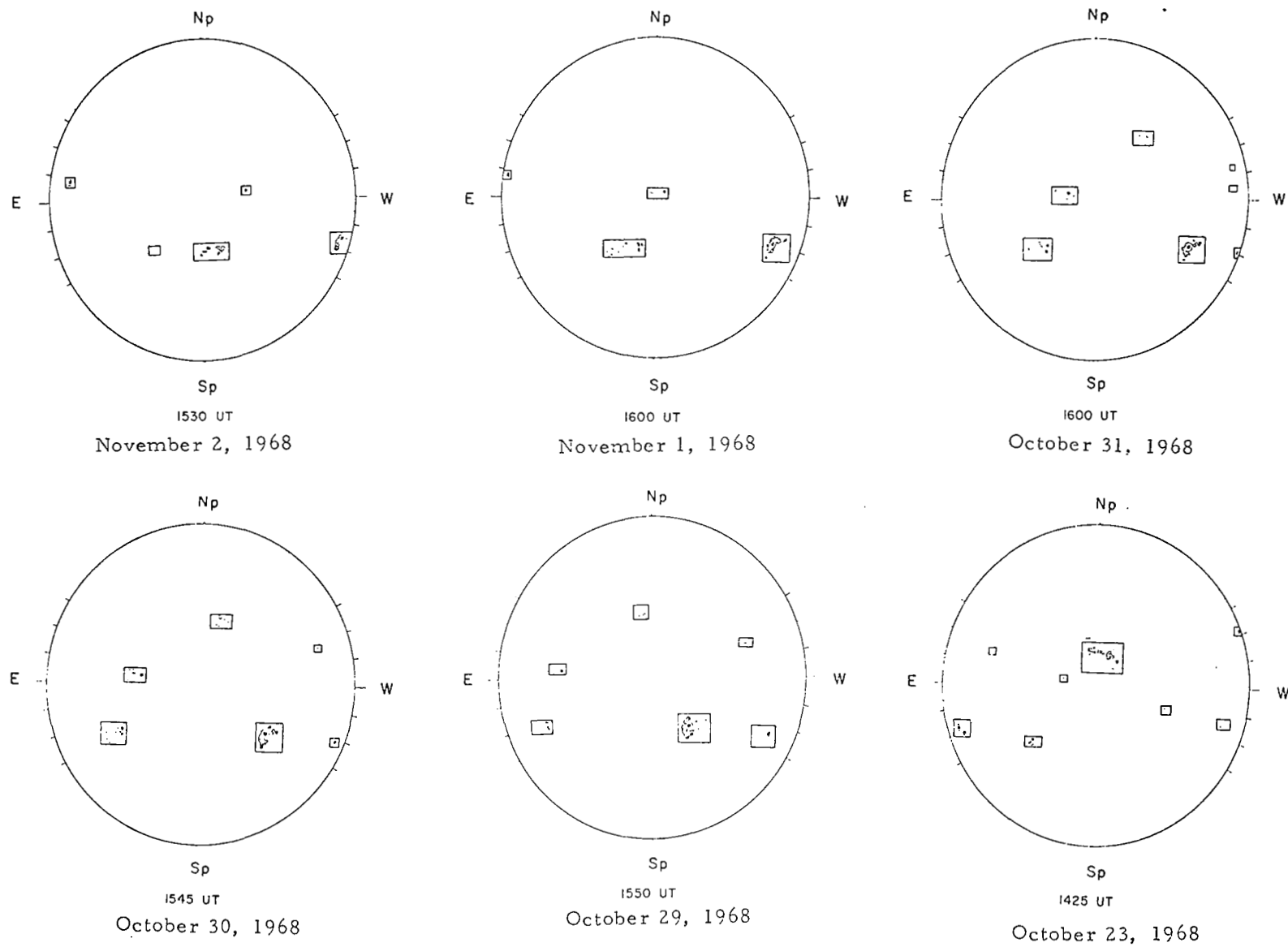
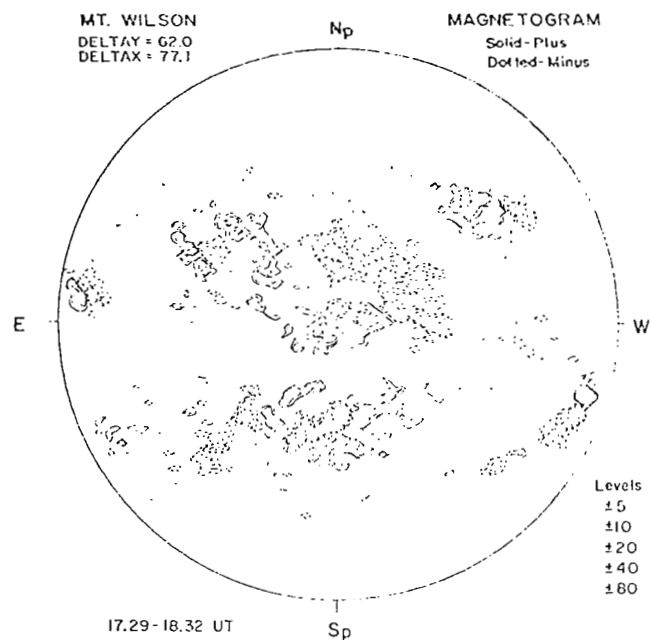
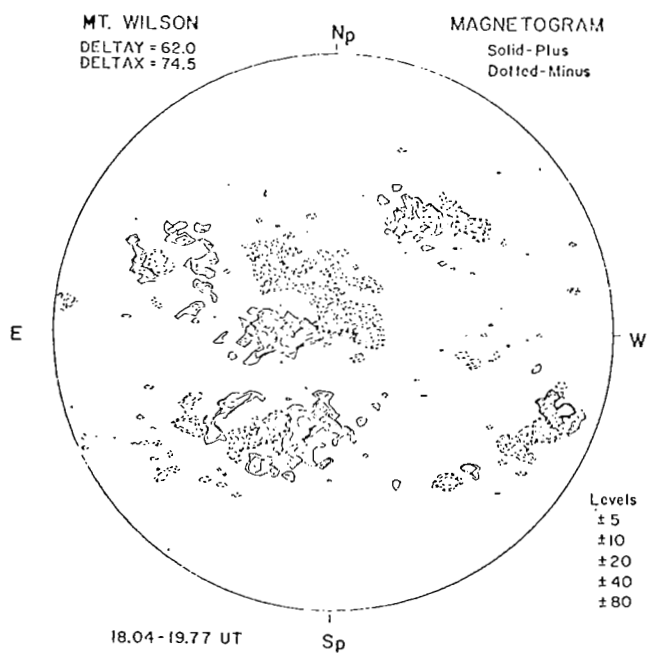


Figure 14 Sunspots taken by Environmental Sciences Services Administration, Boulder, Colorado



November 2, 1968



November 1, 1968

Figure 15 Magnetograms from Mt. Wilson Observatory

(Continued on next page.)

No data obtained on October 31 or 30, 1968.

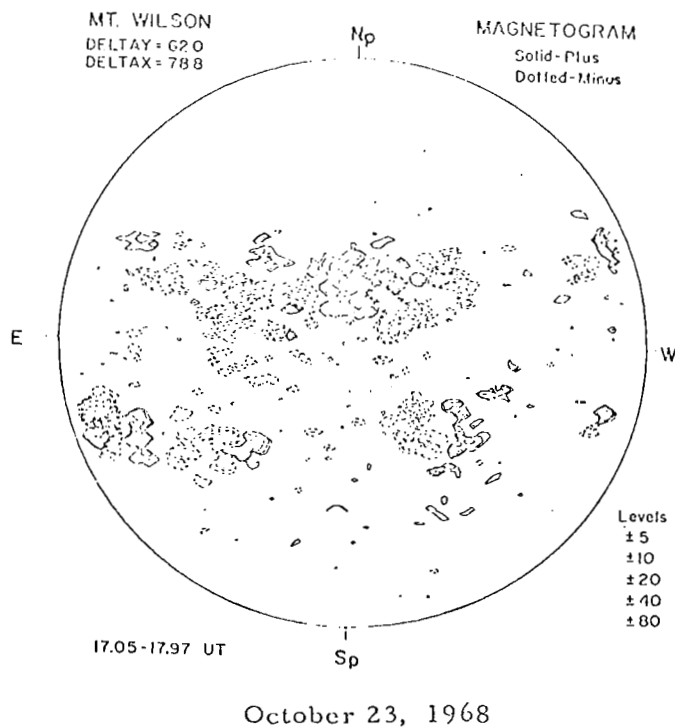
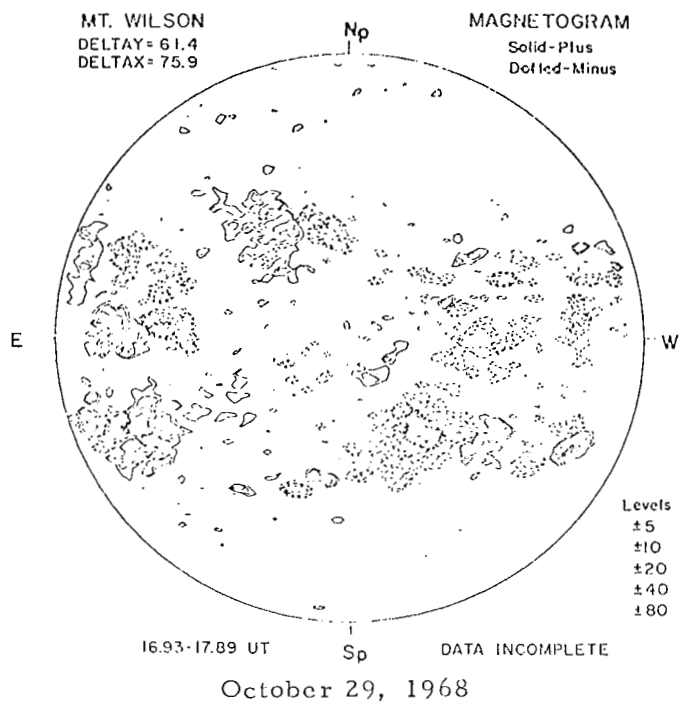


Figure 15 (concluded)

with a particular noise burst, assuming they represent the same solar disturbance, then he can calculate the velocity at which the plasma burst traveled from the Sun out to the line-of-sight. Levy et al have tabulated these velocities for each of the noise bursts that might be regarded as the appropriate mate to each of the Faraday rotation events. On Nov. 8 there was only one such burst which gives a velocity of 1.490 km/sec, about 4 times faster than normal solar wind. The other two events were preceded by multiple bursts which give velocities anywhere from 430 to 1,170 km/sec.

A separate experiment with Pioneer VI was performed by Richard M. Goldstein (Ref. 31), who measured the spectral broadening of the signal as a result of passage through the corona. His experiment also straddled the occultation event and was performed from October 31 to December 8, 1968 during which time the line-of-sight from the spacecraft moved from about 3.5° on one side of the Sun to 2.5° on the other. The received signal was divided into 15 minute blocks and a Fourier transform of each block computed to make spectrograms in a 100 Hz bandwidth.

Goldstein particularly remarked on the disappearance of the signal at 1° from the center of the Sun even though the visible radius of the Sun is only about 0.26° , and the system had sufficient capability to track much closer to the Sun. Goldstein states that the behavior is as though the disc of the Sun has an S-band diameter of 2° . The 210 foot dish has a beam width of only 0.14° at S-band and a system noise temperature of only 25° K when pointed far from the Sun. Of course near the Sun side, lobes of the antenna will pick up extra noise from the Sun. At 1° this raises the effective system noise temperature to the range of 200° - 300° K. Moreover, as the antenna rotates to track the Sun some of the minor lobes of the antenna will go on and off the Sun's disc and cause slightly erratic noise events. Nevertheless at 1° from the Sun there was ample signal-to-noise ratio to continue tracking had the Sun permitted this. The apparent loss of signal could be the result of a sudden increase in absorption, possibly scattering, or more likely a frequency spreading that reduced the spectral density of signal below the noise level.

Goldstein's principal results were the observation of the same three events that Levy et al observed, and the observation of the spectral broadening just before and just after the signal disappeared behind the Sun. On November 8 for example, the signal bandwidth jumped suddenly from a residual of about 2 Hz at 1641 o'clock to a bandwidth of about 10 Hz at 1701, and continued to grow to nearly 20 Hz at 1752. From then on the bandwidth decays much more gradually than it widens. Curiously, Goldstein did not state that the sudden onset and gradual decay is what one would expect if a more or less spherical shell of plasma from the Sun struck the line-of-sight. The short dimension of an expanding shell would continue to lie within the line-of-sight for a long time until the shell passed both the spacecraft and the Earth.

The Superior Conjunction of Mariner IV

On March 26, 1966 the line-of-sight to Mariner IV passed the Sun at a distance of 3.3 solar radii from the center of the Sun's disc, Fig. 16. At this time the range to the spacecraft was approximately 328 Gm, slightly over 2 a. u. In other words the spacecraft was slightly farther from the Sun than the Earth is. Goldstein (Ref. 32) studied radio propagation through the solar corona at a frequency of 2.116 GHz on the uplink and 2.295 GHz on the downlink. At this time in the life of the spacecraft the directional antenna was pointed away from Earth, so the experiment had to be performed with the omnidirectional spacecraft antenna. For the uplink 100 kilowatts was transmitted from an 85 foot antenna at the Goldstone tracking facility, and the spacecraft received with a noise temperature in the neighborhood of 2000°K. For the downlink the spacecraft transmitted about 5 to 10 watts, which was received at the 210 foot antenna, which has 61.8 db gain and a noise temperature of 27°K when the antenna is pointed far from the Sun. The received signal at conjunction was -170 dbm, or 10^{-20} w. During the experiment there was approximately 20 db excess solar noise received at the ground station; that is, the overall noise temperature was often in the range 200°-300°K when the antenna side lobes picked up solar noise, instead of the nominal 27°K.

In the absence of an uplink signal Mariner IV transmits with its frequency controlled by its own internal oscillator. However, when it is receiving, the spacecraft operates as a transponder, deriving its transmission frequency from the received signal. An interesting feature of Goldstein's experiment is that the spacecraft received sufficiently strong signal to maintain phase lock even at the great range of 320 Gm, but the ground station could not maintain phase lock even though the downlink used the 210 foot antenna while the uplink used only an 85. Such is the advantage of the uplink over the downlink on account of the much more powerful transmitter.

The experiment was performed in two modes, a one-way and a two-way propagation mode. In the first mode the spacecraft was transmitting a signal derived from its own free-running oscillator. At the ground station the received signal could not be heard in the ordinary sense, so a band of noise at frequencies known to contain the signal was studied and processed to extract the spectrum of the signal from the noise. The received data were divided into time blocks of about 45 minutes each. These were Fourier transformed to give spectra with a resolution of 0.245 Hz. Most of the resulting spectra had an equivalent width of about 4 Hz as shown in Fig. 17a. Of this width 1.5 Hz was caused by frequency drift of the spacecraft oscillator during the 45 minute integrating time.

The second mode of operation employed two passes through the solar corona by way of the spacecraft's transponder. The ground transmitter had to be tuned very slowly to give the spacecraft receiver an opportunity to find the signal and lock on to it. The problem here can be appreciated

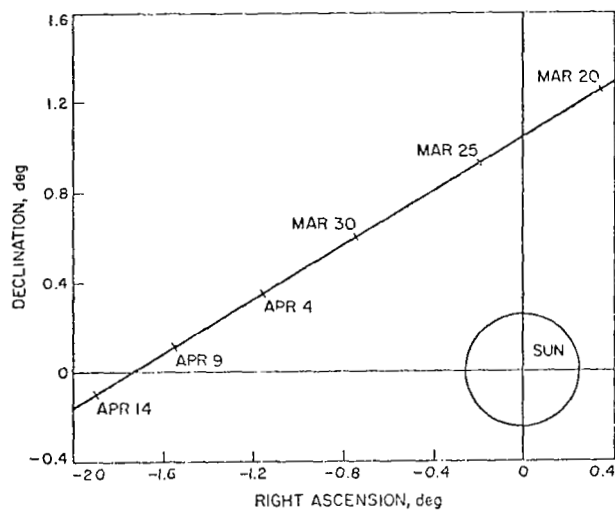


Figure 16 Mariner IV Solar Passage, after Goldstein (Ref. 32)

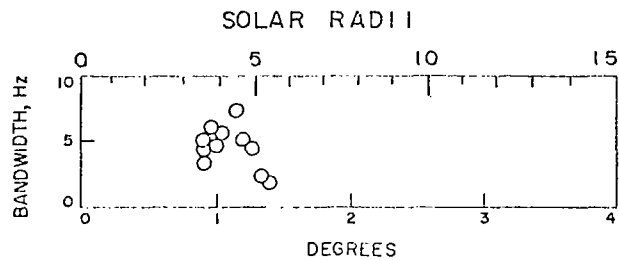


Figure 17a One-way Bandwidth as a Function of Angular Distance from the Sun, after Goldstein (Ref. 32)

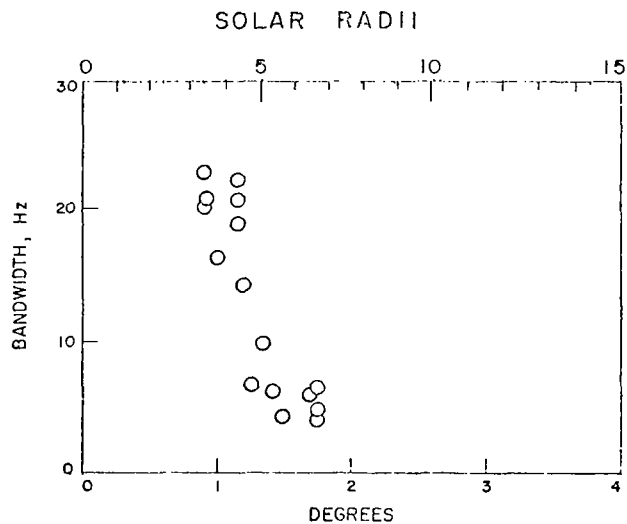


Figure 17b Two-way Bandwidth as a Function of Angular Distance from the Sun, after Goldstein (Ref. 32)

by recalling that the round trip signal propagation time is in excess of 30 minutes. Thus when the transmitter was tuned to the proper frequency, 30 more minutes elapsed before this fact was known to the experimenter doing the tuning. As a result the two-way acquisition problem consumed an excessive amount of tracking time, which was used to maximum advantage by operating the downlink in the one-way mode while the transmitter was being tuned for acquisition. The two-way spectra are plotted in Fig. 17b with a spectral resolution of 0.984 Hz.

Note that the two-way spectrum is about 3 times as wide as the one-way spectrum. In his discussion Goldstein treats this as an anomalous result,* but he does remark that the transponder treats the signal in a nonlinear fashion. The transponder response was fast enough to track the phase variations that result from passage through the corona on the uplink, but the transponder did not reproduce amplitude variations. Instead the transponder generates a fixed amplitude at all times. In terms of the most recent models of the behavior of the solar corona, some of which have been published since Goldstein's report, we believe that we can explain the excess spectral broadening of the two-way signal in a reasonable way that is based on the nonlinear transponder response. In the following section that deals with scattering theory, we dwell on this point to some extent, because it brings out interesting consistency checks in our knowledge of the corona, and because it gives some insight into criteria for choosing an optimum frequency for studies of the corona.

In his attempt to understand the experimental results and relate them to the general body of knowledge, Goldstein performed an impressive number of checks and auxiliary experiments. Of course the ultimate check, a complete analysis and study of the performance of the spacecraft transponder, was not possible. However, he did determine that the spacecraft responded as expected to certain artificial signals which were intended to simulate the effects of corona at times when the line-of-sight was well removed from the corona. He also performed a number of checks using a transponder on the ground which was a duplicate of the spacecraft transponder. Finally Goldstein devoted a considerable amount of study to monitoring and analyzing the performance of the ground system. Among other things he noted excess noise when the position of the Sun occurred at particular values of the azimuthal angle ϕ about the axis of the antenna. These excess noise angles were 90° from the azimuthal angles of the quadripod legs which support the cassigrain reflector from the main 210 foot surface. This phenomenon was explained as side lobes generated by the quadripod legs which break the azimuthal symmetry of the antenna.

*Goldstein does suggest an explanation based on the difference in ground antenna areas for up- and downlinks, but this explanation has been disproven.

The Measurement of Interplanetary Electron Density with Pioneer VII

The Pioneer VII experiment was conducted during the fall and winter of 1966-67 by Koehler (Ref. 33) of Eshleman's group at Stanford University (Ref. 34). They used the Stanford 150 foot paraboloid antenna. This experiment differs from the others in three significant ways. First, the line-of-sight did not pass near the Sun. Second, the propagation experiment was performed entirely on the uplink; the downlink served only as a telemetry channel to return the data. Third, and most important for our purposes, is the use of two widely differing but harmonically related frequencies, namely 49.8 and 423.3 MHz, in the propagation experiment, i. e., the uplink in this case.

The importance of using two widely differing frequencies is that it provides two equations in two unknowns, so that both are soluble. The unknowns are the precise distance to the spacecraft and the integrated electron density along the line-of-sight to the spacecraft. Both unknowns affect the effective path length from Earth to spacecraft for determining the phase of the receive signal, that is the phase path or the number of cycles in the path times the wavelength. However, the effect of range on the phase path is independent of frequency, while the effect of electron density on the phase path varies inversely with the square of the frequency. Equation (3) evaluated for two frequencies permits a simultaneous solution for integrated or columnar electron density $I \equiv \int N_e ds$ and range R :

$$\left. \begin{array}{l} \text{phase} \\ \text{path} \end{array} \right\} = \int_0^R n(s) ds = \int_0^R \left(1 - \frac{40.3 \times 10^6 \text{ cm}^3 \text{ MHz}^2}{f^2} N_e(s) \right) ds, \quad (3)$$

where the variable s is distance along a radio ray from one station to the other. The two-frequency experiment worked very well and should be extended to any future solar radio probe which passes behind the Sun.

The above description is oversimplified, because discontinuous tracking causes complications that lose the R measurement, but retain the I measurement and its corona information. To evaluate the total phase path length for Eq. (3) one must count the total number of wavelengths along the line-of-sight from the Earth to spacecraft. To do this precisely with the two frequencies used, one would have to maintain continuous communications with the spacecraft and count cycles continuously after launch. This was impossible because there was no worldwide net assigned to the Pioneer propagation experiment, so the uplink was broken from the time the spacecraft set on the horizon at Stanford until it rose again half a day later.

The alternate method involved two modulation frequencies $f_m = 8.7$ and then 7.7 kHz imposed one at a time on both carriers. First consider the 8.7 kHz modulation. Owing to the different group velocities at the two

carrier frequencies, the modulation arrives with different phases on the two carriers, and the phase difference is a measure of columnar electron content I . The conversion of phase to I is accomplished by a graph such as that shown in the upper plot of Fig. 18 (except $f_m = 10^6$ Hz instead of 8.7 kHz in this graph), but more than one plausible value of I may result. For example, a measure of 0.1 cycle of phase could represent 1.1, 2.1, 3.1, ... etc. cycles. In other words there is a cycle ambiguity. This is resolved with the 7.7 kHz modulation which corresponds to the lower plot in the figure. (The same relative group time delay contains fewer cycles of lower f_m .) The point where the two plots agree on the same value of I (see arrow) is the true value.

Once the absolute value of I is established at the start of track, then it is possible to follow changes, both ΔI and ΔR , for the duration of track by the original simple method of Eq. (3). However, ionospheric perturbations are a real problem.

Much of Kochler's paper describes clever means for removing the effect of the electron content of the Earth's ionosphere from the experimental results. He introduced the useful term "Pioneer electron content," which means the integrated electron density all the way from the ground to the spacecraft, from which we wish to subtract the ionospheric electron content to determine the difference which is the interplanetary electron content. He used three techniques to determine the ionospheric content. The first could be performed 1 to 3 times daily during passes of the Beacon satellite. Two frequencies were received from the satellite, and the cycles of doppler shift were counted on each. This counted doppler range is an increment in the phase path to the satellite which can be used in Eq. (3) to determine the ionospheric electron content. However, the results represented only the average direction of Beacon and the particular time of the pass. The second technique was a crude one which removed the ionospheric content only to the extent that it followed a periodic diurnal cycle. This was done merely by removing the component of the Pioneer results that exhibited the diurnal periodic signature.

The third and most satisfactory technique for monitoring the ionosphere was provided by the launch of the geosynchronous ATS satellite. For a portion of the experimental period this satellite was continuously above the horizon as observed from Stanford. The Faraday effect, that is the rotation of the plane of polarization, was monitored at 137 MHz. This was done by slowly rotating an antenna with linear polarization and observing the antenna position that produced a null and signified that the antenna polarization was opposite to that of the incoming signal. During midday the Faraday effect caused approximately 7 half-turns of the polarization vector, so that measurement at midday is ambiguous since 7 half-turns is indistinguishable from 6 or any other integral number. However, the ambiguity was removed by tracking the polarization rotation into the night when it unwinds to less than one half-turn.

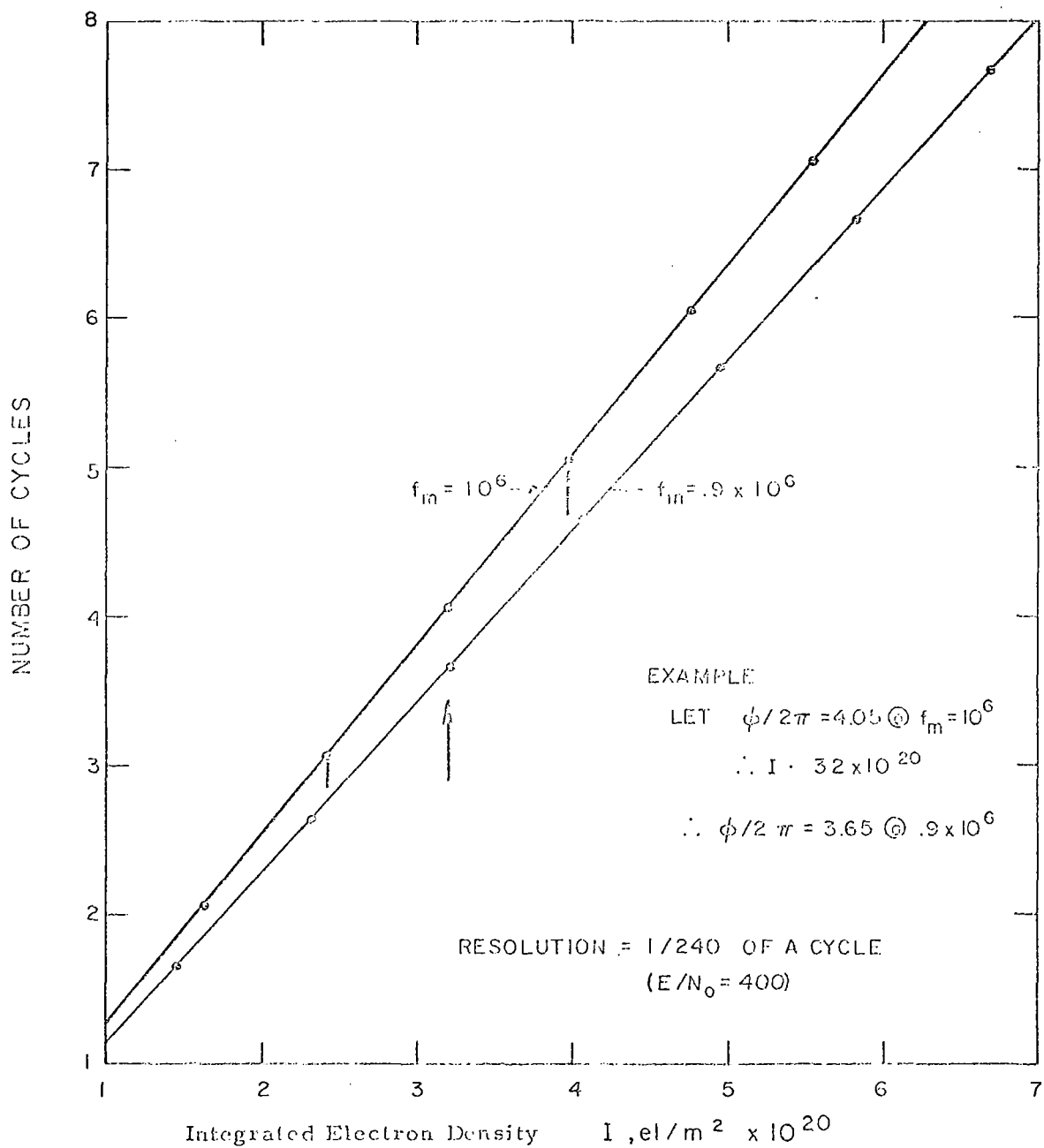


Figure 18 Resolution of Cycle Ambiguity with Two Modulating Frequencies

Koehler observed three strong events which were almost surely the passage of more or less spherical pulses of increased electron density. Koehler interpreted these as follows:

1. An event on October 24, 1966 was a pulse having a density of about 33×10^6 electrons/m³ and a radial width of 10.7 Gm, which traveled at 330 km/sec.
2. An event on November 10 was more difficult to interpret owing to uncertainties about the ionosphere.
3. The final event on January 25, 1967 can be interpreted well because the ionosphere was being monitored with the aid of the ATS satellite at that time. In summary it was a spherical pulse of 56×10^6 electrons/m³ having a radial width of 5.2 Gm and traveling at 350 km/sec.

Koehler mentions the possibility that pulses he observed were not necessarily radiating spherically from sudden events on the Sun. The pulse fronts were probably portions of an Archimedean spiral generated by the rotation of the Sun in a manner analogous to spiral spray from the rotating variety of water sprinkler.

RELATING RADIO MEASUREMENTS TO CORONA PROPERTIES

Radio astronomers use highly developed measurements techniques to monitor the emission from radio stars through the solar corona during occultation. The basic limitation of conventional radio astronomy is the fact that such sources are incoherent. In contrast, radio probes emit a coherent signal which allows measurements distinct from those of radio astronomy, thus yielding some of the solar corona parameters not attainable heretofore.

It is logical to divide possible solar plasma measurements in two classes according to whether one measures natural emissions from an incoherent source such as a radio star or man-made coherent signals from radio probes. Scintillation and scattering measurements belong to the first class while integrated electron density, frequency fluctuation and Faraday rotation belong to the latter. Obviously, we emphasize in this study those measurements which rely on the features of a coherent signal, since data of this type are scarce compared to those obtained by radio astronomers with noise sources. In particular, integrated electron density measurements have never been carried out close to the Sun; Pioneer VI and Mariner IV missions did not use the necessary two frequency system, and the Pioneer VII experiment did not extend to conjunction. Although frequency fluctuation (phase jitter bandwidth) was measured by Goldstein on the telemetry signals to four solar radii, the ensuing radio blackout revealed that the electron fluctuation near the Sun is highly structured (inhomogeneous). This indicates a need for additional measurements near the Sun at a frequency high enough (preferably X-band) to operate in the dense corona.

In the following subsections we describe the status of the various measurements we considered appropriate for a solar probe but we depart from rigidly adhering to the two classes mentioned above. The following Table IV summarizes the measurements we contemplate, the corona parameters that can be extracted from those measurements and the frequency dependence of the interaction between the measurement and the plasma itself. The table makes it clear that the plasma interaction decreases with increasing frequency but we shall see in the section on Measurement Accuracy that as frequency increases less energy is required per measurement for a given accuracy. This is so because noise temperature decreases with increasing frequency at such a rate that it more than compensates for the decreased interaction. In addition, there are more basic reasons for using higher frequencies, namely if the corona is as inhomogeneous as one expects from the Pioneer and Mariner measurements of jitter bandwidth, then high frequencies are necessary to penetrate the corona closer to the Sun; finally since higher frequencies mean weaker interactions the latter are more interpretable by perturbation theory, in particular when one measures scintillation.

TABLE IV MEASURABLE PARAMETERS

| Corona Parameter | Measurement | Frequency Dependence |
|---|--|---------------------------------|
| Columnar Electron Density $\equiv I = \int N_e ds$ | Pulse time delay, T_d , or phase delay ϕ_d in sinusoidal modulation on two carrier widely separated in frequency. | f^{-2} |
| Faraday Rotation $\int N_e H_{\parallel} ds$ | Direction of polarization vector | f^{-2} |
| Integrated Electron Density Fluctuation $\left[\langle \Delta N_e^2 \rangle ds \right]^{\frac{1}{2}}$ | Scintillation (signal amplitude fluctuation) $\frac{\Delta A}{A}$ | f^{-1} if weak interaction |
| Solar wind velocity a | Scattering Angle $\Delta\theta$ | f^{-2} |
| Blob Size u | Bandwidth of Phase Jitter B | f^{-1} |

The comparison of weak and strong plasma interaction for corona diagnosis is crudely analogous to the following optical situation. If a volume is full of very thin transparent balloons that are lighted from the back, then one can see through the front balloons and take size and shape statistics of layers further back. However, if the balloons are filled with water, for strong interaction with light, then only a bell shaped distribution function of scattered light can be measured. One can devise mathematical models for possible scatterers that would produce the observed scattering function, but more than one model is likely to produce the observed scattering function.

Fluctuations

Fluctuations in amplitude (scintillation), phase (jitter bandwidth), and angular spread (scattering) of the received signal are caused by random phase changes taking place along the ray path through the solar corona. As the solar eddies or blobs cross the propagation path, corresponding fluctuations in electron density occur, which in turn cause phase path fluctuations. Fluctuation measurements are important because they yield information on electron density fluctuation, ΔN_e , blob size a , and blob velocity u .

The analysis of fluctuations nearly always begins with the so-called thin phase-changing screen approximately illustrated in Fig. 19. Here we show two slabs of extended scattering medium with rays passing through them. The one on the left does not meet the thin screen criterion, and the one on the right does. On the left the cumulative scatters focus radiation on blob a , and off blob b . Hence the lever arm or length of each scatter is important, and the slab cannot be compressed to an equivalent thin screen. On the right the focussing is negligible on blobs c and d , so it may be collapsed into an equivalent thin screen that causes the same phase shifts. The mathematics for solving the scattering problem without the thin screen approximation are almost intractable. The strong scattering at 80 MHz (Sunblazer) would fall in this category for a wide range of important path offsets, but the thin screen approximation is valid in all cases for S-band and higher frequencies. Collision damping is negligible.

We begin the analysis by assuming a phase fluctuation function for the wavefront that emerges from the thin scattering screen:

$$\phi(x, y) = \phi_0 [\cos \alpha x + \cos \beta y] \quad (4)$$

The exact periodicity in this function is artificial of course, but the function is otherwise plausible as Figure 20 shows for $\sigma = \pi$, $\beta = \pi/3$. The exact periodicity gives rise to diffraction grating lobes that are too precise and may be smeared to obtain a good understanding of the true pattern from random blobs. Note the spatial average of ϕ^2 :

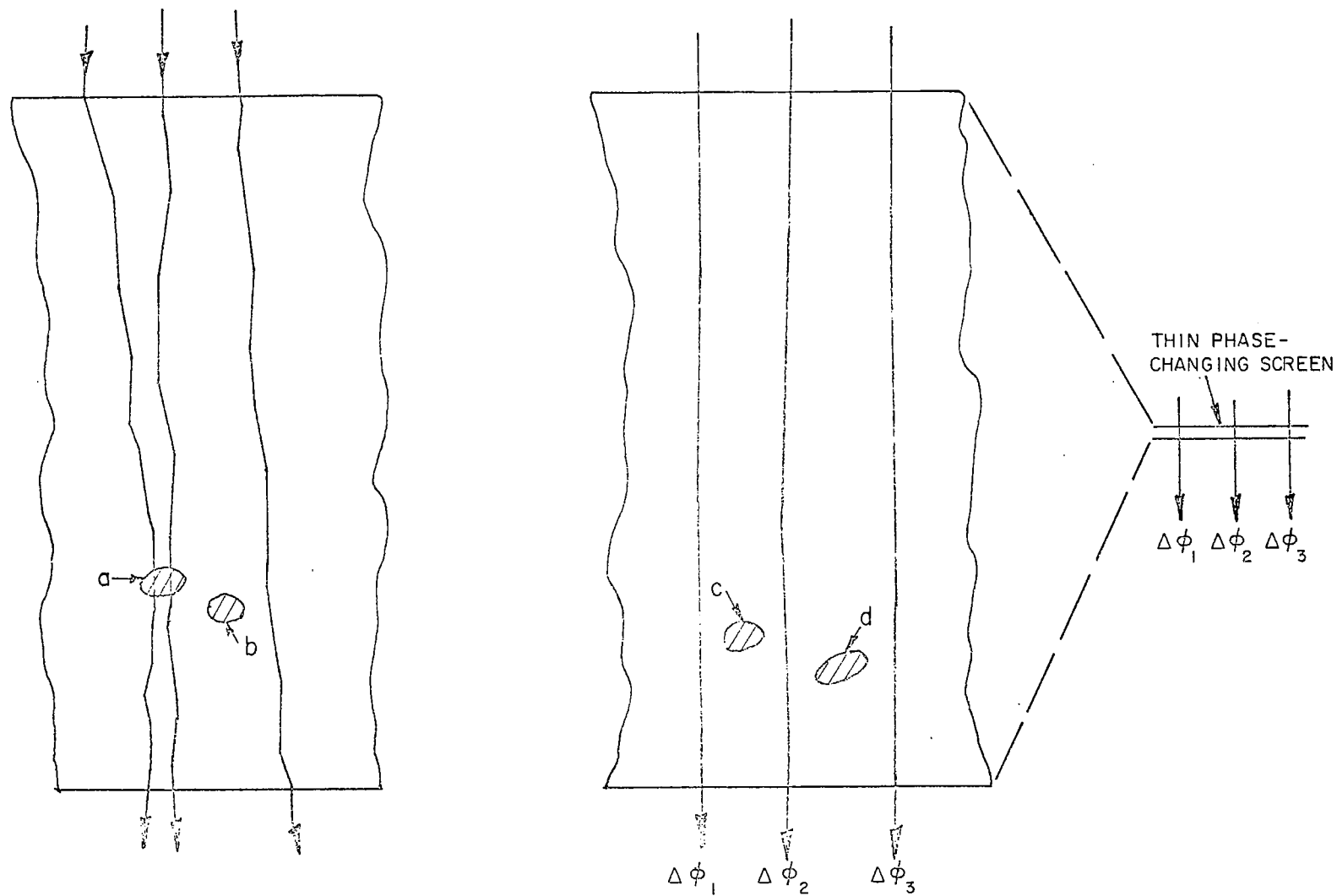


Figure 19 The thin phase-changing screen approximation in corona scattering theory. Approximation fails on the left screen, and is valid on the right.

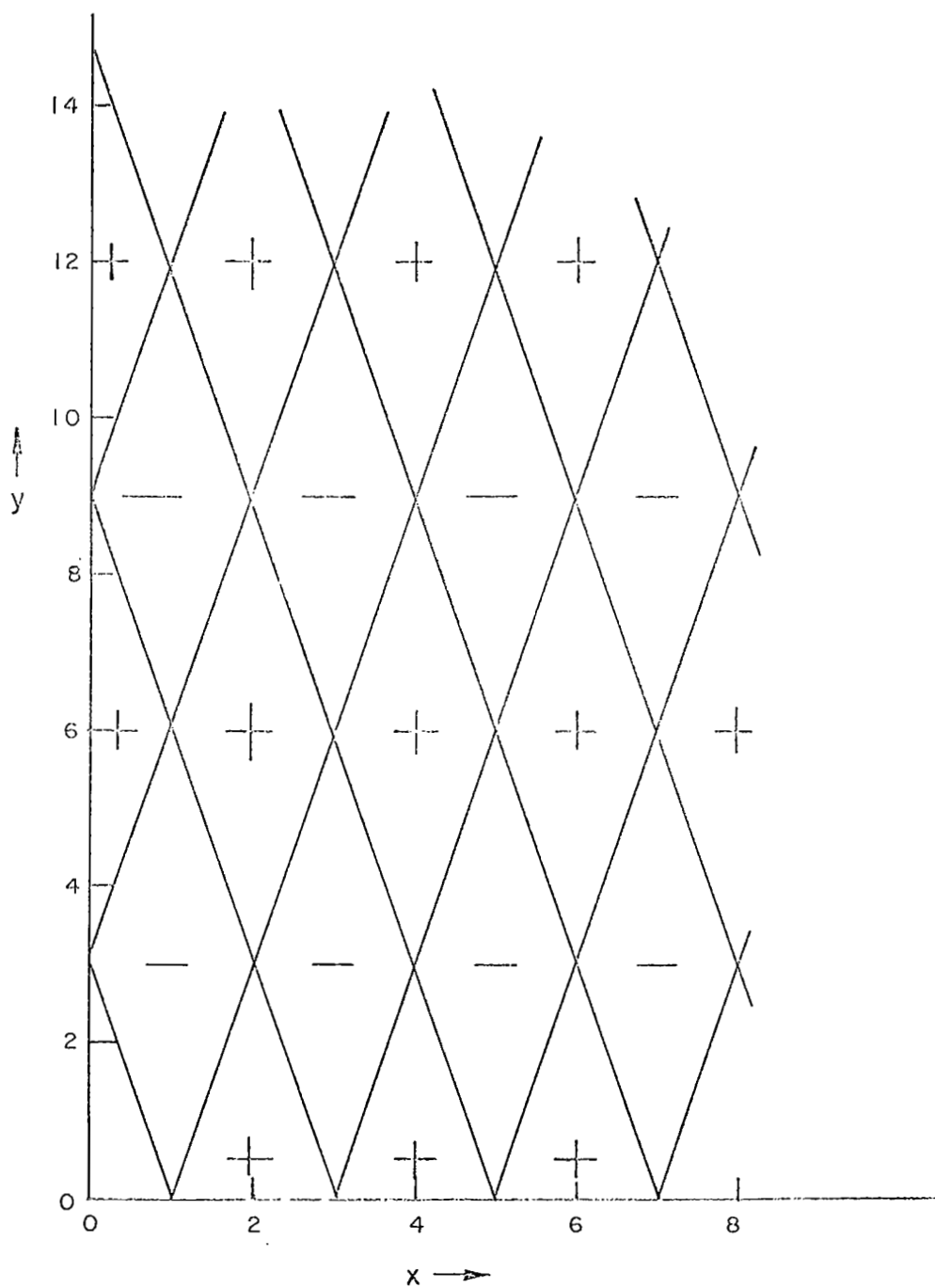


Figure 20 The function $\cos(\pi x) + \cos(\pi y/3)$. The diamond pattern is the locus of nulls. The values are ± 2 in the centers of the diamonds.

$$\langle \phi^2 \rangle_{sp} = \phi_0^2.$$

Also note the realism in the elongation of the filamentary blobs in the figure. The y direction is aligned with the magnetic field and corresponds to nearly the radial direction.

The geometry for performing the diffraction integration comes from Fig. 21. The integral for the signal received on Earth is

$$\psi(\xi, \eta) = N^2 \iint \exp[ik(x^2 + y^2)/z + i\phi(x - \xi, y - \eta)] dx dy, \quad (5)$$

where N^2 is the uninteresting normalization constant, ξ, η the coordinates on Earth $k = 2\pi / \lambda$ (carrier), $z = 1$ a.u., i.e., z is the distance from screen to both Earth and spacecraft, and we have put

$$\phi(x, y) \rightarrow \phi(x - \xi, y - \eta)$$

so that we can move the scattering screen corresponding to the solar wind; e.g., let $\xi = ut$. Note that z in Eq. (5) would be $2z$ for a radio star case since the incoming wavefront would be plane; i.e., there are differences between the formulae for the star and probe cases.

Equation (5) with ϕ from Eq. (4) factors into

$$\psi(\xi, \eta) = \psi_1(\xi, \alpha) \psi_1(\eta, \beta), \quad (6)$$

where the subscript stands for one-dimensional; explicitly

$$\psi_1(\xi, \alpha) = N \int \exp[ikx^2/z + i\phi_0 \cos \alpha(x - \xi)] dx \quad (7)$$

Equation (7) is evaluated in terms of the well-known Bessel functions expansion of modulation theory. The procedure is to expand $\exp[i\phi_0 \cos \alpha(x - \xi)]$ in a Fourier series and integrate. The result is

$$\begin{aligned} \psi_1(\xi, \alpha) &= \sum_{m=-\infty}^{m=\infty} i^m J_m(\phi_0) e^{im\alpha \xi} \exp\left(-i \frac{z}{k} \frac{m^2 \alpha^2}{4}\right) \\ &= J_0(\phi_0) + 2 \sum_{m=1}^{\infty} i^m J_m(\phi_0) e^{-i \frac{z}{k} \frac{m^2 \alpha^2}{4}} \cos m\alpha \xi \end{aligned} \quad (8)$$

In the above we have dropped an inconsequential normalization factor. Note that the higher the frequency, the smaller ϕ_0 and the faster the series converges.

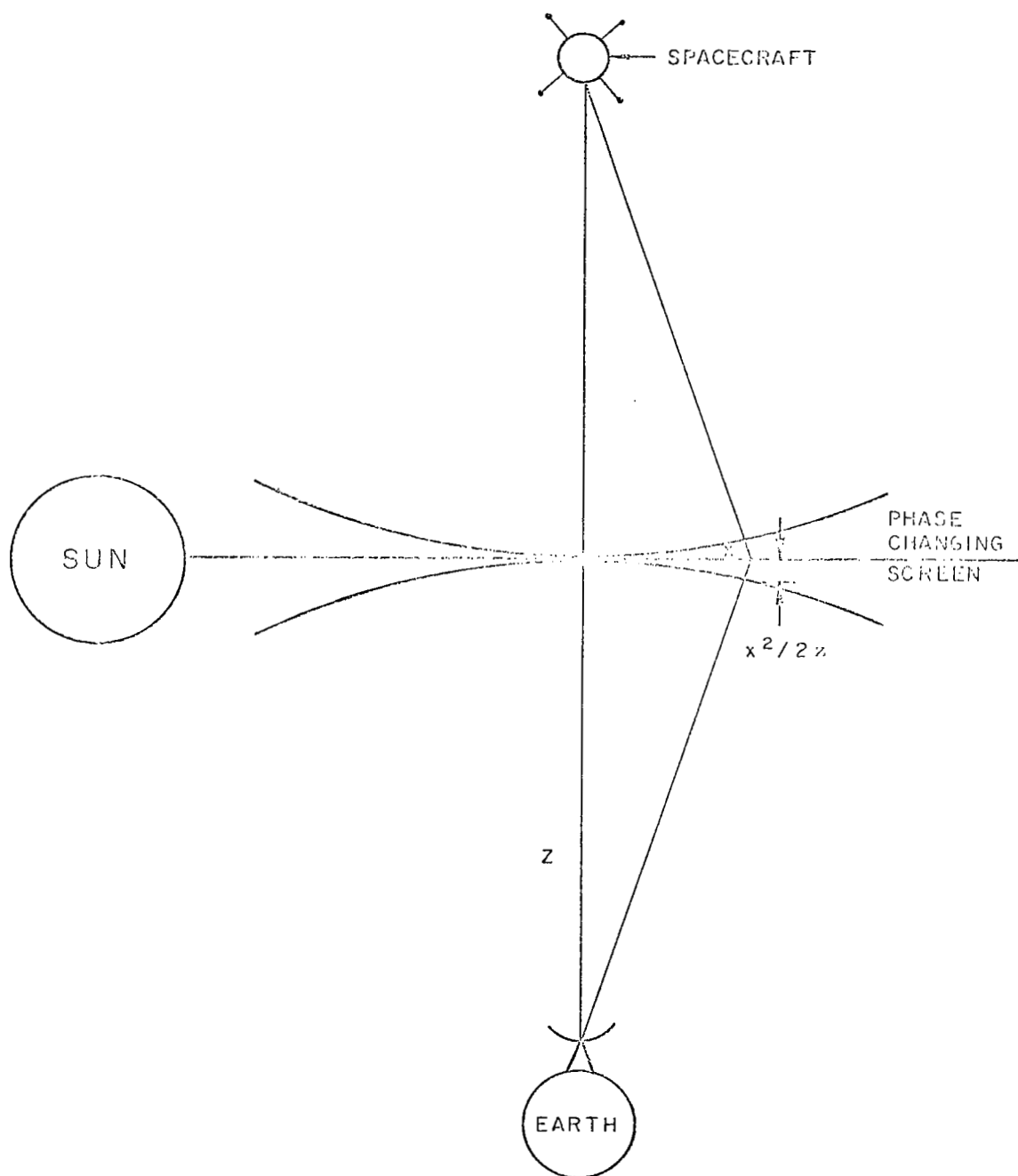


Figure 21 Scattering screen geometry

When the plasma interaction is small (high frequency), then $\phi_0 \ll 1$ and the terms $J_m(\phi_0) = (\phi_0/2)^m/m!$ decay rapidly. This explicitly demonstrates why higher frequency plasma interaction is so desirable. On a statistical basis with reference to other works, the desirability of $\phi_0 < 1$ has been explained by Little and Hewish (ref. 35).

To see the time dependence of scintillation and phase jitter in the received signal, put $\xi = ut$ for a moving solar wind. Then to first order (in m) the phase jitter comes from the $\cos(\alpha u t)$ term, i.e., the bandwidth is about $B = \alpha u$. However, for strong plasma interaction (low frequency) ϕ_0 is larger and the higher harmonics come in giving $B = m\alpha u$, where m is the index of terms in Eq. (8) that are large enough to be significant. Thus at low frequency when ϕ_0 is large, one must accept noise in a larger phase jitter bandwidth.

Recall Goldstein's experiment with Mariner IV in which the two-way bandwidth was 3.5 times greater than one-way, and this was not explained. In that case ϕ_0 was a little more than one radian, so the series converged in several terms. We offer the following very plausible explanation. The dominant terms of the series sometimes cancel out in the course of normal scintillation caused by interference of the first few harmonics (m values) in Eq. (8). The remaining weak terms have the higher frequency components, i.e., $\cos(m\alpha u t)$ etc. They contribute no more than usual on the one-way link, but the AGC effect of the Mariner transponder amplifies these wide band terms to full signal strength during the scintillation fades in the dominant terms.

So far we have merely discussed a single form (Eq. 4) for the phase shift caused by the whole scattering screen. In practice one must synthesize this shift from the multiple layers of blobs. In each layer the phase shift is just that caused by the refractive index difference Δn (Table I) between the blobs and the average for the plasma, i.e.,

$$\Delta\phi = 2\pi\Delta n a/\lambda,$$

where a is the average dimension of the blobs along the line of sight. As one expects, the $\Delta\phi$'s accumulate incoherently through the layers of blobs, so that ϕ_0 of Eq. (4) is the root of the sum of $\Delta\phi^2$. For a proof for the radio astronomy case, see Ref. 35, p. 229.

For some purposes, especially interferometry, it is well to express the results as a summation of plane waves. To do this we first go back to the diffraction integral (7) and introduce the z dependence of the signal originating at the distance $2z$ from earth (see Fig. 21), namely e^{i2kz} . The resultant expansion for the received signal

$$\psi_1(\varepsilon, \alpha, z) = \sum_{m=-\infty}^{m=\infty} i^m J_m(\Phi_0) e^{im\sigma\varepsilon} e^{i2kz(1 - \frac{m^2\alpha^2}{4k^2})} \quad (9)$$

exhibits the well-known fact that the signal at any point can be thought of a superposition of plane waves, each defined by a complex amplitude $i^m J_m e^{-i \frac{z}{k} \frac{m^2\alpha^2}{4}}$ and k vector inclination, $\theta_m = m \sin^{-1} \alpha/2k$ with respect to the z direction. The latter is easily seen if we relate the expansion (9) to a sum of plane waves defined by their direction,

$$\psi_1(\varepsilon, \alpha, z) = \sum_{m=-\infty}^{m=\infty} i^m J_m e^{i2k\varepsilon \sin m\theta} e^{i2kz \cos m\theta} \quad (10)$$

and identify the z and ε coefficients in the exponents of (10) with their corresponding part in (9), e. g. ,

$$\cos m\theta = 1 - m^2\alpha^2/(8k^2) \quad (11a)$$

$$\sin m\theta = m\alpha/(2k) \quad (11b)$$

We shall see later than even for large scattering $m^2\alpha^2/k^2 \ll 1$, hence

$\cos^2 m\theta + \sin^2 m\theta = 1$ to 2nd order in $m\alpha/k$ and the plane wave interpretation in terms of angular directions $m\theta$ is valid. We have then at any point a spectrum of plane waves arriving at discrete angles

$m \sin^{-1} \alpha/2k$ with respect to the z -direction. We can relate α to blob size a by first calculating a correlation function from Eq. (4) by averaging $\Phi(x, y)\Phi(x+\xi, y+\eta)$ over x and y . Then we can fit the curvature of the correlation at the origin to the usual model $\exp(-(x^2 + y^2)/2a)$ that defined blob size a . The result is*

$$\alpha = \sqrt{2}/a.$$

* Some authors use $(x^2 + y^2)/a$ with the result $\alpha = 2/a$.

the discrete angles at which the plane waves arrive are given by

$$\theta_m = m\lambda / (\sqrt{2} 2\pi a) \quad (12)$$

Each mode number, m in the expansion, gives rise to a pair of diffracted waves of successively higher order, $\pm m$, with respective relative energy, $2 J_m^2$. Note that the 1st order occurs at angle $\lambda/2a$ because the phase screen is illuminated by a point source at distance $2z$ instead of a plane wave from a star infinitely remote. For small scattering, $\Phi_0 \ll 1$ most of the energy of the received signal is contributed by the unscattered component of relative amplitude, $A_0 = J_0(\Phi_0) \approx 1$ (see Eq. 8). The only scattered energy that adds to the signal is the 1st order diffracted wave with a relative amplitude $\Delta A = 2J_1(\Phi_0) \approx \Phi_0$. For small scattering we see

from Eq. (8) that the signal is approximately given by

$$1 + i \Phi_0 e^{-i \frac{z}{k} \frac{\alpha^2}{4}} \cos \alpha \xi.$$

Maximum scintillation occurs whenever the scattered and the unscattered components are in phase or antiphase. First scintillation is where

$$\frac{z}{k} \frac{\alpha^2}{4} = \pi/2,$$

hence at $z_0 = a^2/\lambda$, in the near field of the blob. Since total intensity, I is proportional to the square of the resultant amplitude, $A = 1 + \Phi_0$, the relative intensity scintillation $\Delta I/I \approx 2\Phi_0$. For a sinusoidal phase screen, maximum scintillation or interference occurs at all z 's equal to odd multiples of a^2/λ . In reality, turbulence introduces randomness in the screen so that inhomogeneities in the plasma are roughly decorrelated beyond a distance equivalent to the blob size, a . As the distance, z increases above a^2/λ ; contributions from other blobs come in which are decorrelated, and scintillations caused by interference between scattered and unscattered components no longer oscillate and remain essentially constant. For distances $z < a^2/\lambda$ scintillations never build up to their relative level, Φ_0 . This is readily seen if we draw a phasor diagram, Fig. 22. At $z=0$, the scattered component of amplitude Φ_0 is in quadrature with the unscattered wave of unity amplitude and no scintillation occurs. As z increases, the phase described by modulus and argument $\Phi_0 e^{-i \frac{z}{k} \frac{\alpha^2}{4}}$ rotates clockwise and its in-phase component $\Phi_0 \sin \frac{z}{k} \frac{\alpha^2}{4}$ interferes with the unscattered wave so as to produce scintillation. Obviously maximum intensity scintillation takes place when the phasor is in antiphase with the unscattered wave and its argument $\frac{z}{k} \frac{\alpha^2}{4} = \pi/2$. For distance $z \ll z_0$, the antiphase component has magnitude $\Phi_0 z/z_0$ and the resultant intensity scintillation is reduced by the same ratio.

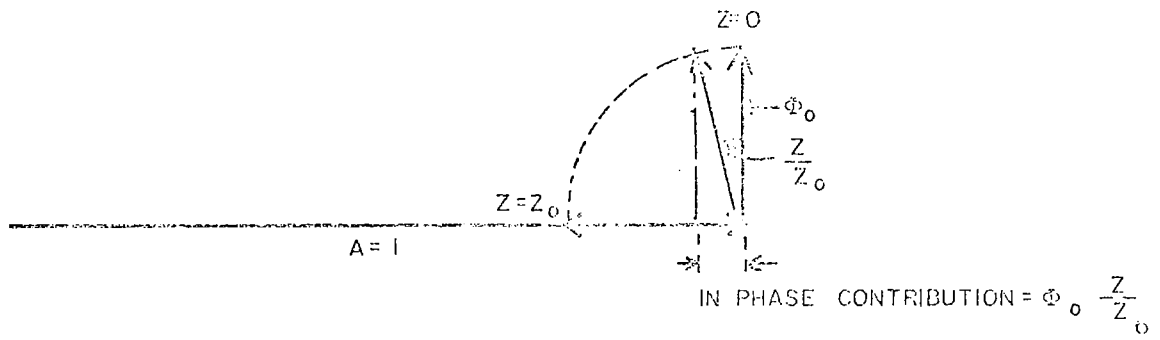


Fig. 22 Phasor diagram of unscattered and 1st. order scattered wave

For large phase fluctuations, $\phi_0 \gg 1$ the expansion (8) shows that higher order scattered waves contribute to the received signal in a manner totally analogous to the side bands of phase modulated signals in communication theory. It is well known from communication theory and the properties of Bessel function that for large phase deviation the significant number of side bands is $m \approx \phi_0$ and that most of the energy is concentrated around the m th-order as shown in Appendix 3. Thus in the case of large phase fluctuation, the closest integer to ϕ_0 is approximately the number of significant pairs of scattered waves contributing to the received signal. Thus we see that weak scattering diffracts energy within a half-cone angle $\pm \alpha/2k$ about the z - axis, with most of the energy undeflected and relative intensity scintillation $\Delta I/I \approx 2\phi_0$. Large scattering refracts the bulk of the energy in the direction $\pm \phi_0 \alpha/2k$ corresponding to the maximum slope of the phase distribution on the screen while the relative scintillation, $\Delta I/I \approx 1$. At low frequencies, say VHF where the plasma-wave interaction is large, the phase fluctuation, ϕ_0 over the propagation path exceeds many radians, strong scattering predominates so that no scintillation is observed and no corona diagnostics is possible as explained in p. 53 of this report. The situation is summarized in the scattering regime diagram, Fig. 23a based on the convergence of the expansion (8) in ϕ_0 . The figure is consistent with radio astronomy data from Ref. 27. Beyond the distance z_0 from the scattering screen, the receiver is in the far field of the blob. Lines superposed on this diagram show the movement of a spacecraft across the diagram for various frequencies and path offsets marked as dots labeled in solar radii. As mentioned above plasma diagnostics is only possible in the weak scattering regime since measured scintillation yield directly the phase fluctuation ϕ_0 which is a measure of the integrated electron density fluctuation $\langle \Delta N_e^2 \rangle$ as shown in Table IV. This is a strong argument for using as high frequencies as possible.

Figure 23b shows the frequency range available for weak plasma interaction as a function of path offset. The usual NASA S-band links enter strong scattering at 7.5 solrad, and even X-band at 3 solrad. This does not necessarily spoil the experiment at these offsets, but it surely becomes more difficult to retain phase lock and interpret data for points far into the strong region.

If we put in the time dependance $\xi = ut$ into Eq. (8) to account for the moving solar wind, we see right away that for small ϕ_0 , the signal fluctuates as $A + \Delta A \cos \alpha ut$, A being a complex number. The scintillation spectrum caused by this wave interference has radian bandwidth $B = \sigma u$ so that if we know the solar wind u we can get the scale of turbulence through σ . On the other hand for large ϕ_0 , the received energy spreads to the higher diffraction order $m \sim \phi_0$. The spectrum not only has much larger bandwidth, $m\sigma u$ but since the bulk of the energy is concentrated in the m th order diffraction we cannot resolve fluctuation scales larger than $1/m\sigma$, or of the order of a/ϕ_0 . The strong plasma interaction occurring at low frequencies gives rise to such large phase fluctuation that no measure of the turbulence scale is possible. This is another strong argument against using frequencies smaller than X-band for a solar corona propagation experiment.

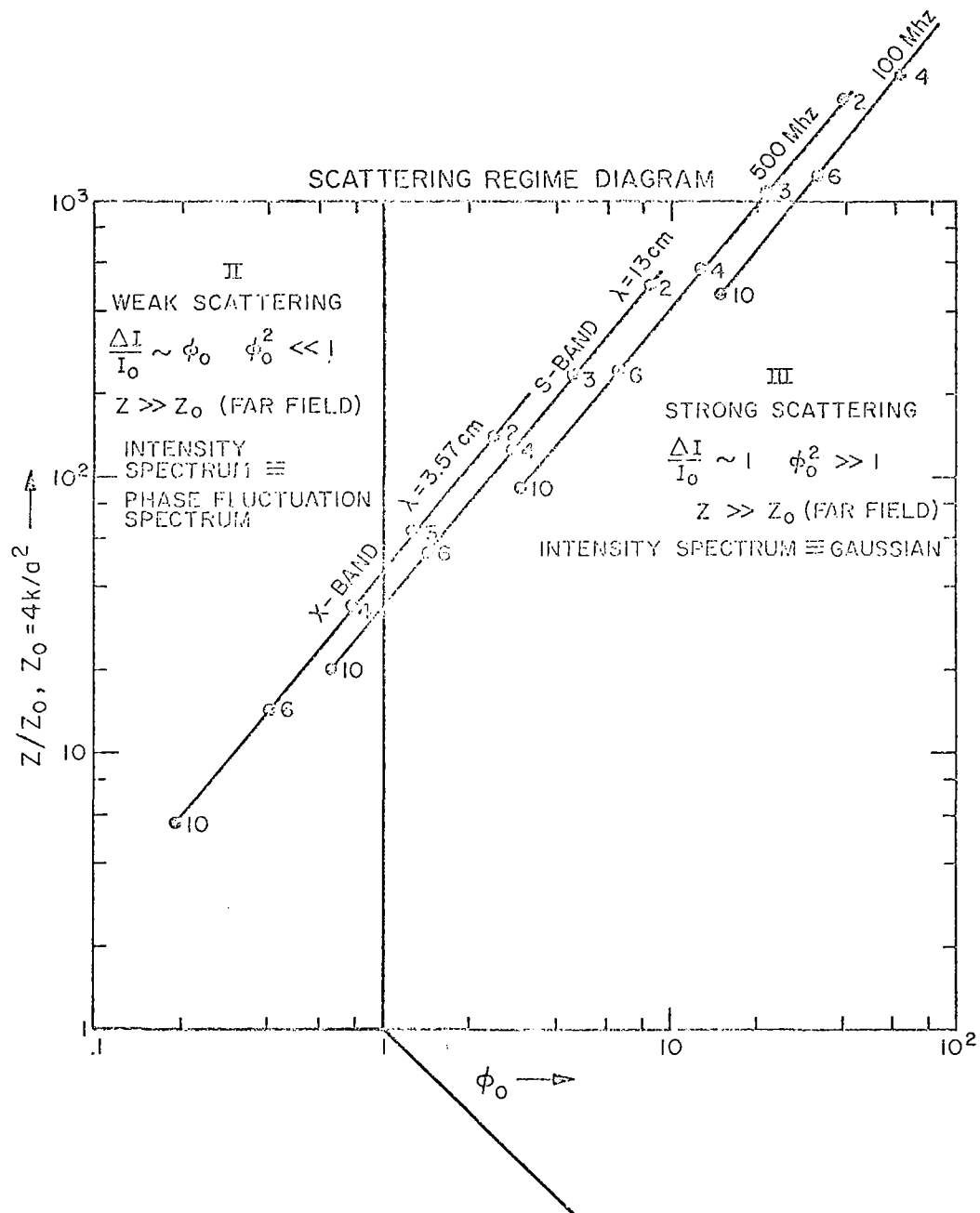


Figure 23 a Scattering Regime Diagram, after Cohen, Gundermann, Hartree, and Sharp

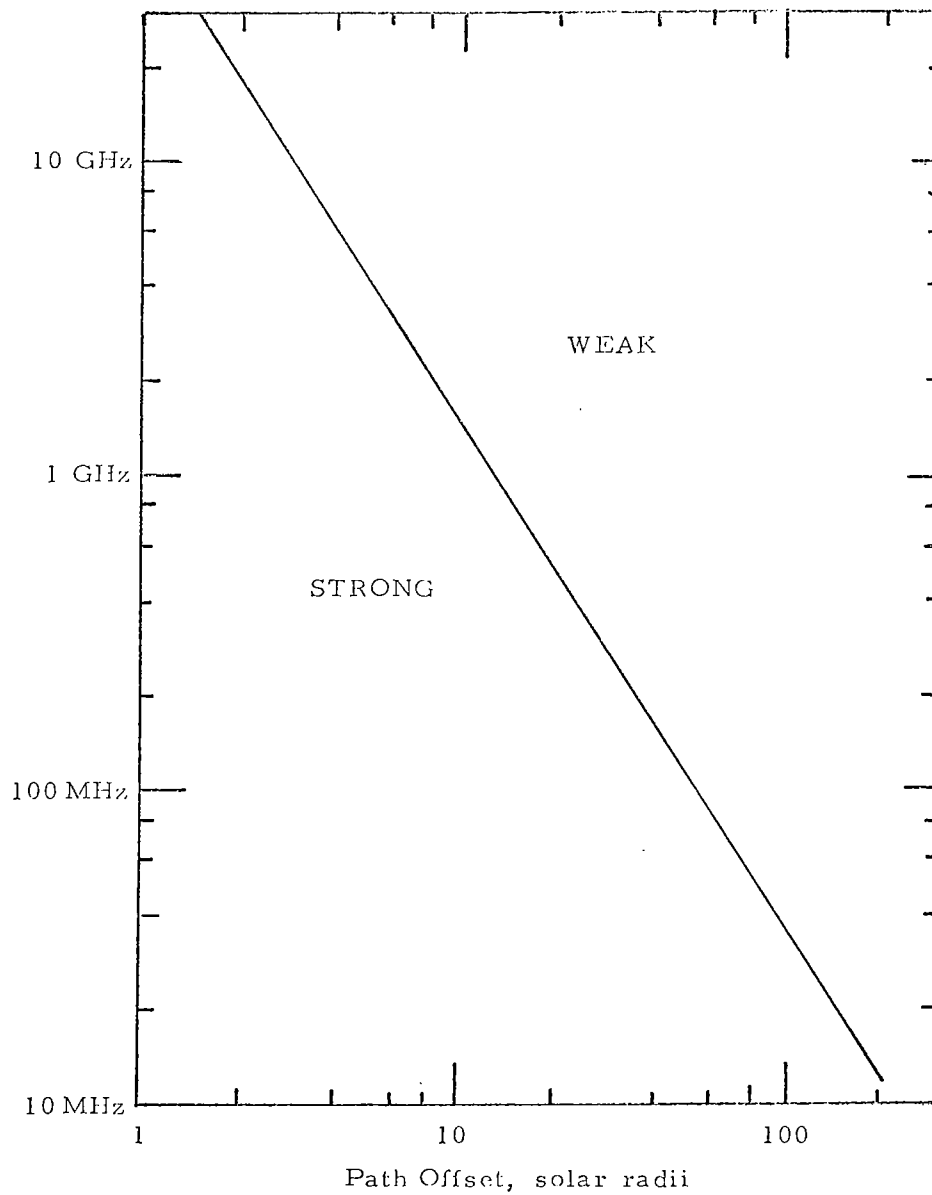


Figure 2 3b Condition for Weak Interaction $\phi_o = 1$ radian, after Hewish and Symonds (Ref. 24)

Another shortcoming of the large phase fluctuations inherent in low frequencies is that the scintillation spectrum bandwidth requires a phase locked loop receiver to have the same bandwidth in order to accommodate the phase jitter $\phi_0 \alpha$ radians/sec. Now let us call channel coherence time, T_c the time for solar wind inhomogeneities of size $a = \sqrt{2}/\alpha$ and velocity u to cross the propagation path. The resulting bandwidth $B = \sqrt{2} \phi_0 / (2\pi T_c)$ Hz is much larger than the inverse of the coherence time.

On the other hand, for small phase deviation, $m = 1$, the required phase locked loop bandwidth $= 1/T_c$ Hz is much smaller. We have then two bandwidths, $1/T_c$ determined by the stationarity of the propagation path and, $\sqrt{2} \phi_0 / (2\pi T_c)$ related to the rate of change of the total phase shift along that path. The latter is calculated in Appendix 4 and a comparison of theory and experiment is shown in Fig. 24 as a function of path offset. The discrepancy is due to lack of knowledge of blob size and velocity as a function of path offset. In the Link Analysis Sec. III we use an average of the experimental curves marked Mariner IV and Pioneer II. These were scaled as $1/f$ in Table IV for other frequencies.

Image Blur Circle

The purpose of this subsection is to calculate the angular spread in the direction of incoming rays after passage through the solar corona. In optical astronomy, the analogous spread is called a blur circle, so we use the same term for consistency. We can gain some insight by estimating the rms angular deviation $\Delta\theta$ from data that were originally derived from scintillation observations (intensity fluctuations). We then compare the estimates to direct measurements of $\Delta\theta$.

We could perform a diffraction analysis as in the preceding subsection for the scattering angle. The difference is that we have to add a factor for the thin lobe of a radio interferometer capable of resolving the small angular size. However, it is more instructive at this point to make an intuitive estimate and show that this gives good results. Details of the deviation are given in Appendix 5 where we find

$$\Delta\theta(\text{rms}) = \frac{107.84}{f^2} \left(\frac{47.1}{b^{4.21}} + \frac{0.27}{b^{3.21}} \right)^{\frac{1}{2}}, \quad (12)$$

where f is in MHz, $\Delta\theta$ in radian, and b is in sol. rad.

Experimental values of $\Delta \theta^2$ from Snee's data appear in Fig. 10. His data are compared to a plot of the preceding equation, Fig. 10. Our estimates are too small by a factor of 5 near 20 sol. rad. and a factor of 2 near 200 sol. rad. This discrepancy is not out of reason considering the time of the solar cycle for the two sets of data. A further cause of the discrepancy appears in the nonlinear dependence of $\langle \Delta \theta^2 \rangle$ upon a (see Appendix). This means that any statistical moment of θ , such as the variance we are treating, depends on many higher moments of a . However, in our estimate we have used only the average value of a for lack of further data. Had the higher moments been available, we would have used

$$\begin{aligned} \left\langle \frac{1}{a} \right\rangle &= \left\langle \frac{1}{\langle a \rangle + \Delta a} \right\rangle = \left\langle \frac{1}{\langle a \rangle} - \frac{\Delta a}{\langle a \rangle^2} + \frac{(\Delta a)^2}{\langle a \rangle^3} - \dots \right\rangle \\ &= \frac{1}{\langle a \rangle} + \frac{\langle \Delta a^2 \rangle}{\langle a \rangle^3} + \frac{\langle \Delta a^4 \rangle}{\langle a \rangle^5} + \dots, \end{aligned}$$

or better yet, moments of the joint distribution of ΔN and a . The point here is that the neglected terms are positive, the proper sign to help explain the discrepancy.

Various observers (Ref. 8) have noted sporadic intense events in the corona. This suggests that statistics of various quantities have long-tailed distribution functions, which in turn implies that the higher moments are larger than they would be for normal statistics. Sporadic events tend to dissipate and approach normal statistics at great distances from the sun; therefore, it is noteworthy that the discrepancy in the graph diminishes at great distances.

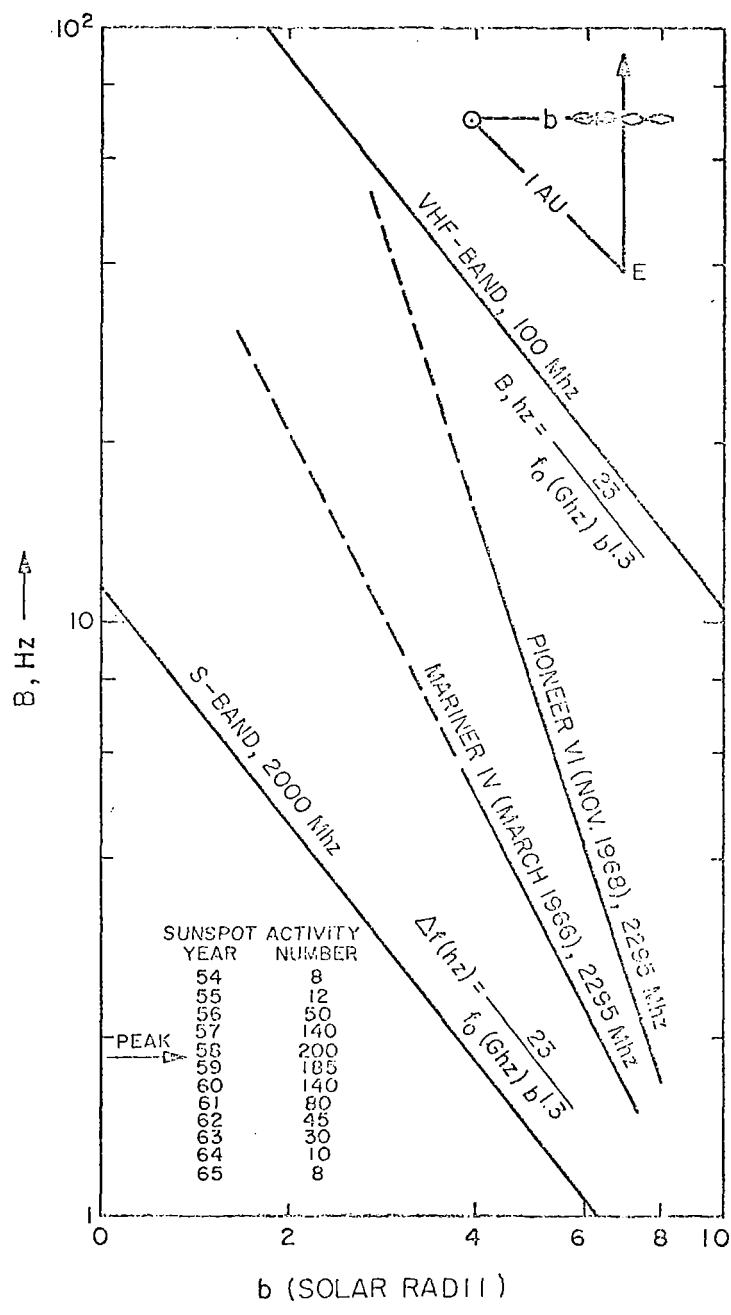


Figure 24 Phase jitter bandwidth vs path offset

Measurement Accuracy in Terms of Signal-to-Noise Ratio

Noise limits the ultimate fineness of a measurement. The smallest increment that can be measured cannot be smaller than the noise fluctuations in the system. Take for instance the measurement of time delay T_d between two pulsed carriers. After r.f. detection, the

pulse of width T_B and amplitude A is impressed on a matched filter of unity gain. The matched filter correlates the input with itself. If the noise level is $\sqrt{P_N}$, the timing error $\Delta T = \sqrt{P_N} \frac{T_B}{A}$. Since the

carrier power $P = \frac{1}{2}A^2$, $\Delta T_d = T_B / \sqrt{2P_s / P_N}$ or in terms of received

energy $\Delta T_d = T_B \sqrt{2E/N}$. To be exact there is an additional timing error for the pulse at the second frequency so that strictly speaking the total error should be $\sqrt{2}$ times as high. As expected, the fineness of the measurement is inversely proportional to the signal-to-noise ratio. The relative measurement accuracy, assuming the second

frequency much higher $F^2 \gg f^2$ is

$$\frac{\Delta T_d}{T_d} = \frac{T_B \left(2 E/N \right)^{-\frac{1}{2}}}{1.35 \times 10^{-7} f f^{-2}} \quad (\text{MKS units})$$

$I = \int N_e dl$ is the integrated electron density along the ray path;

T_B of the order of the rise time as shown in Appendix 1 is inversely proportional to $f^{3/2}$. Since T_d is proportional to I , the above

is also the relative accuracy with which I can be determined. It is convenient to express the received energy-to-noise ratio E/N , in terms of the transmitted directive energy, $E_T G_T$, the noise temperature of the receiving system, T_N and the capture area A of the receiver,

$$\frac{E}{N_0} = \frac{E_T G_T}{4\pi R^2} \frac{A}{kT_N} \quad (\text{Range Equation})$$

The preceding two equations together with the rise time expression of Appendix 1 yield a useful quantity for comparing various systems,

$E_T (\Delta T_d / T_d)^2$; it is the relative error times the transmitted energy and

it depends only on the following three system parameter, f , T_N , A .

$$E_T \left(\frac{\Delta T_d}{T_d} \right)^2 \sim f \frac{T_N}{A}$$

The left-hand expression rewritten as $\frac{E_T}{(T_d / \Delta_d)^2}$ is recognized

as the required energy per resolvable measurements, for a given columnar electron density, I . This expression is a useful figure of merit to compare candidate systems for the downlink experiments since the spacecraft imposes an upper limit on available energy. The explicit frequency dependence, f on the right hand side of the equation comes about from the decreased interaction between plasma and measurement. As frequency increases, more energy is required to achieve the same accuracy if everything else is constant. However, noise temperature in a downlink system goes down with frequency, in general at a faster rate than $1/f$ so that it more than compensates for the decreased interaction. As we shall see in the section on Link Analysis, the overall result is that higher frequencies require less energy for measurement in downlink experiments.

If instead of pulses we use two phase modulated CW carriers as in the Pioneer experiment, we find again the same dependence on f , T_N and A for the energy,

$$E_T \left(\frac{\Delta \varphi_d}{\varphi_d} \right)^2$$

required by resolvable measurement. In this case the phase error is

simply $\Delta \varphi_d = (2E/No)^{-1/2}$ while the phase delay φ_d varies as f_m/f^2 .

The modulating frequency f_m here plays the same role as the pulse width since they are related by $f_m \approx 1/T_B$.

It is a simple matter to generalize the above results; namely if we measure a variable, v such as T_d , φ_d with a measuring function $m(v)$, the minimum measurable increment $m(v)$ is

$$P_N^{1/2} / m'(v)$$

where m' is the maximum slope of the measuring function. The square root only applies if the measurement is based on amplitudes. For power measurements, $\Delta v = \frac{P_N}{m'(v)}$.

Uplink Interferometry

Measurements of scattering angles by radio interferometry have been so useful, that we do not wish to sacrifice this capability in an uplink experiment. Even though scattering is a quantity that can be measured with radio stars, it is desirable to measure the scattering caused by the same solar events being measured in other ways by the spacecraft experiment. Fig. 25 shows a way to retain interferometry, but only at the expense of complicating spacecraft data reduction. One station transmits a slightly higher frequency than the other, so that lobes sweep across the spacecraft. The spacecraft receives an amplitude modulated signal, and the jitter on this modulation is a measure of the scattering angle in the corona.

If the antennas are too far apart, i. e., lobes too close together, then the jitter in the lobe angle will exceed the lobe spacing, and results will be difficult to interpret. The shortest interferometer baseline is needed for short path offset, say 3 solrad. The spacings appropriate to this offset are given in the Fig. 25

Columnar Electron Density and Faraday Rotation

For the most part these topics have been discussed sufficiently. Columnar density is treated briefly in the Spacecraft Experiment section and under Link Analysis. Further discussion appears in papers by Koehler (Ref. 33) and Eshleman (Ref. 34), and unpublished reports of the Stanford group and the MIT Sunblazer group.

Faraday rotation is discussed in the Spacecraft Experiment section and by Levy, et al (Ref. 30), and the other papers and reports just mentioned.

One added point on this subject is that the two frequencies required for the electron density measurement must propagate in the same direction that is both uplink or both downlink. This is not a strict limit imposed by physical law, but rather a practical result. Consider what happens if we attempt to count the number of cycles of two carrier frequencies, one on the uplink and one on the downlink. In order to compare the two counts the frequencies must both be derived from a precise frequency standard, and the counting of each must terminate at the same time. This requires the synchronization of a clock on board the spacecraft with a clock on the ground. If this is done by sending synch signals to the spacecraft, those signals have to be on a separate carrier to remove the effects of electron density. This separate carrier then establishes two uplink frequencies which may as well be the experimental frequencies and the downlink is not needed for that purpose.

However, if the spacecraft clock is synchronized with the ground clock by means of its own built-in precision, this would require an atomic clock in the craft, which implies considerable development risk, since

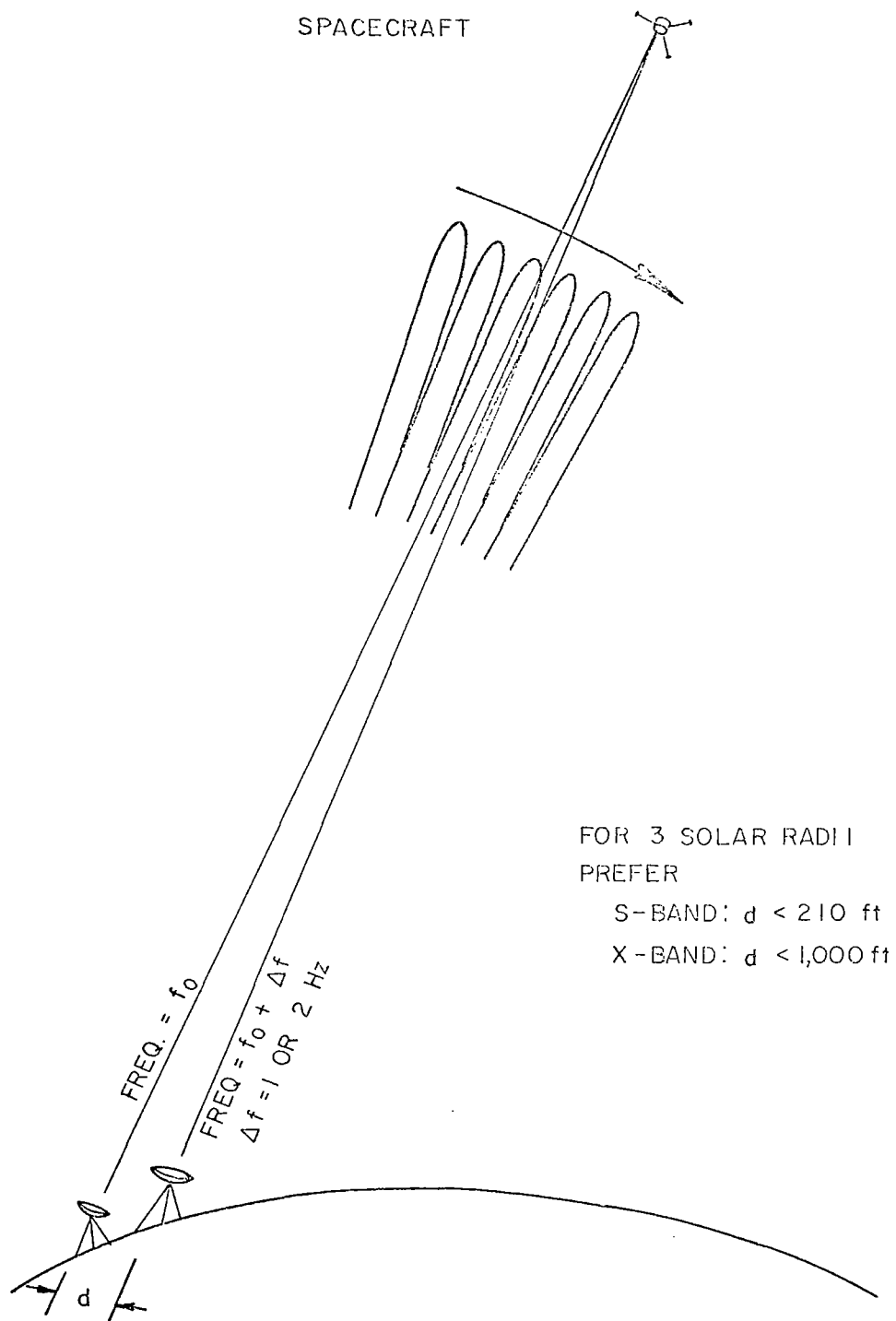


Figure 25 Fan-beam lobes of an uplink interferometer sweeping across the spacecraft

there is no precedent for sending atomic clocks on deep space probes. Moreover, the equipment that is put on a spacecraft should be designed in such a way that failures produce obvious effects, so that the experimenter knows there has been a failure. If frequency and time signals in the spacecraft are derived from a precision clock, the experimenter on the ground is never completely sure that the clock has maintained its designed precision. However, if the downlink frequency is derived from the uplink frequency by the familiar techniques of frequency multiplication and addition, then it is almost impossible to have a failure that would only produce a slow drift between the two. Any failure in the spacecraft system would be identified by a failure of the downlink to track the phase of the uplink. When uplink and downlink signals are harmonically related in this manner a cycle count does not provide two independent measurements of spacecraft range and plasma density. Rather, it gives a single measurement of round trip range and plasma density, from which one can derive only one equation in the two unknowns.

PROPAGATION LINK ANALYSIS

The purpose of the Sunblazer experiment is to measure (1) Faraday rotation, (2) fluctuations in phase, angle and intensity of the radio signal, and especially (3) integrated electron density $I(\text{el}/\text{m}^2)$. These measurements are related to parameters of the solar corona as discussed in detail in the preceeding section. This section is devoted to determining the frequency at which the measurements should be made, and whether an uplink or downlink should be used for the propagation experiment. By definition an uplink has its transmitter located on earth and receiver in the spacecraft, and a downlink vice versa. The following link analysis proceeds as follows: (1) the optimum downlink frequencies are determined, (2) the optimum uplink frequencies are determined, S and X-band, and (3) a decision is made that uplink is preferable to downlink.

Most of our studies to date have assumed that the receiving antenna is pointed in the normal way to receive the maximum amount of signal strength. However, for some candidate systems it would be advantageous to point a null of the antenna pattern at the Sun, the major source of noise, even though this sacrifices a considerable amount of signal strength. This introduces a number of complex considerations; for example, is it feasible to widen a null of the antenna pattern to encompass the whole Sun, or is there an even more advantageous pointing direction somewhere between the null pointing and normal pointing mentioned above? Owing to considerations such as these, a truly complete trade-off study of the various links is a more prolonged activity.

Since the integrated electron density (I) is the most important quantity to measure it receives the most attention in this section. Also, as shown in the preceeding section, if a measurement of I can be made with satisfactory accuracy at a given frequency, then the three fluctuations (frequency, amplitude and angle) can be measured at that frequency with similar accuracy.

Integrated Electron Density (I) Measurement

It is well-known that the group delay of a signal or time advance of a phase front propagating through a plasma is given by:

$$T_d = \frac{1.35 \times 10^{-7}}{f^2} I \text{ (sec)} \quad (13)$$

where I = integrated electron density (el/m^2) and
 f = carrier frequency (Hertz),

assumed to be much higher than the plasma resonance. To determine I therefore one need only know the group delay of the signal with respect to a signal which has propagated through a vacuum. Since a vacuum

cannot be arranged in the corona, two signals at different frequencies are required and the relative group delay is measured. The group delay is usually large with respect to the carrier period, and some type of modulation is required to define the group. We will briefly examine three possibilities.

Ranging Code. - The use of two pulsed carriers is a simple method by which relative group time delay could be measured. Unfortunately practical problems arise. Timing accuracy of a pulsed signal as measured by a matched filter receiver is given by:

$$\Delta = \frac{1}{2} T_B (E/N_0)^{-\frac{1}{2}} \quad (14)$$

where Δ = rms timing error
 T_B = pulse rise time
 E/N_0 = ratio of received signal energy to noise energy.

As seen in Eq. 14, the rms timing error improves as rise time T_B is reduced, which in turn relieves the requirement for high E/N_0 . But as T_B is reduced the transmitter peak power must be increased. Peak power, however cannot normally be increased as easily as T_B is decreased, so this reasoning leads to a transmitter operating at its peak power capacity but well below its average power capacity. A ranging code eliminates this problem by making use of the total transmitter average power as T_B is reduced.

The essential property of a ranging code is that it has an autocorrelation function which approximates a delta function. For binary encoded digital signals a typical autocorrelation function is shown in Fig. 26.

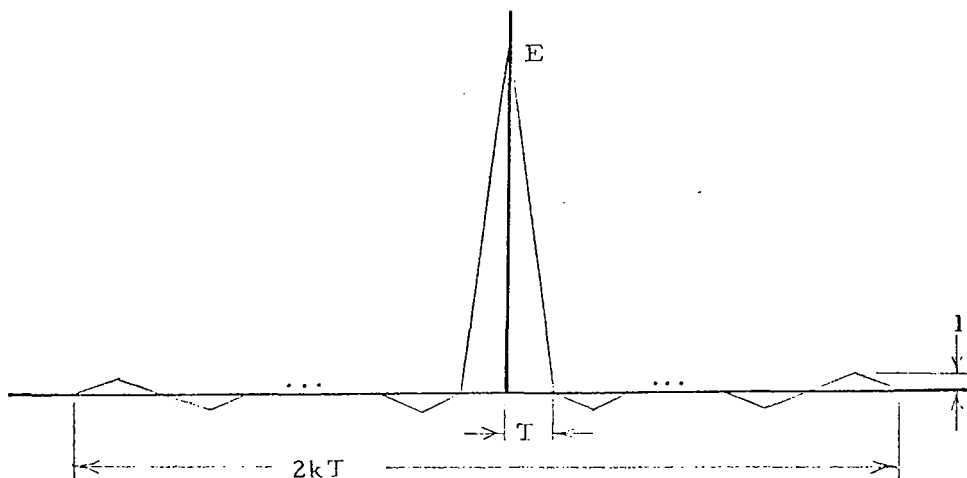


Figure 26. Autocorrelation Function of a Binary Ranging Code

In Fig. 26 E is the energy in the ranging code and K is the number of binary digits (bits).

Figure 27 shows a typical receiver used to determine group time delay. Phase shift keying ($0^\circ/180^\circ$) is used to modulate the carrier with the ranging code (denoted by $f(t)$). The received signal is coherently demodulated by means of a phase locked loop and then the autocorrelation function shown in Fig. 26 is obtained. The number of correlators required is dependent upon K , the number of bits in the code, and the number of points required to trace out the part of the autocorrelation function where the peak is expected. The number of correlations may be greater than $2K$ but probably less than $20K$. Once the autocorrelation functions are obtained from both carriers the relative time delay is obtained directly. An obvious disadvantage of the ranging code method is the receiver. As illustrated in Fig. 27 it could become very complex. This eliminates range codes from the preferred uplink mode.

Phase Modulation. - The Pioneer VI and VII used phase-modulation to measure I . Two carriers (50 MHz/425 MHz) were phase modulated at 7.7 kHz or 8.7 kHz rates; a small modulation index ($\approx 1/2$) was used. This system is considerably simpler than the ranging code method, however, it has a minor drawback in that I is large enough to cause relative time delays greater than one period of the modulation frequency. Ambiguities result which can be resolved by first measuring the phase on one modulation frequency and then switching to the other modulation frequency and measuring its phase shift. In the case of Pioneer up to ten cycles of ambiguity were resolved in this manner.

The receiver concept for the phase modulation method used in the Pioneer experiment is shown in Fig. 28. It basically consists of four phase lock loops. The receiver outputs, which were telemetered to Earth, are (1) channel phase jitter and (2) modulation phase shift (group time) at each of the two carrier frequencies.

Amplitude Modulation. - We have considered and rejected the use of amplitude modulation. The main reasons for rejection are: (1) possible transmitter linearity problems, and (2) inefficient average power utilization of the transmitter.

Briefly the amplitude modulation receiver for measuring group time delay and channel phase jitter would be very similar to the receiver of Fig. 28. The use of phase lock loops would be required for coherent demodulation in order to achieve maximum output signal-to-noise ratio.

Phase Lock Loop - The Important Receiver Component. - A phase lock loop must be used in deep space experiments because the low signal-to-noise ratios demand coherent reception with maximum noise rejection by using prior knowledge about the signal (phase). If signal-to-noise ratio (S/N) is inadequate for satisfactory phase lock loop operation we can conclude that

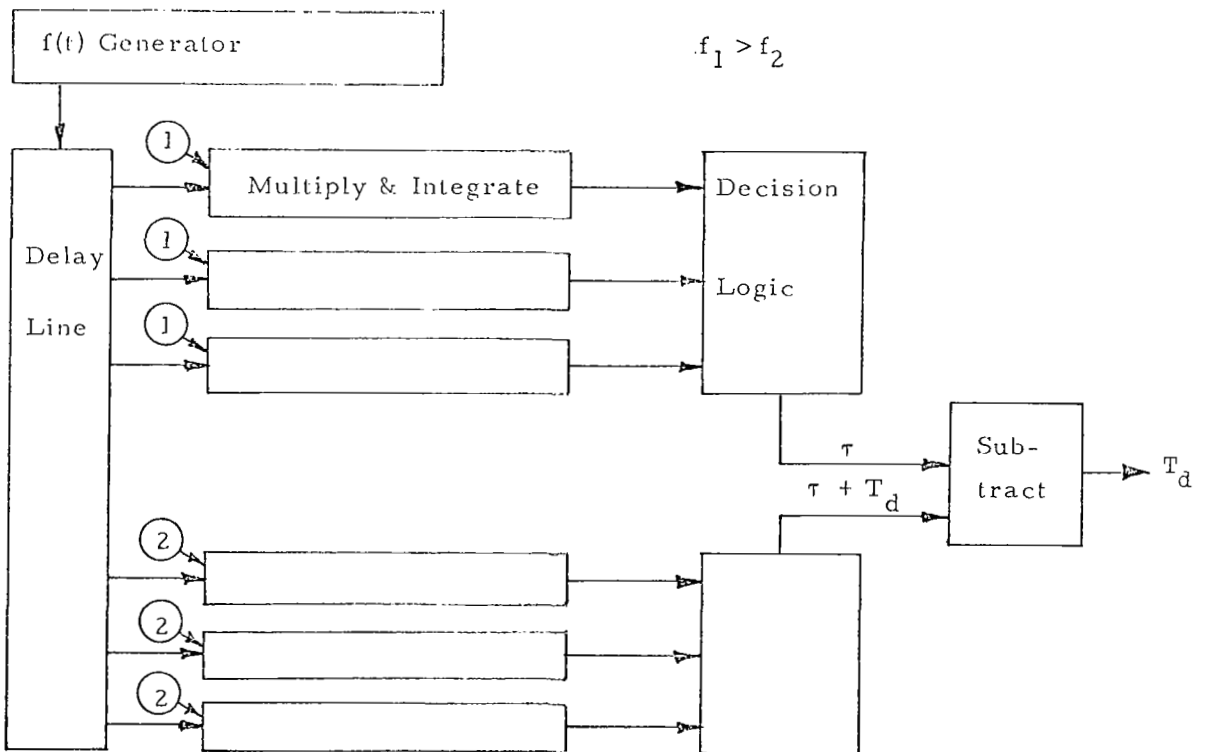
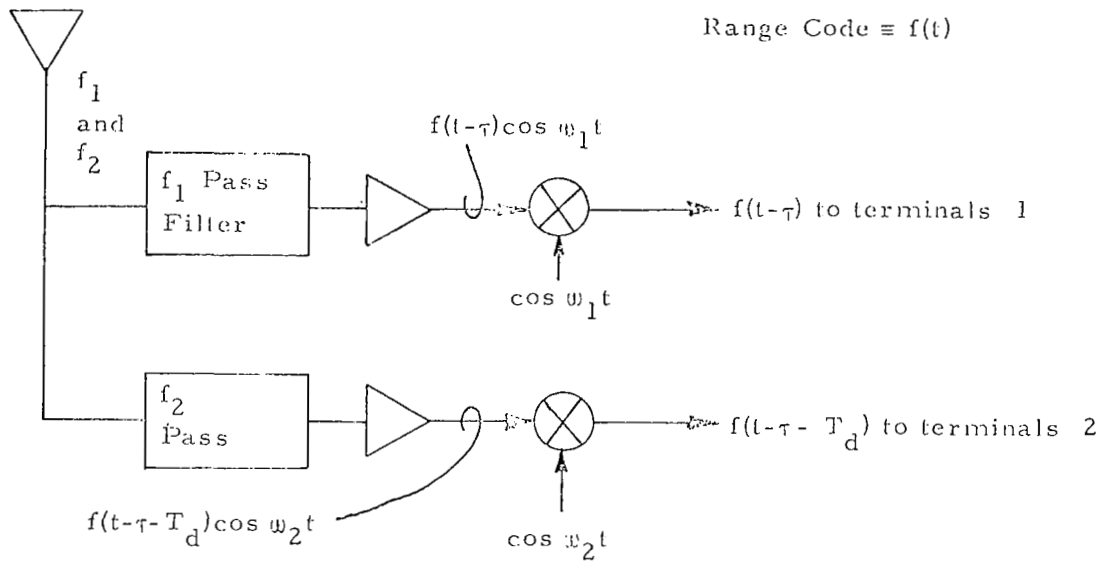


Figure 27 Range Code Receiver

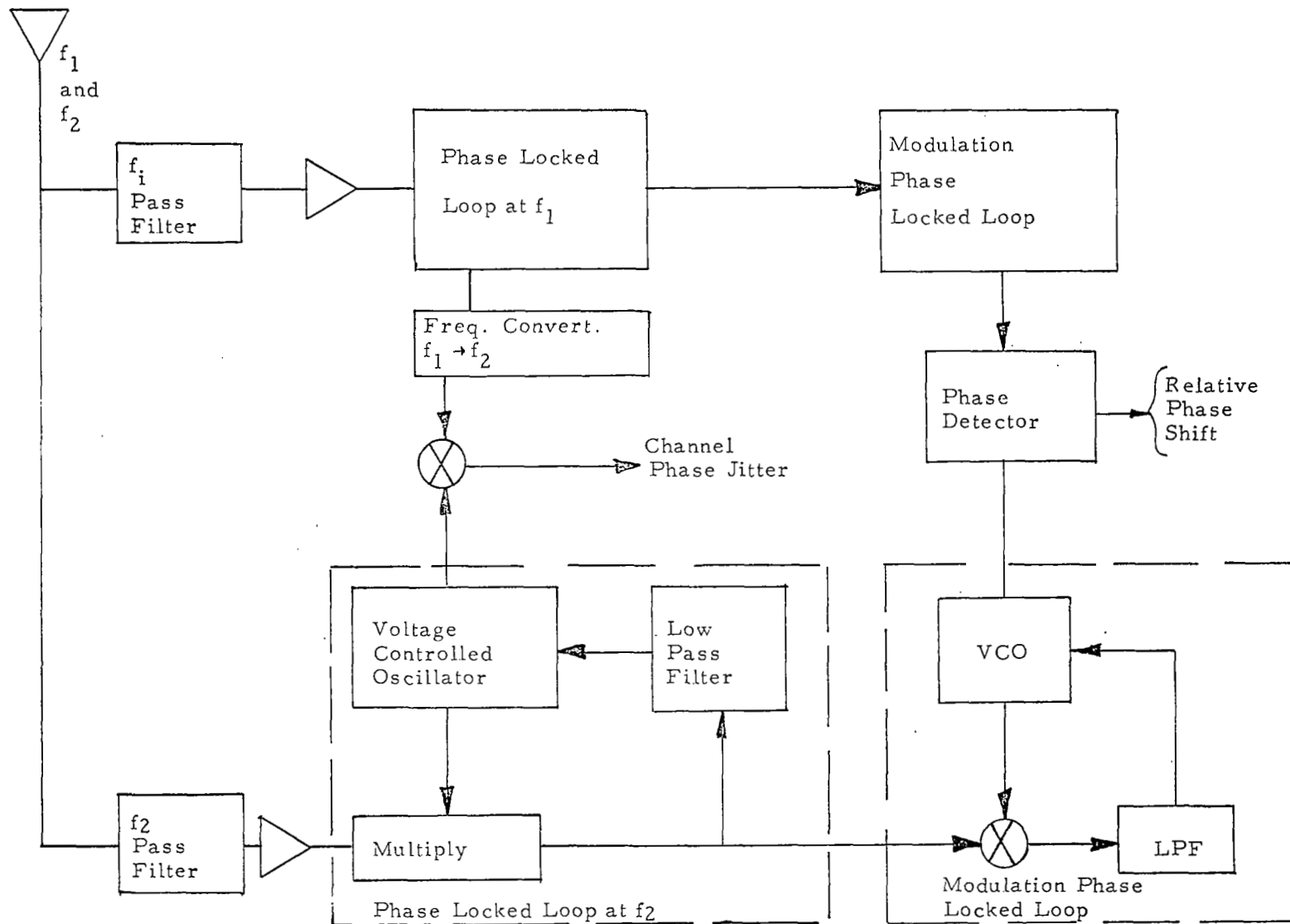


Figure 28 Simplified Diagram of Receiver Used in Pioneer VI and VII Experiments

communications will not be successful in the ordinary sense, although Goldstein (see Spacecraft Propagation Experiments section) pulled signals out of noise by Fourier analysis of prolonged samples. The next sections consider the S/N within a bandwidth necessary for the operation of the phase lock loop.

Downlink Analysis

In this section we determine the requirement for received S/N within the phase lock loop bandwidth, and from this we select the most attractive frequencies for the solar probe experiment. The S/N is based upon existing antenna facilities. Next a comparison of signal energy efficiency is made between the selected system and the proposed Sunblazer system.

The received signal-to-noise ratio is given by the range equation

$$S/N = \frac{P_t G_t A_e}{4 \pi R^2 k T_e B} \quad (15)$$

where A_e = receiving antenna effective area
 T_e = effective receiver noise temperature
 B = phase lock loop bandwidth
 P_t = radiated power
 G_t = transmitting antenna gain
 R = communications range (see Fig. 29 for values used).
 k = Boltzmann's constant

Starting with A_e each of the parameters in Eq. 15 is defined in the following sections.

Facilities - Receiving Antenna. - During the program a review of all radio astronomy observatories was made. Table V shows a partial list of the observatories reviewed and contains the more important ones. Note that all antennas listed are steerable over a hemisphere. The very large non-steerable antennas such as the 1000 ft. diameter antenna at Arecibo, Puerto Rico are eliminated from consideration because of limited daily tracking time. As discussed in our review of current knowledge, solar events occur fast enough to demand a maximum amount of tracking, continuous if possible.

Our review shows that many observatories have 85' diameter parabolic reflector antennas. This antenna seems to be the "work horse" in the fields of space communications and observation. Its frequency range extends easily to X-band with an efficiency of 60% being maintained (except in the worst weather). Designing an experiment around this antenna will greatly reduce problems of site selection and scheduling.

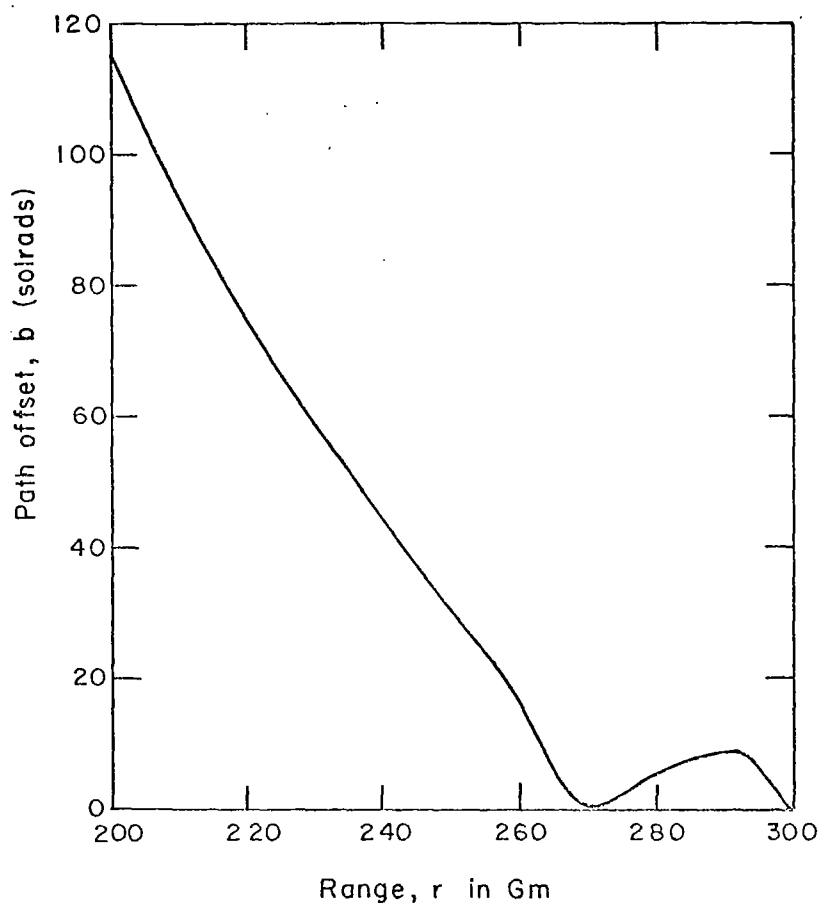


Figure 29 Range and Path Offset Relationship for a Typical Sunblazer Orbit

Table I

| Observatory | Antenna Location | Type Dimensions | Receiving Freq. (Mhz) | Transmitting Freq. / Power | Comments |
|---|--------------------------|-------------------------|---|---|--------------------------|
| 1. JPL | Goldstone Calif. | Parabolic 85'/30'/210' | 2115 2295 2388 8400 | 2115/400KW 2388/100KW 8400/20KW | X Band Telemetry by 1975 |
| 2. MIT Lincoln Lab | Millstone Westford Mass. | Parabolic 84' | 1295 400 150 | 1295/5MW Peak /150KW Ave | |
| 3. MIT Lincoln Lab | Haystack Westford Mass. | Parabolic 120' | L Band 8000 15,500 16,800 | 8000/400KW Ave | Planetary Radar |
| 4. Evans Signal Lab | Belmar New Jersey | Parabolic 85' | 1420 | | |
| 5. Harvard College Observatory | Fort Davis Texas | Parabolic 85' | 200 950 5000 10-580 Sweep | | |
| 6. National Radio Astronomy Observatory | Green Bank W. Va. | Parabolic 85'/140'/300' | 138/234/256 405/611/750 1420/1660- 1720 2695/5000 8500/15000 | | |
| 7. Owens Valley Radio Ob. | Big Pine Calif. | Parabolic 90'/130' | 1400/2800 5000/10,000 | | |
| 8. Stanford | Frazerburg Scotland | Parabolic 149' | 400 800 | | |

Table I (Continued)

| Observatory | Antenna Location | Type Dimensions | Receiving Freq. (Mhz) | Transmitting Freq. / Power | Comments |
|---|-------------------|----------------------------|-----------------------|----------------------------|-------------|
| 9. Stanford | Palo Alto Calif. | Parabolic 150' | 50 425 | 50/250KW 425/30KW | |
| 10. Univ. of Calif. Radio Astronomy Lab | Hat Creek Calif. | Parabolic 85' | 300 1500 10,000 | | |
| 11. University of Michigan | Ann Arbor Mich. | Parabolic 85' | 8000/8700 16,500 | | |
| 12. CSIRO | Parkes Australia | Parabolic 210' | 600 to 10,000 | | |
| <u>Interferometers</u> | | | | | |
| 1. Owens Valley Radio Ob. | Big Pine Calif. | See #7 | | | |
| 2. National Radio Astronomy Observatory | Green Bank W. Va. | 3 Element 85' | 2 x 720 | | |
| 3. Sidney University | Sidney Australia | 32 x 32 19' Paraboloids | 440/1400 | | Mills Cross |
| 4. Stanford | Palo Alto Calif. | 16 x 16 9' Paraboloids | 3280 | | Mills Cross |

Following the 85' diameter antenna we find a number of steerable antennas ranging from 120' to 150' in diameter. These were individually designed since their useful frequency range varies. For example the frequency range of the 120' diameter antenna used by Lincoln Laboratory at Haystack Hill extends to X-band while the Stanford 150' diameter antenna extends to about S-band. For purposes of analysis 150' diameter is selected as a candidate antenna.

The largest antenna which is considered useful for the experiment is the 210' diameter antenna at Goldstone, California. This antenna is usable to X-band and is steerable over a hemisphere. At present the 210' Goldstone antenna is the only one of its kind and is tightly scheduled for data retrieval of presently orbiting Pioneer and Mariner Spacecraft. While the 210' would be ideal, scheduling problems are certain to complicate the solar probe experiment.

While there are many radio astronomy observatories in operation we find that the antenna sizes are limited. 85', 150' and 210' diameter parabolic reflectors steerable over a hemisphere are the prime candidates. There are a few steerable antennas larger than 210' diameter such as the 600 ft. diameter Naval Radio Research Station antenna and an 800 ft. diameter antenna operated by Stanford University. These very large antennas are not intended to be used beyond VHF and scheduling will be a problem since they are intended for special purposes. We therefore confine the propagation link analysis to the 85', 150' and 210' antennas. Of the three the 85' antenna is the prime candidate because of the large number in operation.

Noise Temperature. - There are three sources of noise, solar, galactic and receiver noise. The noise conditions are different for downlink as compared to uplink. As shown in Fig. 30 for a downlink the noise temperature is a function of the propagation path position with respect to the Sun. As the propagation path approaches the Sun, the noise temperature at the receiver will increase because the receiving antenna "sees" the Sun first through its sidelobes and then in its main beam.

In the uplink the noise temperature is independent of spacecraft position. The spacecraft will have a broad beam antenna which will always see the Sun. Noise temperature therefore, will be constant with respect to spacecraft position.

Solar Noise. - Figure 31 shows the spectral density of solar radio noise flux on Earth versus frequency (Ref. 36). For a quiet Sun the flux density increases rapidly with frequency whereas the flux density of a disturbed Sun (max.) is within one order of magnitude over the 30 to 10,000 MHz frequency range shown. Note also 3 to 4 orders of magnitude between quiet and disturbed Sun at the lower frequencies.

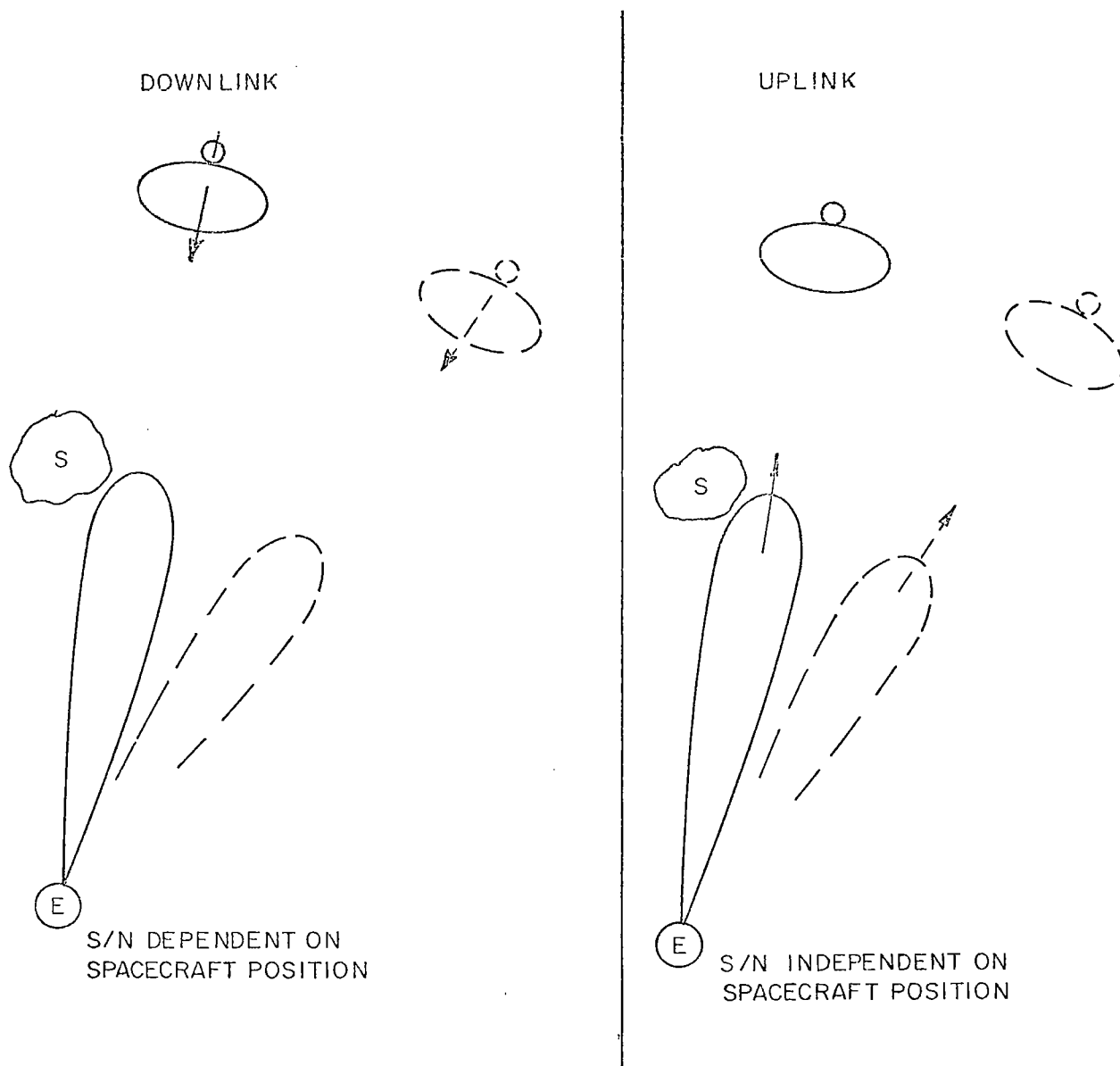


Figure 30 Noise conditions

In determining solar temperature we have elected to use an intermediate value of flux density as shown in dashed lines in Fig.31 . The solar temperature for an antenna which does not resolve the Sun is simply determined as follows:

$$kT_A = P_D A_e(\theta, \phi) \quad (16)$$

where T_A = solar noise antenna temperature
 k = Boltzmann's constant (1.38×10^{-23} J/°K)
 P_D = solar flux density on Earth (Fig.31)
 $A_e(\theta, \phi)$ = effective area of the receiving antenna

Effective area and antenna gain are related by:

$$A_e(\theta, \phi) = \frac{\lambda^2}{4\pi} G(\theta, \phi) \quad (17)$$

where λ = wavelength
 $G(\theta, \phi)$ = antenna gain

Substituting Eq. (17) into Eq.(16) yields

$$T_A = \frac{P_D}{k} \frac{\lambda^2}{4\pi} G(\theta, \phi) \quad (18)$$

or

$$T_A = \frac{P_D}{k} \frac{A_{e0}}{G_0} G(\theta, \phi) \quad (19)$$

where A_{e0} = effective area at $\theta = \phi = 0^\circ$
 G_0 = antenna gain at $\theta = \phi = 0^\circ$

The effective area is related to the physical area of the antenna through the efficiency η . Equation (19) therefore becomes

$$T_A = \frac{P_D}{k} \eta A_P \frac{G(\theta, \phi)}{G_0} \quad (20)$$

where A_P = physical area of the antenna

One last step is required before T_A can be obtained and that is to determine the antenna gain relation $\frac{G(\theta, \phi)}{G_0}$.

Figure 32 shows a smoothed version of the far field radiation pattern of a uniformly illuminated circular aperture. This bell-shaped curve is used in all calculations of T_A to eliminate the complicated effect of the lobe structure. In the abscissa D_e is effective aperture diameter $\sqrt{\lambda}$ D_P . The lower curve represents an ideal circular aperture, and the

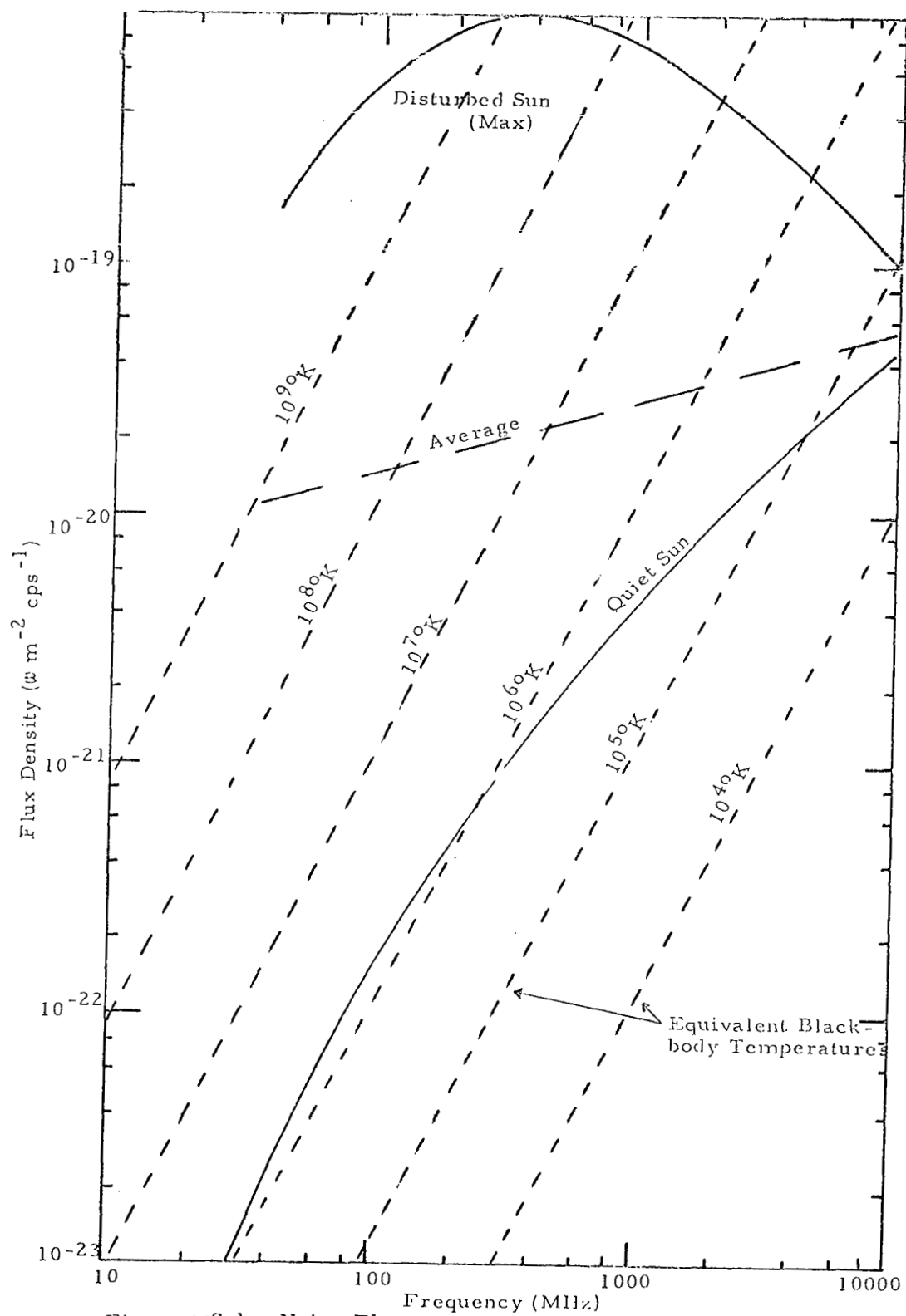


Figure 31 Solar Noise Flux

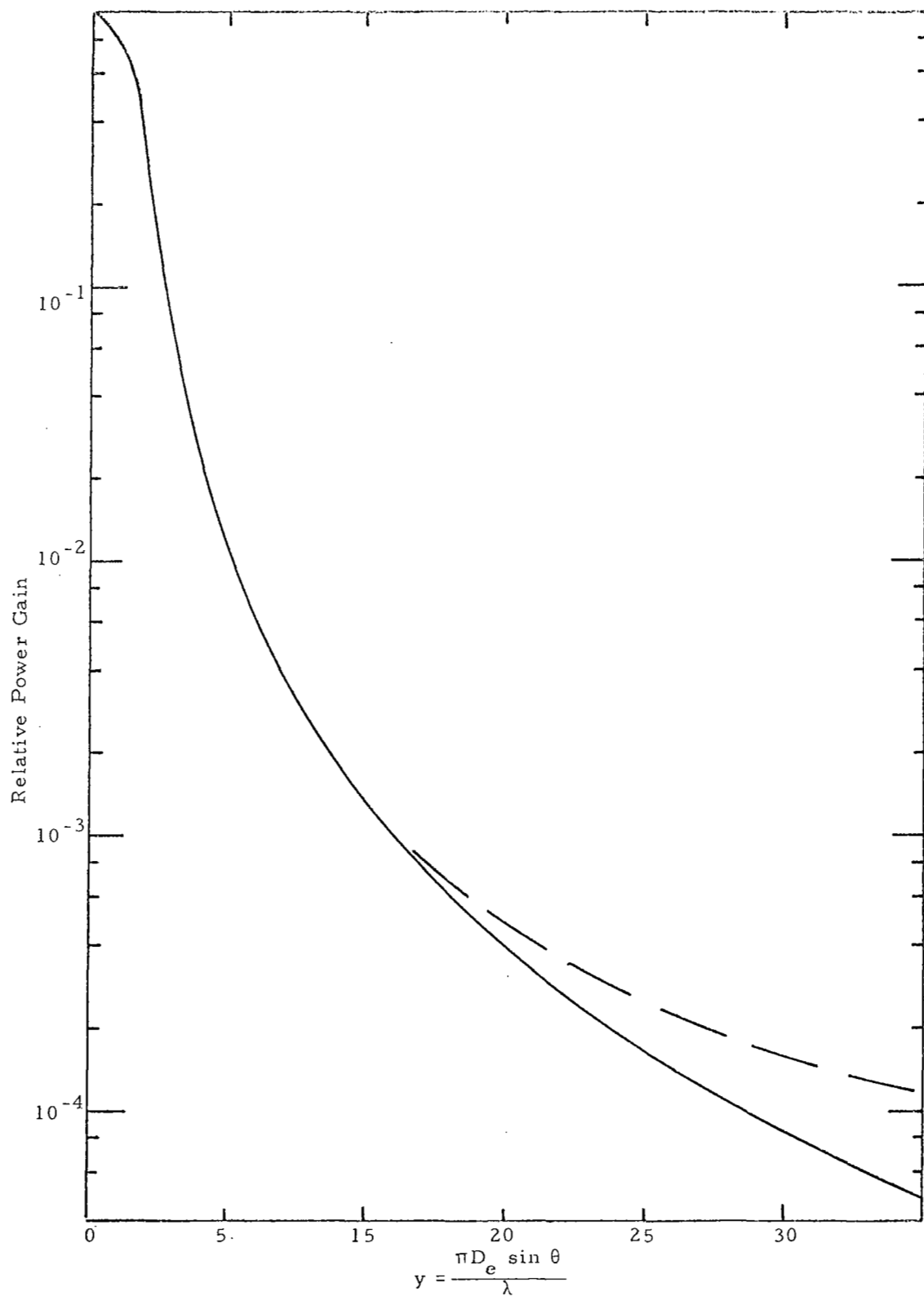


Figure 32 Antenna Pattern of a Uniformly Illuminated Circular Aperture

upper one a practical aperture in which auxiliary structures such as quadripods create extra side lobe structure. The practical curve is a smoothed version of the measured pattern of the 210' in two different planes.

If the solar flux density is interpreted in terms of an equivalent black-body temperature, T_s as in Fig. 31, the antenna temperature T_A can be expressed as follows. If the antenna does not resolve the sun, its beamwidth Ω_A is larger than the angle, Ω_s subtended by the sun and we have

$$T_A = \Omega_s T_s \frac{G(\theta, \phi)}{G_o}, \quad \Omega_A \geq \Omega_s$$

If the antenna is capable of resolving the Sun, the antenna temperature is

$$T_A = T_s \frac{G(\theta, \phi)}{G_o}, \quad \Omega_A \leq \Omega_s$$

Figures 33, 34 and 35 show the solar noise temperature versus frequency for the 85', 150', and 210' antennas. Each figure has a family of curves showing the effect of path offset (measured in solar radii) on solar noise temperature. Figure 36 summarizes Fig. 33 through 35 for the frequencies of primary interest.

Figures 33 through 35 show clearly how solar noise decreases as frequency increases for a fixed antenna diameter. For a given antenna and a fixed offset angle as frequency increases from 30 MHz solar noise temperature initially increases. This is because the solar flux density increases with frequency. As frequency increases, however, the antenna beamwidth decreases, hence the sharp roll off of solar temperature as this parameter takes effect. Figures 33 through 35 show clearly the penalty incurred at low frequencies with existing antennas.

Also shown on Fig. 35 are the solar noise temperatures of the El Campo system. For a simple rough estimate, we treated the square El Campo array as if it were a circular aperture of the same area. The situation is summarized in Fig. 36 for S-band and El Campo antennas as a function of path offset.

Galactic Noise. - Galactic noise is defined as cosmic noise from all sources in our galaxy except the Sun. Our solar system belongs to a galaxy which has a pancake spiral shape. A receiving antenna pointed toward the galactic center will record a very high noise temperature whereas the same antenna pointed in the direction of the galactic pole will see fewer sources and record a much lower noise temperature.

Figure 37 shows galactic noise temperature as a function of frequency. For the purpose of this analysis we have selected a galactic noise temperature lying between the galactic center and pole noise temperature.

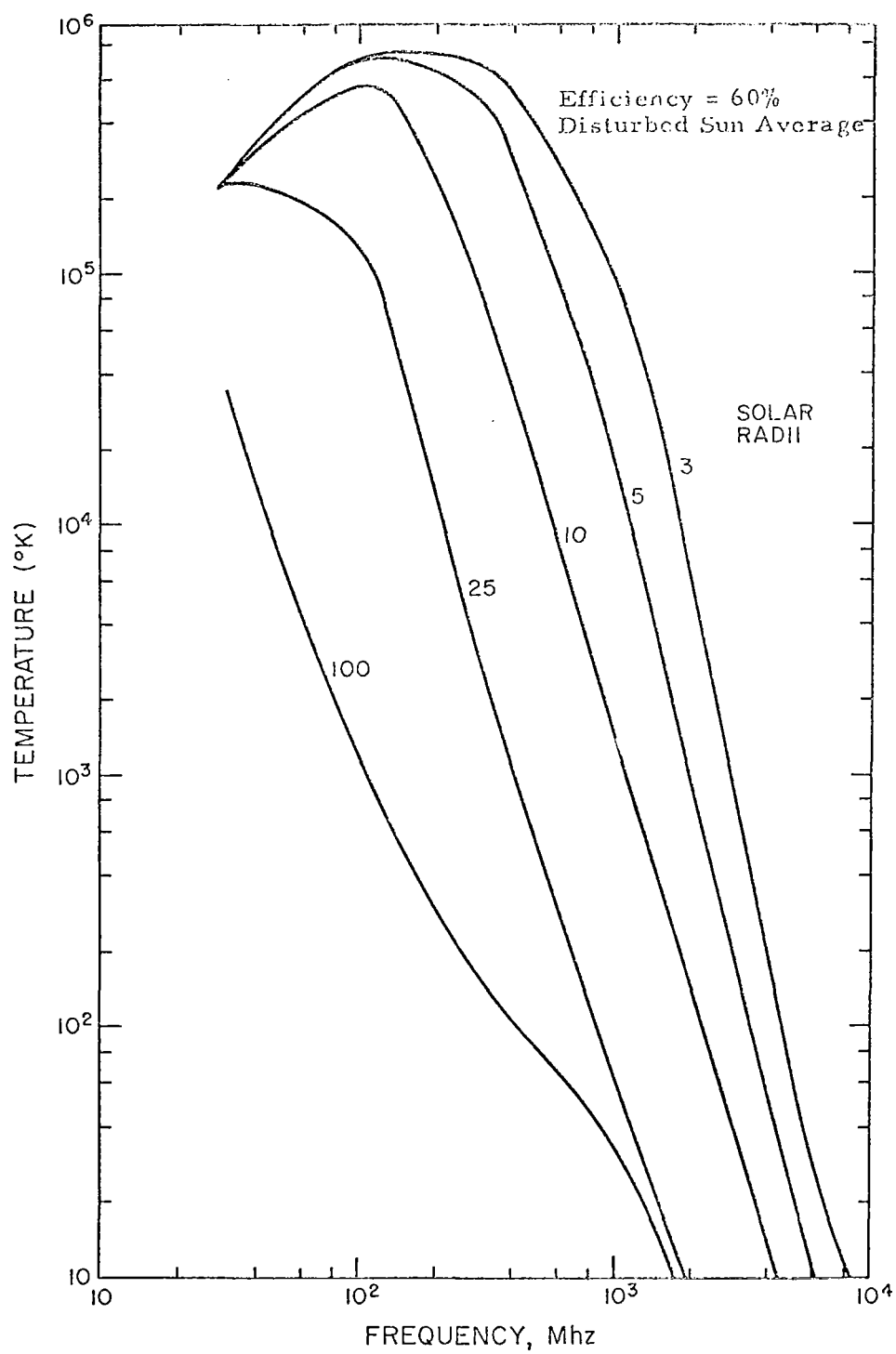


Figure 33 Sun noise temperature - 85' diameter antenna

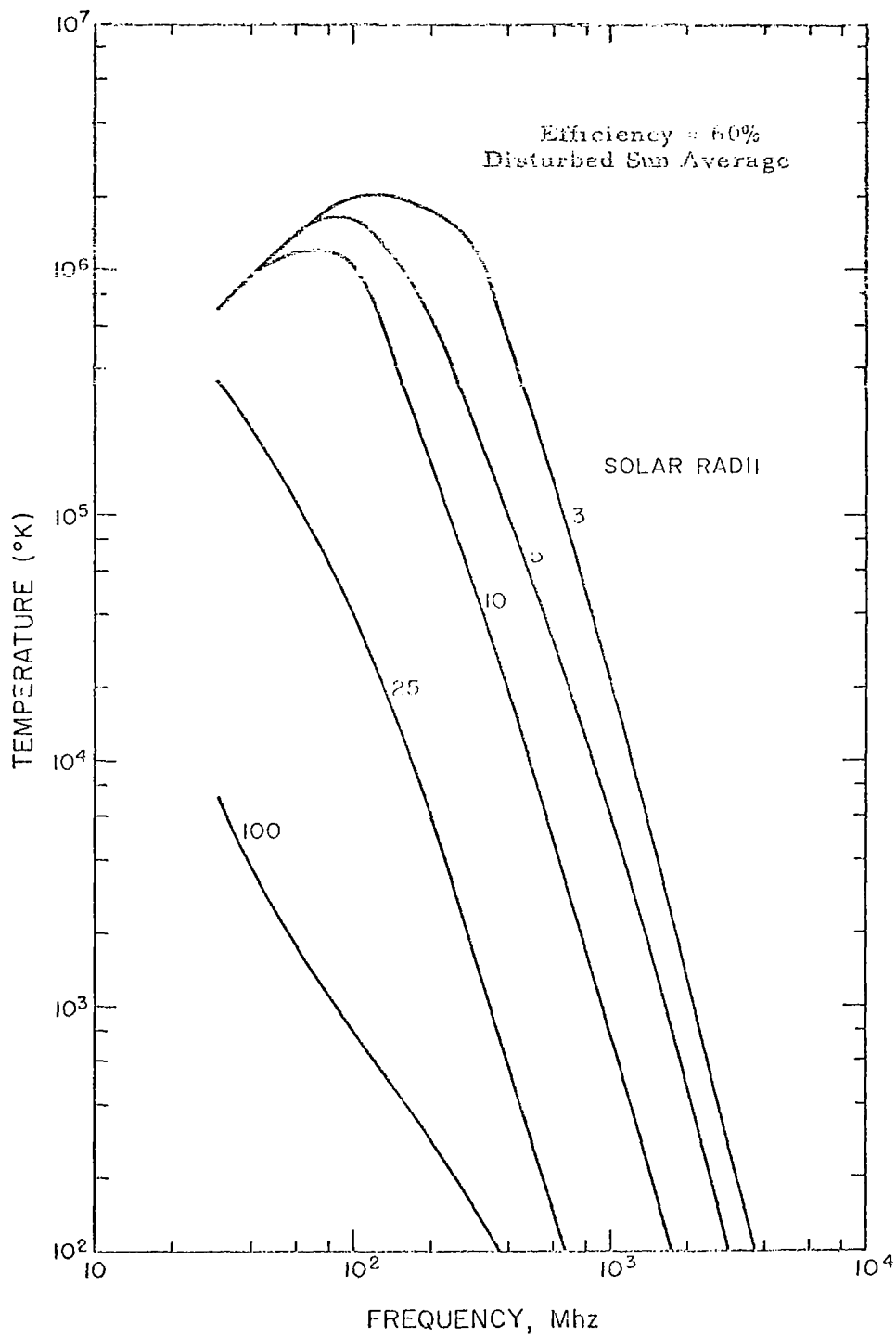


Figure 34 Sun noise temperature - 150' diameter antenna

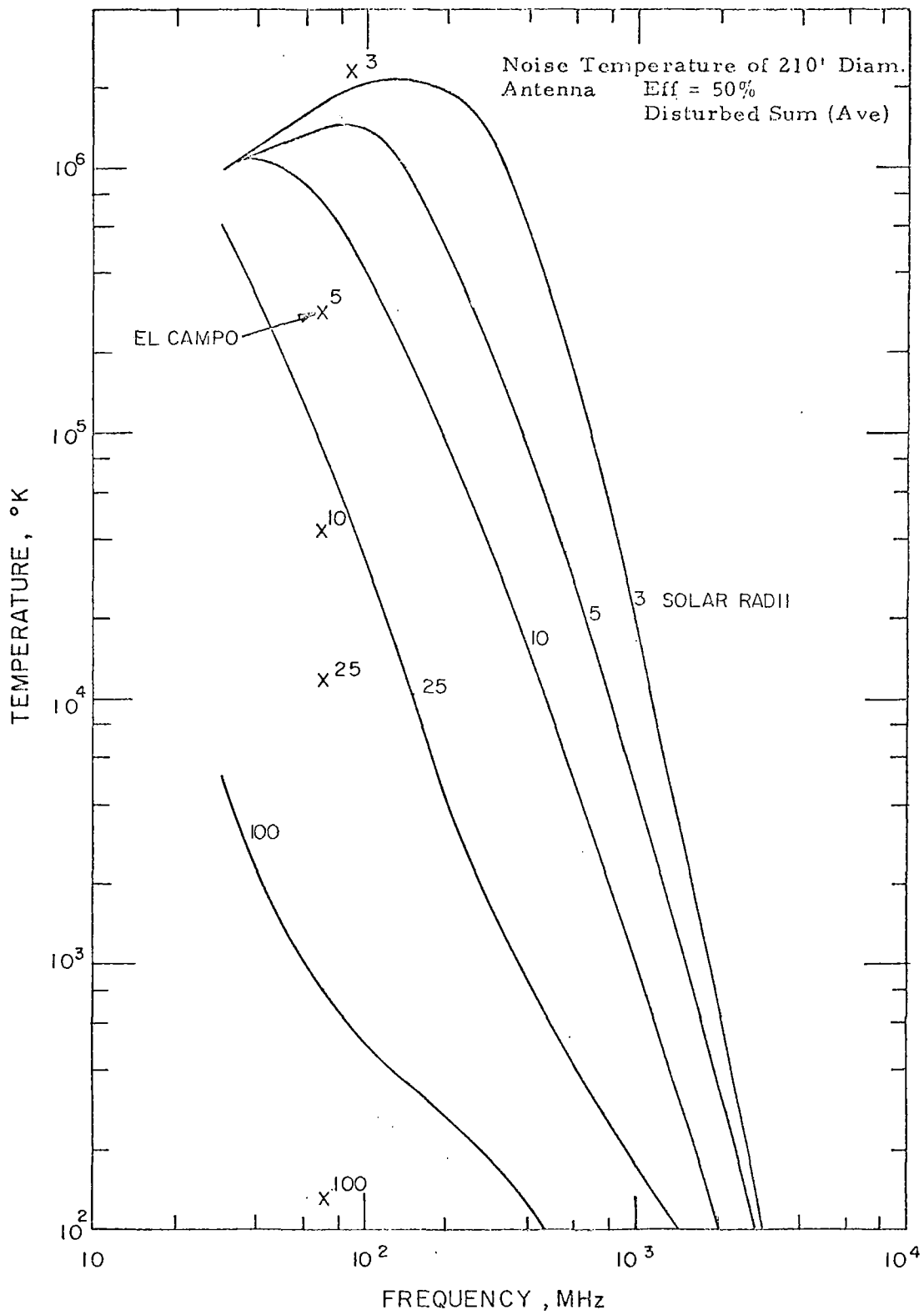


Figure 35

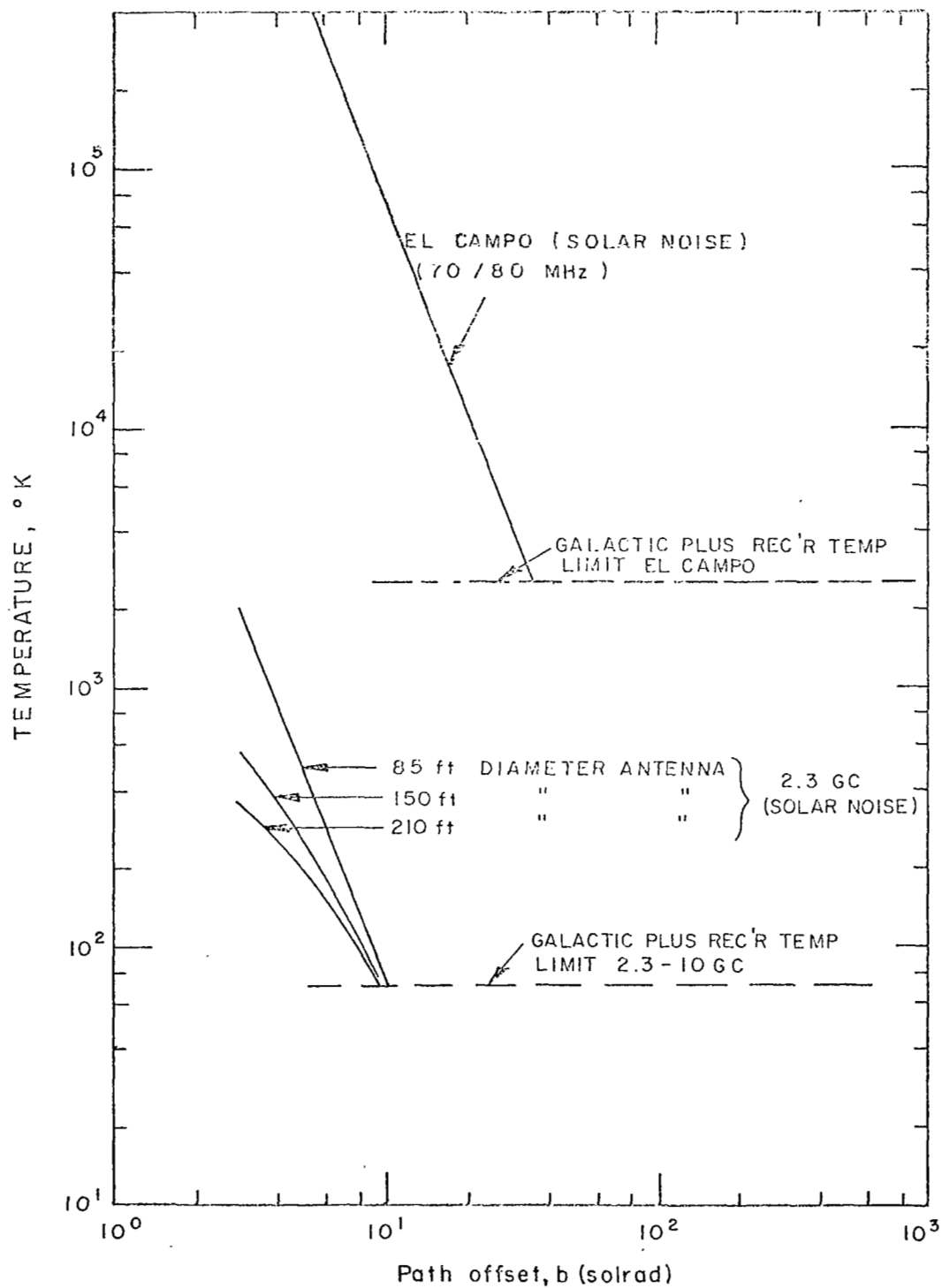


Figure 36 Antenna noise temperature summary as a function of path offset

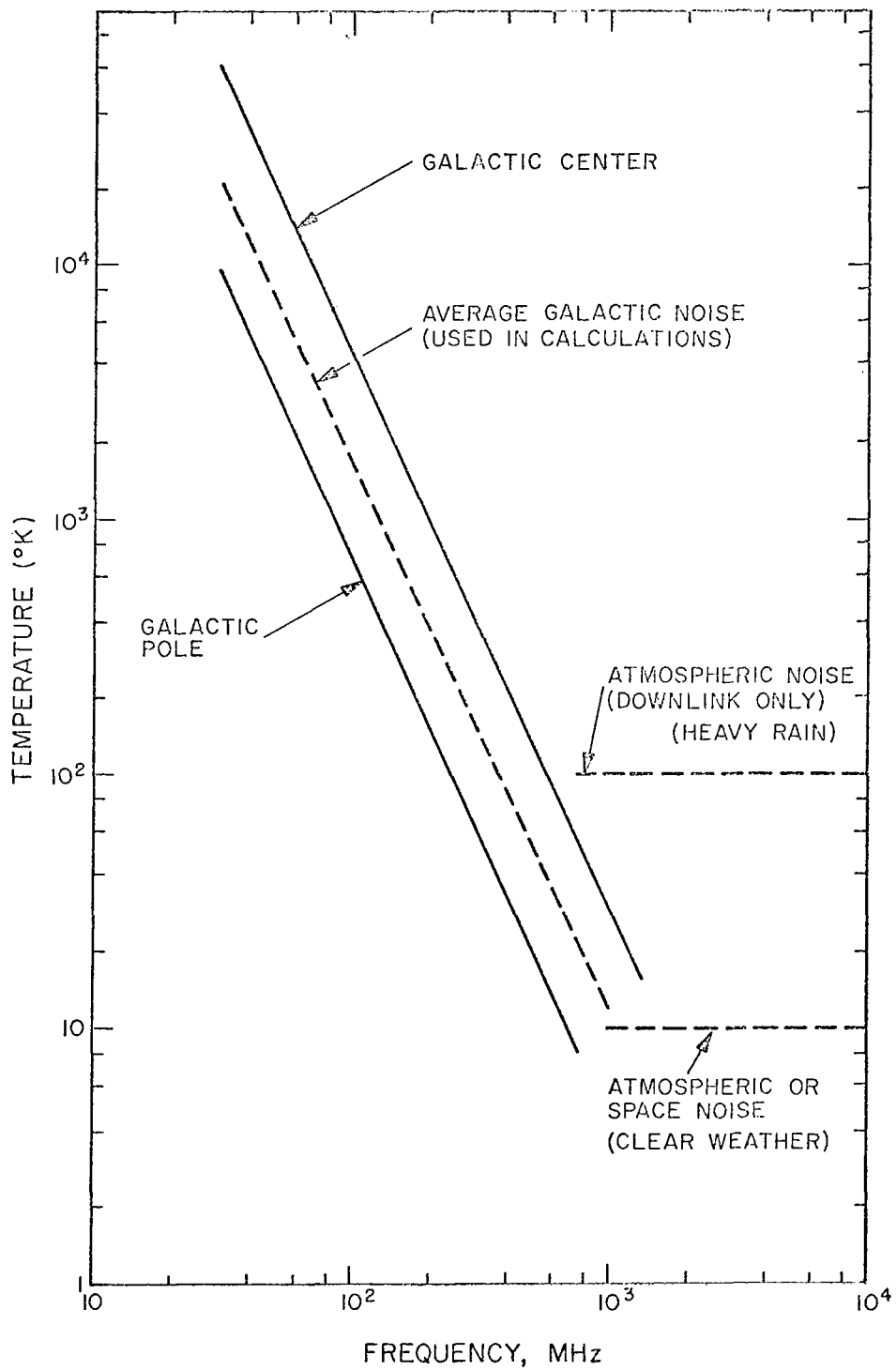


Figure 37 Galactic and atmospheric noise temperature

Receiver Noise. - The downlink receiver is not weight or volume constrained as is an uplink receiver. Also in order to insure maximum S/N a low noise receiver such as a maser or cooled parametric amplifier will be used. We have assumed a receiver noise temperature of 100°K across the frequency band of interest (30 MHz to 10,000 MHz). Figure 38 justifies this noise temperature which in the case of the maser is conservative as 25 to 50°K has been attained in the NASA deep space net.

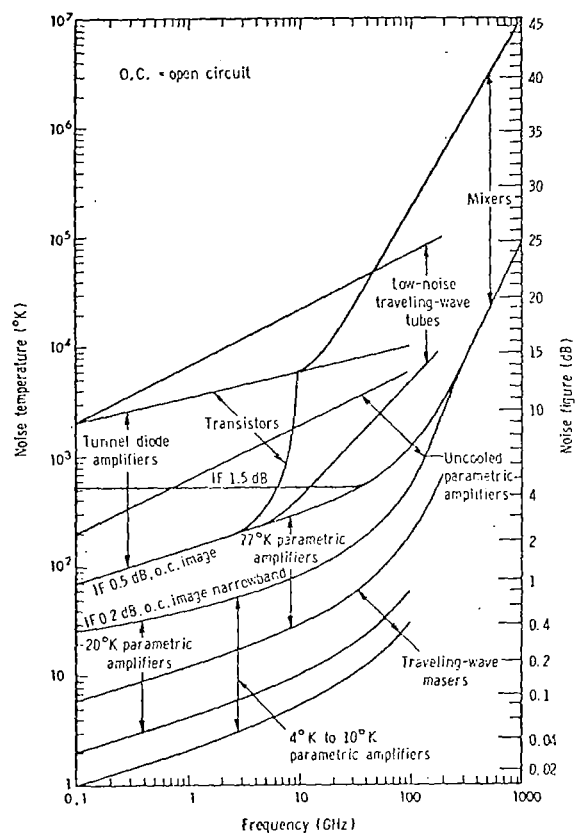


Fig.38 — Comparison of noise-figure and frequency ranges of low-noise devices.

Spacecraft Radiated Power. -Average power radiated by the spacecraft is limited by the primary source of power. On long-duration flights such as the solar probe mission, silicon solar cells undoubtedly must be used. In the past the cells have been mounted on flat panels or around the body of the spacecraft. In either configuration an electrical power output of 8 to 10 w/ft² of panel area can be obtained when: (1) vertical incidence to solar radiation is maintained and (2) the spacecraft is about 1 a.u. from the Sun or closer.

The efficiency of the transmitter varies with frequency and the magnitude of radiated power. For example the efficiency of a solid state transmitter below about 300 MHz is about 50% for a power output 5 watts. This will fall off at higher frequency. An S-band efficiency of about 20% can be expected using tube power amplifiers. (These efficiencies do not include power conditioning equipment.)

Assuming transmitter efficiency of 20% and 8 - 10 w/ft² power output from the silicon solar panels we find that a reasonable average radiated power is 5 watts. Also improvements in the state-of-the-art will increase the efficiency of future systems. We use 5 watts radiated power in our downlink range equation.

Spacecraft Antenna Gain. -At frequencies below about 1 GHz aperture type antennas are not practical. At these frequencies some type of stub or whip antenna will be used. The gain of a stub antenna is 1.5, which we have assumed from 30 MHz to 100 MHz. At frequencies above 1000 MHz we assume a constant gain of 20 db. Antenna attitude control is not required with a 20 db antenna for path offsets less than 38 solrad (10°), since the width of a 20 db beam is 20°. We would prefer a 10 db antenna for a 63° beam, but a 10 db antenna gives a completely inadequate S/N.

If active antenna pointing were provided, the spacecraft antenna gain could be increased significantly. The aperture diameter of a 20 db gain antenna is about four wavelengths. This is not very large, especially at the higher microwave frequencies; for X-band it could even be increased further without becoming unwieldy.

Downlink Signal-to-Noise Ratio. -All parameters in the range equation have been determined in the preceding subsections. Figures 39 and 40 show the results for the 85' and 210' antennas. From these graphs two facts are immediately evident: (1) microwave frequencies are necessary for the downlink experiment with existing antennas and (2) a system continuously radiating at a 5 watt power level does not provide much S/N margin, especially for the 85' antenna, the one more likely available. The 5 watts here are assumed to be continuous for maintenance of phase lock; that is, the peak power is equal to the average power. The receiver bandwidth is taken as the channel jitter bandwidth caused by the solar corona. This cannot be reduced substantially without the phase lock loop occasionally losing lock and jumping cycles. The S/N shown in

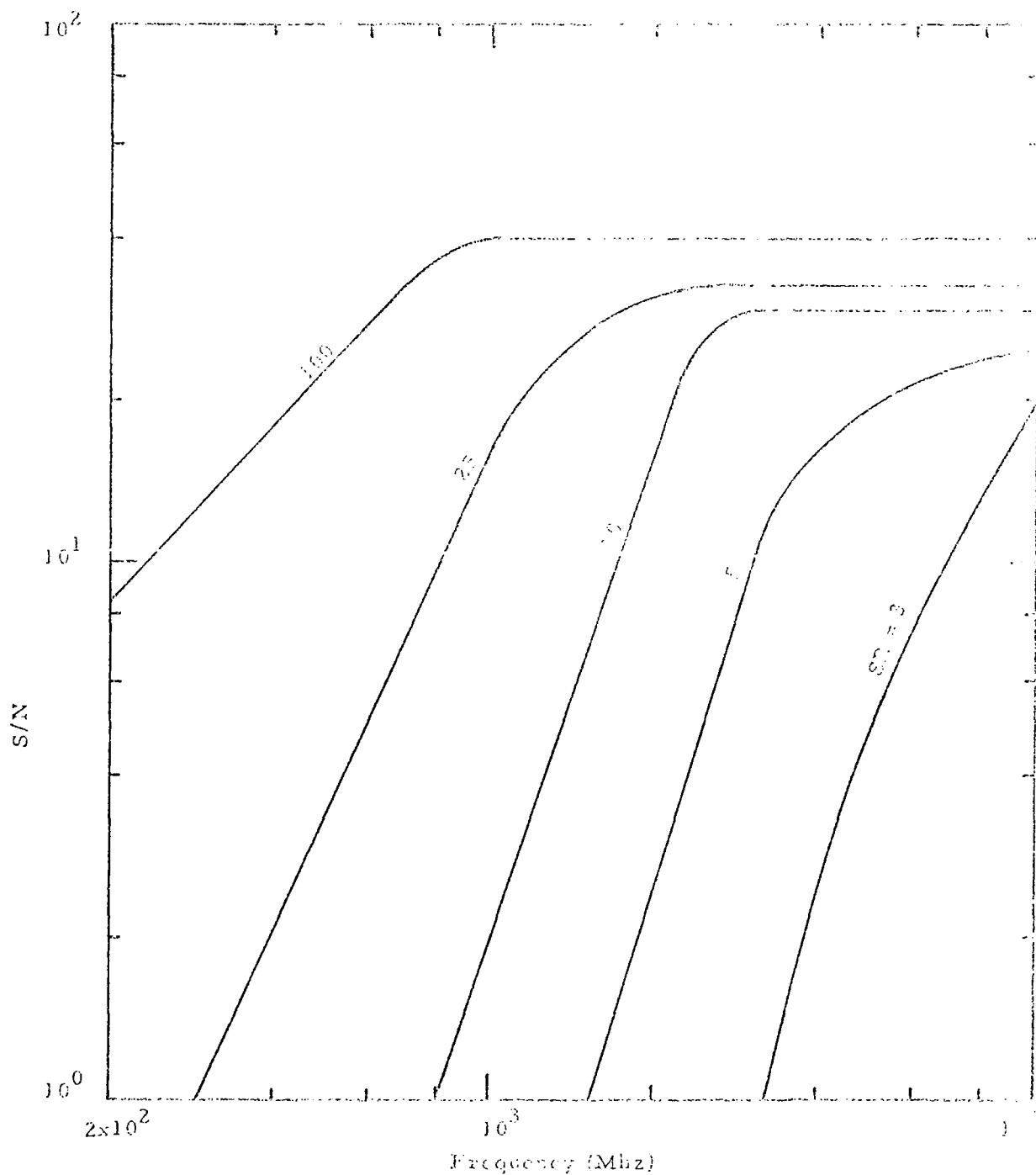


Figure 39 Phase Lock Loop Signal-to-Noise Ratio vs. Frequency for a 5 watt Downlink to a Standard 85' Paraboloid Antenna

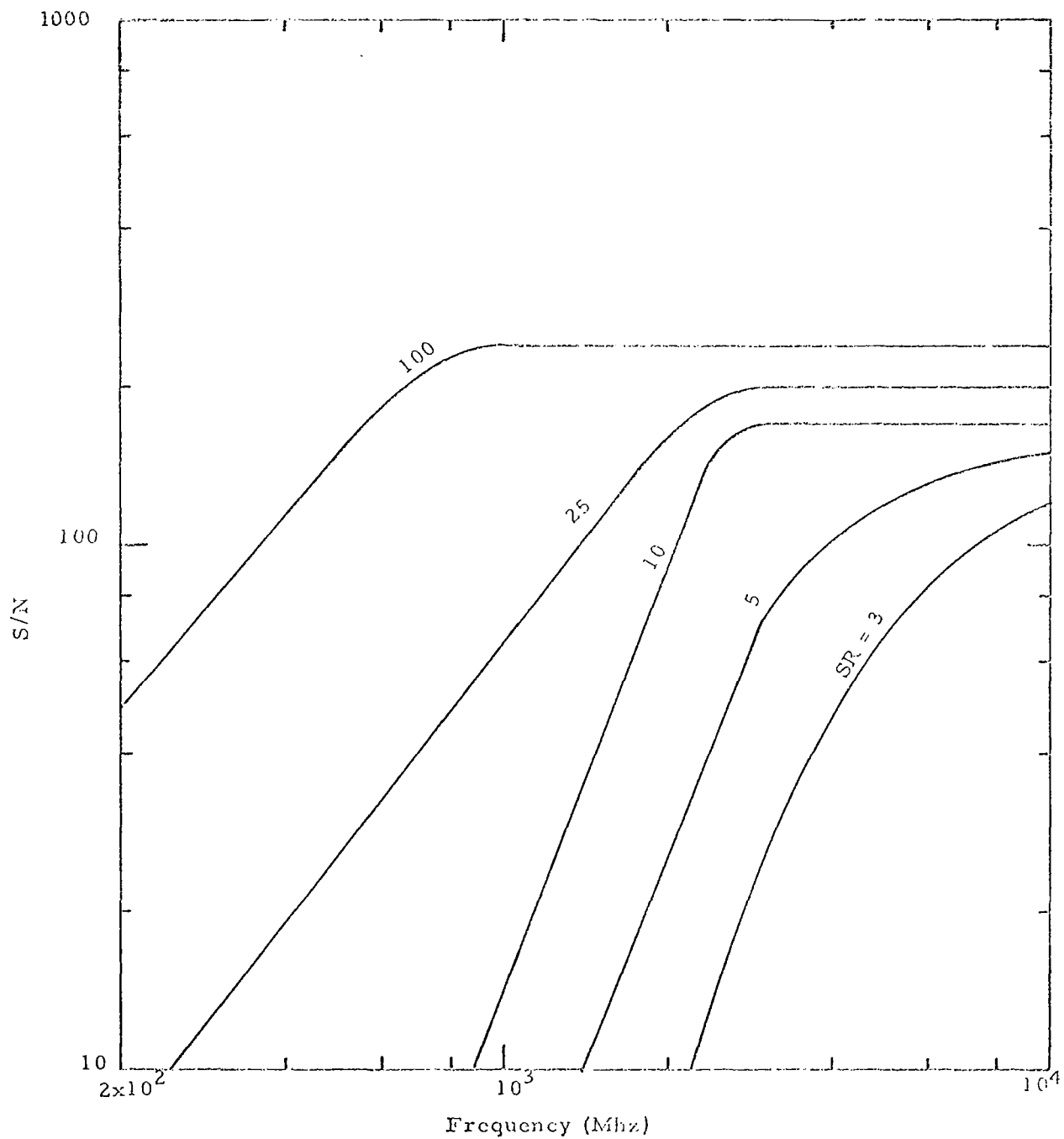


Figure 40 Phase Lock Loop S/N vs. Frequency for 5 watt Downlink to 210' Antenna

Fig. 39 and 40 are therefore the highest attainable with the assumed parameters.

The channel phase-jitter bandwidth was discussed in the Radio Measurements section and plotted in Fig. 22 . To obtain Figs. 39 and 40 we used an average of the Pioneer VI and Mariner IV observed bandwidths, except scaled as f^{-1} to take frequency dependence into account. The bandwidth decreases with path offset as the corona becomes rarified and more homogeneous. Our calculations take the channel bandwidth

$$B = \text{Max of } \begin{cases} \text{Phase jitter B,} \\ 5 \text{ Hz,} \end{cases}$$

since other limitations such as oscillator stability begin to appear at very narrow bandwidths.

The S/N of Fig. 39 and 40 are marginal as given for a CW system. Figure 41 shows the alternatives for salvaging downlink propagation. If the transmitted peak power can be increased without increasing signal bandwidth, a S/N increase could be obtained. The spacecraft however has a fixed average power which means that peak power can be increased only at the expense of duty cycle. It is perfectly feasible to employ a pulsed signal (modulation is still required within the pulse) however it changes the receiving terminal considerably and reduces the data rate. A coherent receiver is still required, but with a pulsed signal a phase-lock-loop cannot maintain lock between pulses. Received raw data at IF frequencies (≈ 5 MHz) must therefore be stored on magnetic tape and a computer used to reduce the data or simulate the coherent receiver. The computer in effect searches for phase lock on each received pulse by playing the tape many times and searching for a locked condition by varying frequency and phase. The data storage requirement also has practical implications. Present state of the art tape recorders have an upper data storage rate limit of 10 MHz. This means that the transmission signal bandwidth is limited by the receiving terminal storage capability, which reduces measurement accuracy below the maximum theoretical value. New techniques of optical data storage and processing may relieve this limitation in the next 10 years.

If a downlink experiment is selected, we recommend a lower carrier frequency of 2.3 GHz and an upper carrier frequency at X-band (10 GHz) in the pulsed alternative, 2295 MHz is a downlink frequency for the NASA Deep Space Net, and much equipment is already in operation. Also in the near future (1975) a telemetry link at X-band will be in operation. A downlink experiment at S/X-band would, therefore, be using operational frequencies and equipment, which represents a considerable cost saving. The lower of the two frequencies should be increased to about 6 GHz in a CW phase-locked system.

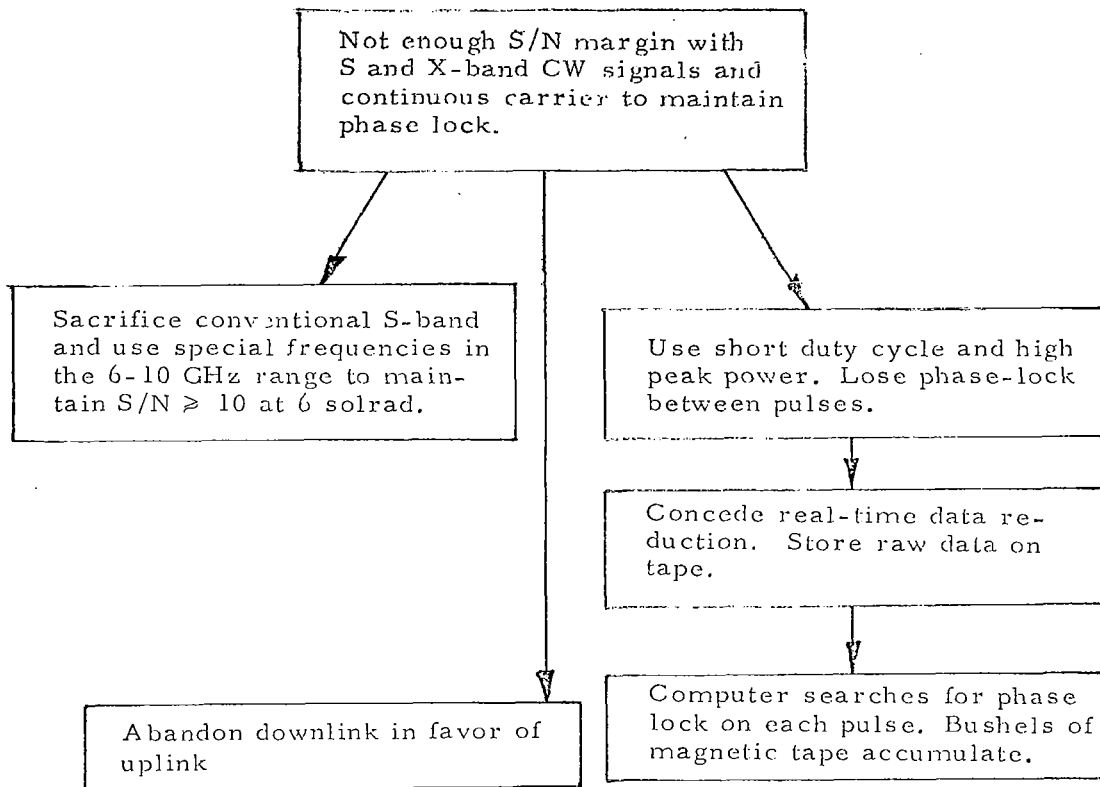


Figure 41 Downlink alternatives

Downlink Energy Efficiency

Theoretical Limit. -The preceding section showed that S-band frequencies and higher are appropriate for a downlink experiment with existing antennas. It is still necessary to determine how accurately solar corona measurements can be made at S/X band and compare this accuracy with the proposed Sunblazer system.

In comparing downlink systems we consider not only the accuracy of the measurement but also the transmitted energy required to make that measurement. The comparison is made for three systems: (1) S/X-band using the 85' antenna, (2) S/X-band using the 210' antenna and (3) 70/80 MHz for the proposed Sunblazer system. The integrated electron density (I) is the parameter used in the comparison.

Assuming that a ranging code is used in all of the downlink cases the rms timing error between autocorrelation peaks is given by:

$$\Delta = \frac{T_B}{\sqrt{2 E/N_o}} \quad (21)$$

where Δ = rms timing error
 E/N_o = received signal to noise energy ratio
 T_B = pulse width

The relative group time delay between frequencies f_l (lower carrier frequency) and f_h (upper carrier frequency) is

$$T_D = \frac{1.35 \times 10^{-7}}{f_l^2} \left(1 - \frac{f_l^2}{f_h^2}\right) I \quad (22)$$

The measurement error therefore is given as

$$\frac{\Delta}{T_D} = \frac{\sqrt{\langle \Delta^2 \rangle}}{I} = \frac{T_B f_l^2}{1.35 \times 10^{-7} \left(1 - \frac{f_l^2}{f_h^2}\right) I \sqrt{2 E/N_o}} \quad (23)$$

E/N_o is obtained from the range equation

$$E/N_o = \frac{E_t G_t A_e}{4 \pi R^2 k T_e} \quad (24)$$

where E_T = transmitted energy per ranging code word
 G_T = transmitter antenna gain
 A_e = effective area of receiving antenna
 T_e = effective noise temperature (solar, galactic, and receiver)
 R = range

Substituting Eq. (24) in the square of Eq. (23) yields

$$\frac{\langle \Delta^2 I \rangle}{I^2} E_T = \left[\frac{4 \pi k R^2}{2 (1.35 \times 10^{-7})^2} \right] \left[\frac{T_B^2 T_e f_1^4}{\left(1 - \frac{f_1}{f_h}\right)^2 I^2 G_T A_e} \right] \quad (25)$$

Equation (25) can be further reduced by eliminating the pulse width T_B . Since accuracy improves as T_B decreases we wish to use the minimum possible T_B . Aside from practical considerations the channel itself will limit minimum T_B , since it is dispersive. The pulse rise time as a function of path offset is derived in Appendix 1. The transmitted pulse width must be larger than the channel limited pulse rise time, and we have set the minimum pulse width equal to twice the rise time. Pulse width is given as:

$$T_B = 2 \frac{(1.38 \times 10^{+7})}{f^{3/2}} \sqrt{\frac{\cos^{-1}\left(\frac{b}{215}\right)}{b}} \quad (26)$$

T_B is shown in Fig. 42. Substituting Eq. (26) into Eq. (25) yields the theoretically best measurement accuracy of 1.

$$\frac{\langle \Delta^2 I \rangle}{I^2} E_T = \left[\frac{4 \pi R^2 k}{2 (1.35 \times 10^{-7})^2} \right] \left[\frac{4 (1.38 \times 10^7)^2 \cos^{-1}\left(\frac{b}{215}\right)}{b} \right] \quad (27)$$

$$\left[\frac{T_e f_1}{\left(1 - \frac{f_1}{f_h}\right)^2 I^2 G_T A_e} \right]$$

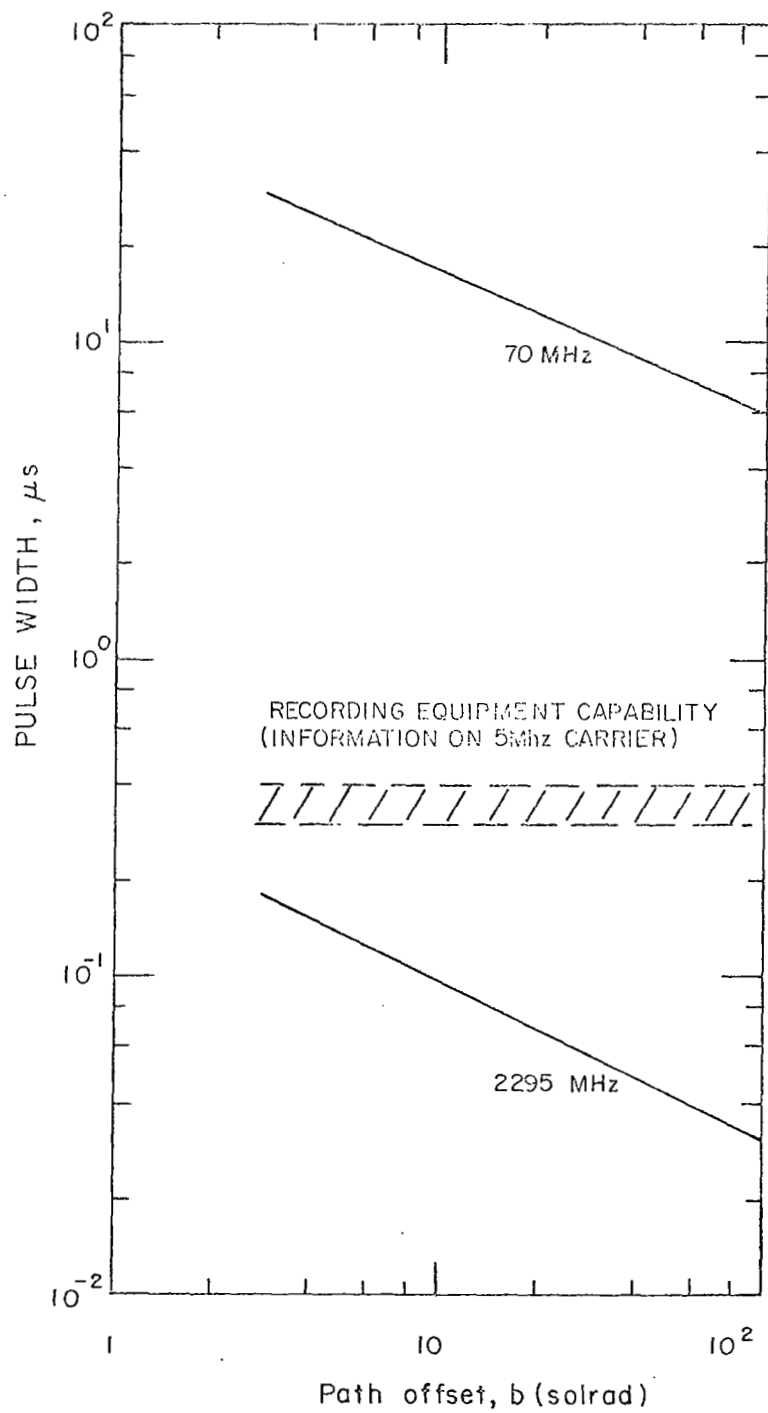


Figure 42. Allowable pulse width for acceptable time dispersion distortion

Equation (27) gives the product of mean square error in the I measurement times the transmitted energy required to make this measurement.

It is apparent that the system with minimum $\frac{\langle \Delta I^2 \rangle}{I^2} E_T$ is most efficient.

Table VI shows the parameters required to determine $\frac{\langle \Delta I^2 \rangle}{I^2} E_T$.

| System Parameter | Sunblazer (El Campo array) | 85' Antenna | 210' Antenna |
|---------------------|----------------------------------|-------------------|--------------------|
| T_e | See Fig. 33, 35, and 37 | | |
| I | See Fig. 26 (App. 2) | | |
| f_l | 70 MHz | 2295 MHz | 2295 MHz |
| f_h | 80 MHz | 10,000 MHz | 10,000 MHz |
| G_t | 1.5 | 100 | 100 |
| A_e | $1.5 \times 10^5 \text{ m}^2$ | 320 m^2 | 1930 m^2 |

Table VI Parameter for Theoretical Systems Comparison

Figure 43 is a plot of Eq. (27) versus path offset, using Table VI. It shows that theoretically the 85' and 210' antenna systems are superior to the Sunblazer system, which is limited by solar noise to operate no closer than 5 solar radii, the region of major interest in the study of the physics of the solar corona. On the other hand, the S/X-band systems using the 85' and 210' antennas function to within 3 solar radii.

Note that Fig. 43 is obtained on a noise basis only and does not account for amplitude scintillation or "deep" fades which may occur as the propagation path nears the Sun. Of course, fading near the Sun is more severe at the lower frequencies because of the greater signal interaction with the plasma. Fading is thus another factor that weighs in favor of high microwave frequencies.

Practical Efficiency Comparison. - Figure 43 is an energy efficiency comparison using the minimum possible pulse width (maximum bandwidth) at all solar radii which the channel can support. In this section a comparison is made on the basis of constant pulse width and tape recording limitations.

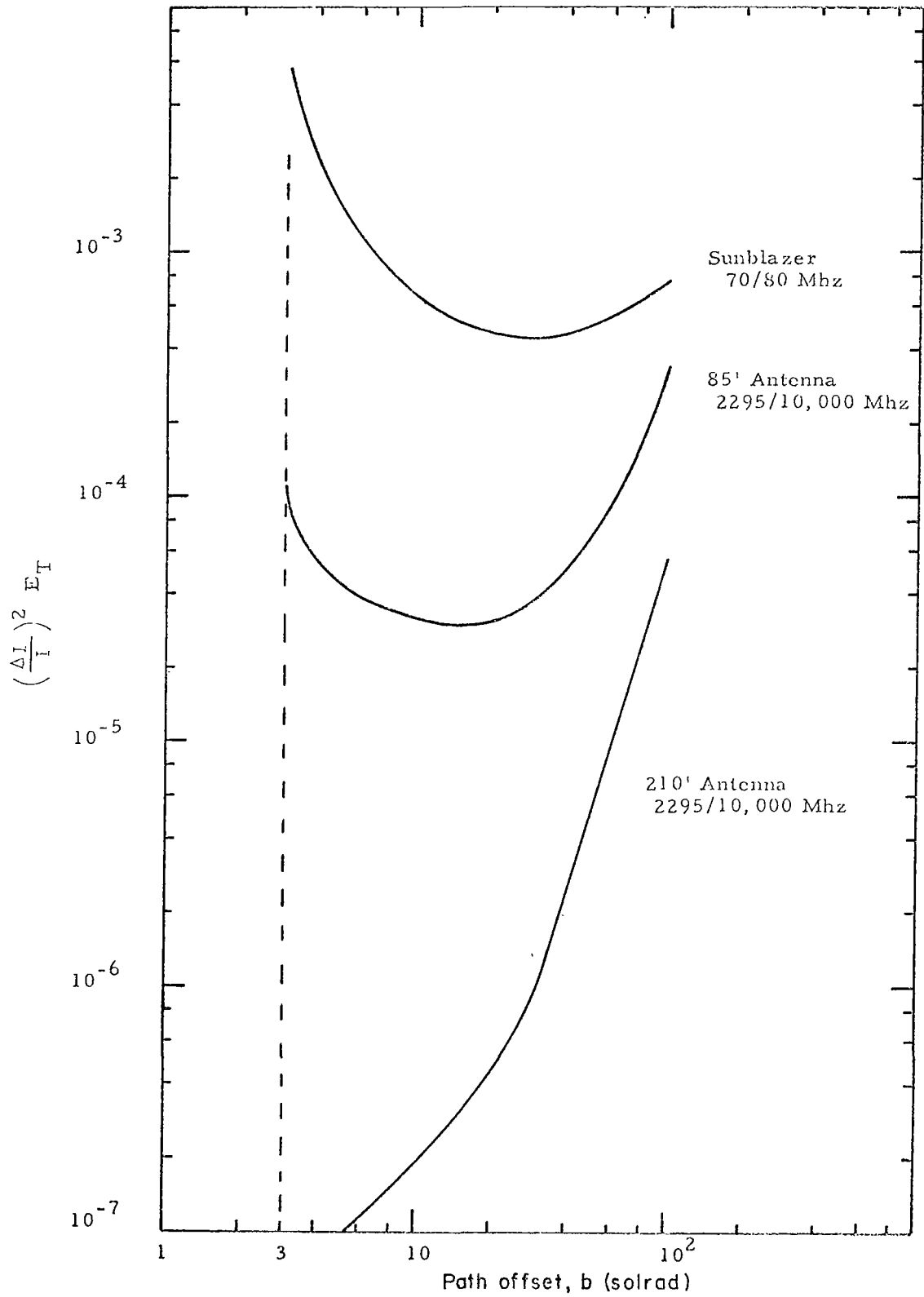


Figure 43 Theoretical Downlink Energy Efficiency Comparison

Again the three systems are compared: (1) 85' antenna at S/X-band, (2) 210' antenna at S/X-band and (3) the proposed Sunblazer system at 70/80 MHz. For the S/X system $1/2 \mu s$ pulse is assumed, a value much greater than the channel limited pulse width, but compatible with the art of magnetic recording. The proposed Sunblazer system employs a $25 \mu s$ pulse width.

Using these pulse widths in Eq. (26) along with the parameters in Table II yields Fig. 44. As in Fig. 43, Fig. 44 shows Sunblazer "cut off" because of high solar noise when the propagation path is within 5 solrad of the Sun, a region that is probably inaccessible for other reasons. Sunblazer, however, is superior (in the limited viewpoint of this section) to the S/X-band system when the propagation paths are greater than 5 and 8 solar radii from the Sun, if 85' and 210' dishes are used respectively.

In the practical case therefore, the tradeoff between S/X-band systems and the Sunblazer system is that S/X performs within 5 solrad of the Sun whereas Sunblazer does not. As discussed elsewhere, the Sunblazer system probably would not penetrate 7 or even 10 solrad.

Figure 45 shows the percentage error in the measurement of I for a transmitted energy of 6 joules per ranging code word. From Fig. 45 it is possible to compare in absolute terms the performance of Sunblazer and the S/X-band systems. For path offsets greater than 80 solrad, error in I exceeds 30% and 10% for the 85' and 210' antennas respectively. These errors can be reduced by averaging over a number of samples, at the cost of decreased accuracy in the electron density fluctuation.

Downlink Conclusions

The following conclusions can be stated as a result of the downlink analysis.

1. S and X-bands are the only frequencies for a downlink experiment with existing facilities. Supporting this is both S/N analysis and the fact that operational downlink equipment exists at 2295 MHz and an X-band telemetry downlink is in preparation for future missions.
2. For propagation paths within 7 solrad, or 5 at the very least of the Sun, S/X-band using either the 85' or 210' antenna is superior to the proposed 70/80 MHz Sunblazer system.
3. A continuous wave (CW) system is marginal because of inadequate spacecraft power. This forces the downlink experiment to a pulsed type of signal or frequency ≈ 6 GHz.

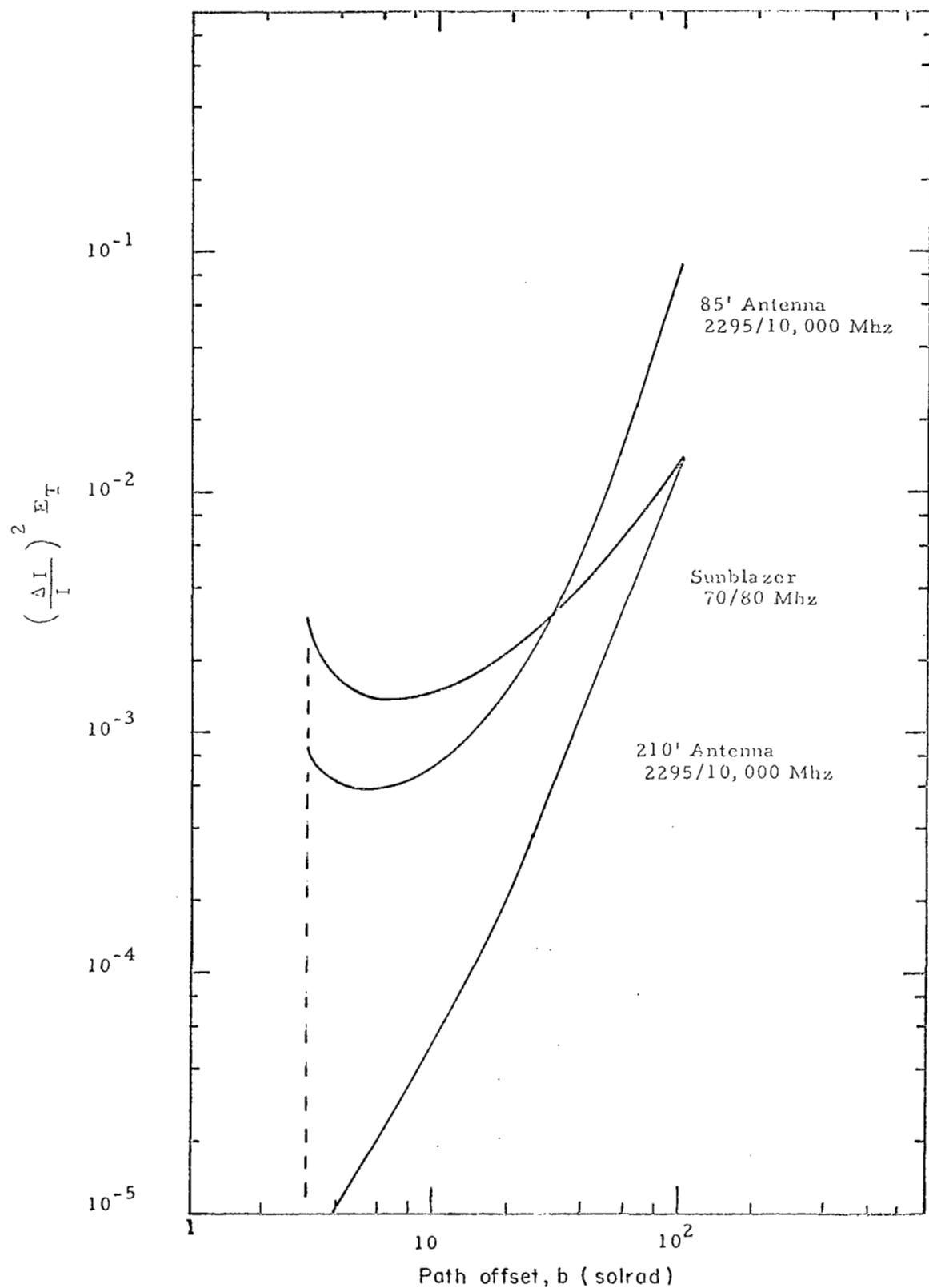


Figure 44 Practical Downlink Energy Efficiency Comparison

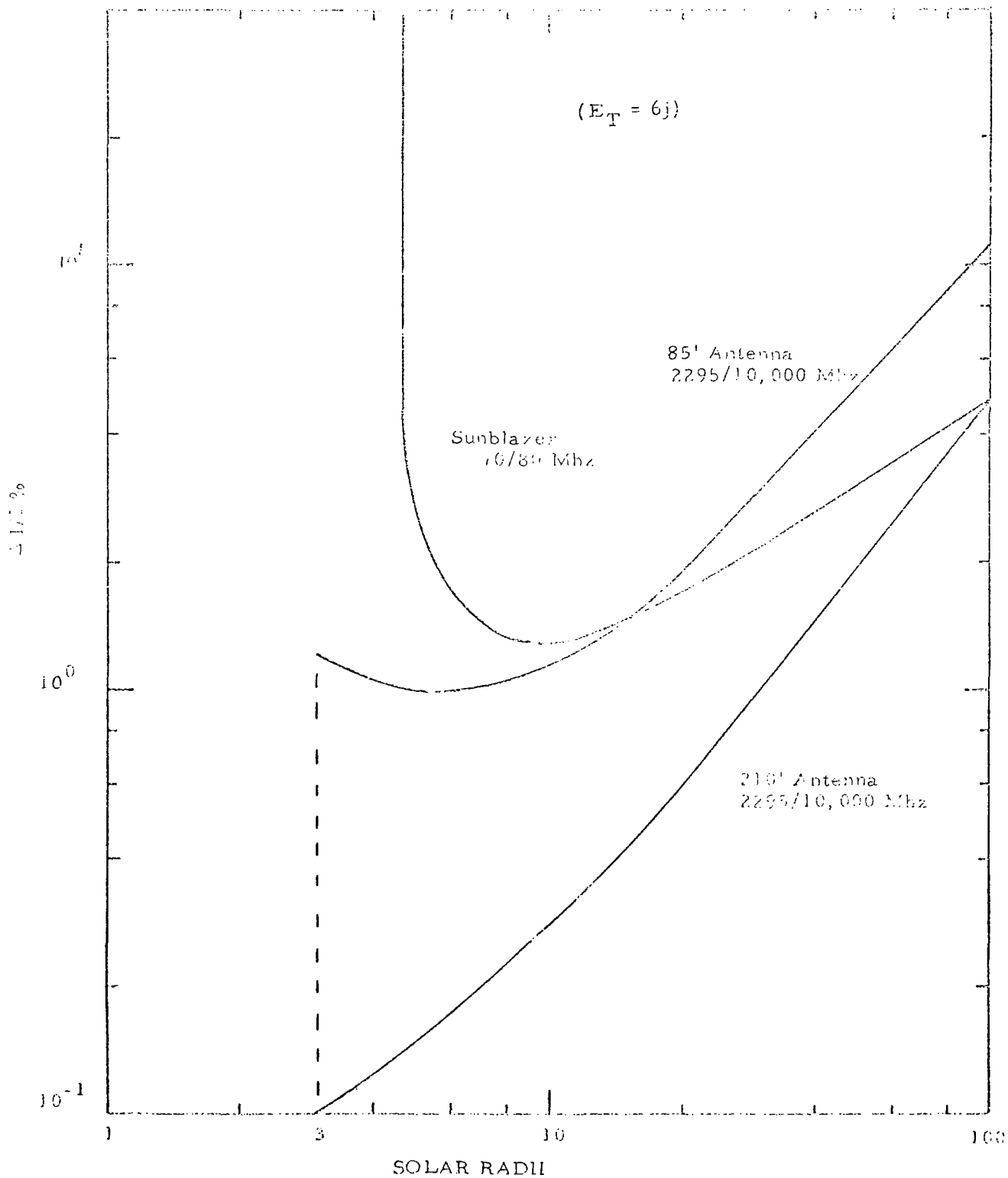


Figure 45 Error in Measurement of l - Downlink

4. Real time data processing is not possible with pulses. As a result raw data must be recorded on magnetic tape and reduced by computer on the ground.
5. For path offsets greater than 5 solar radii and a sufficiently quiet Sun, the measurement accuracy of I is better for the 70/80 MHz El Campo system than it is for the S/X band system.
6. The 210' antenna at Goldstone is the first choice for the experiment; however, it is tightly scheduled for other missions. Scheduling therefore probably eliminates it as a candidate for the Sunblazer experiment.
7. The 85' antenna is the prime candidate for the Sunblazer experiment. Scheduling is not a severe problem since a large number of antennas are in operation.

Uplink Analysis

The uplink analysis proceeds in the same general manner as that of the downlink. There are, however, two important distinctions between the uplink and the downlink. The first is the effective noise temperature of the receiver, which is independent of the propagation path. This is because the wide beamwidth of the spacecraft receiving antenna always "sees" the Sun. The second difference is radiated power. The uplink can easily radiate an average power which is 30 to 40 db greater than downlink power. In short whereas the downlink is limited by average prime power, the uplink is only equipment limited. This means that measurement accuracy can be increased in comparison to the lower power downlink, and more important the greater S/N margin maintains the link during any deep fading phenomenon near the Sun, during solar storms, and in the event that lesser facilities substitute during schedule conflicts.

Facilities. -The discussion in the Facilities - Receiving Antenna section concerning antennas still applies. High power transmitters are not generally available, but 10 kw transmitters will suffice except during the most severe solar storms.

Referring to Table V Stanford, Lincoln Labs and NASA - Goldstone have transmitters capable of interplanetary communication. The Stanford transmitters were used for the Pioneer VI and VII experiment in conjunction with a 150' antenna. Lincoln Labs has a planetary radar at 1295 MHz using an 85' antenna. This radar is capable of generating 2 ms pulses at 5 Mw peak power (max. average power is 150 kw). Modulation within the pulse however is not possible. Lincoln Labs also has a planetary radar at 7.9 GHz. This radar radiates 400 kw average power and has a maximum signal pulse width of 12 μ s. NASA has transmitters at 2115 \pm 5 MHz (which are used for uplink communications) in the space

program. Many transmitters are available at the 10 kw average power level, and as much as 400 kw has been generated; 100 kw is readily available at Goldstone. NASA also has a 100 kw planetary radar at 238 \pm 5 MHz at Goldstone along with a 15-25 kw transmitter at 8.9 GHz.

In the deep space program the majority of equipment and experience is at S-band. While this fact is not the driving factor in frequency selection it cannot be overlooked.

Noise Temperature. -The three sources of noise (galactic, solar and receiver) are considered here. Both galactic and solar noise are negligible at all microwave frequencies considered for the uplink. Assumed receiver noise temperature is given in Fig. 46. Transistors or tunnel diode amplifiers in the receiver front end will yield the noise temperatures shown in Fig. 47. This can be checked with Fig. 38.

S/N versus Frequency - Uplink. -The S/N given in Fig. 47 is obtained from the range equation. The pertinent parameters are:

Transmitter Power = 10 kw

Antenna = 85' diameter

Bandwidth = Channel phase jitter bandwidth at 3 solrad $\left(16 \frac{2300}{f_o (\text{MHz})} \right)$

Receiver Gain, same as downlink, 20 db

Range = 2 a. u.

Noise Temperature in Fig. 46

System Loss = 3 db

The bandwidth used in Fig. 47 is channel phase jitter bandwidth which we use for the phase lock loop bandwidth. As shown in Fig. 47 the S/N above 1000 MHz is excellent and as in the downlink analysis the lower frequencies are not attractive using existing antennas. Note that the 85' antenna is used in the uplink calculation; the 210' antenna has been excluded because the 85' antenna is adequate.

Comparison of S-Band Uplink with Sunblazer System. -In this section a comparison is made between the accuracy of the I measurement using an S-band uplink on carrier frequencies of 2115 and 3115 MHz and the accuracy with the 70/80 MHz Sun System. The uplink is assumed to employ phase modulation as did the Pioneer VI and VII experiment. The use of a ranging code on an uplink is unlikely because of receiver complexity, i. e., delay lines and code correlators. Receiver complexity translates into spacecraft weight, volume and reliability problems.

Group time delay [Eq. (13)] is written in terms of modulation frequency phase shift in Eq. (28)

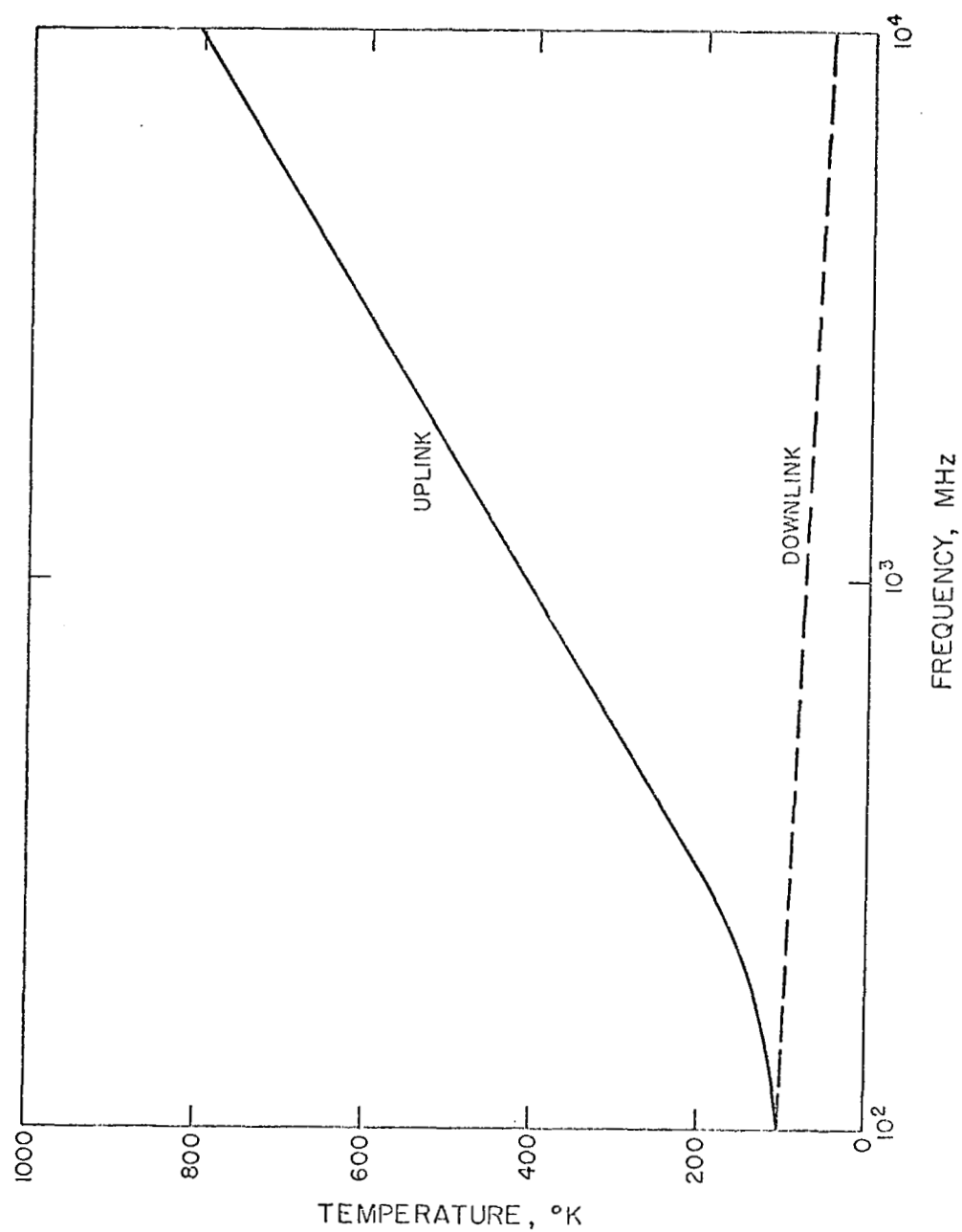


Figure 46 Receiver temperature versus Frequency

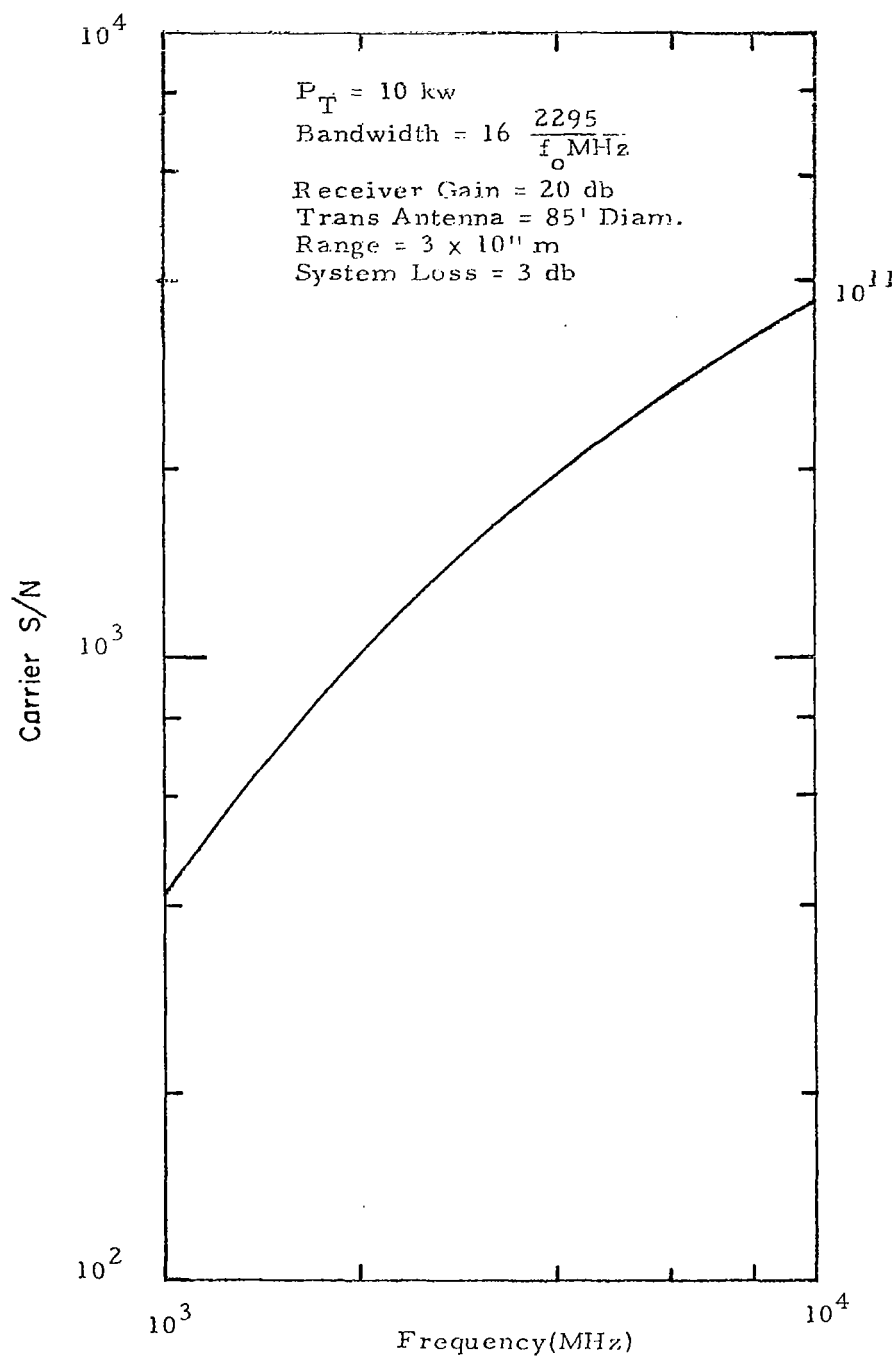


Figure 47 Phase Lock Loop S/N vs. Frequency (Uplink)

$$T_D = \frac{\Phi}{2\pi f_m} = \frac{1.35 \times 10^{-7}}{f_1^2} \left(1 - \frac{f_1^2}{f_h^2}\right) I \quad (28)$$

The minimum phase shift which can be measured is: (where f_m = modulation frequency)

$$\Delta \Phi = \frac{1}{\sqrt{2 S/N}} \quad (29)$$

where S/N = signal-to-noise ratio in a bandwidth equal to the reciprocal of the channel coherence time.

In the downlink section and Fig. 47 the bandwidth used to obtain phase lock S/N is the channel phase jitter bandwidth (16 Hz @ 2295 MHz) which varies inversely with the carrier frequency. This is the minimum bandwidth possible on the communication link and determines if communications are possible at all. In order to determine the error in the modulation phase (and therefore the error in I) the reciprocal of the channel coherence time is used. This bandwidth at microwave frequencies is larger than the channel phase jitter bandwidth and does not vary with frequency. As a result the S/N used in Eq. (29) is smaller than that of Fig. 47.

Error in I therefore is:

$$\frac{\Delta \Phi}{\Phi} = \frac{\sqrt{\langle \Delta^2 I \rangle}}{I} = \frac{f_1^2}{2\pi f_m (1.35 \times 10^{-7} \left(1 - \frac{f_1^2}{f_h^2}\right) I \sqrt{2 S/N}} \quad (30)$$

The S/N at S-band is equal to 160 and is obtained from the range equation using the following parameters.

| | | |
|----------------------|---|---------------------------------|
| Power transmitted | = | 10 kw |
| Transmitting Antenna | = | 85' Diam. |
| Receiver Gain | = | 100 |
| Range | = | 2 a.u. |
| Noise Temperature | = | 600°K at S-band |
| System Loss | = | 3 db |
| Receiver Bandwidth | = | 100 Hz (coherence time = 10 ms) |

The receiver bandwidth of 100 Hz is obtained from the reciprocal of the channel coherence time (see Appendix 3).

Figure 48 shows the percentage error in I versus path offset for an S-band system and the Sunblazer system. The curve for the Sunblazer system is obtained directly from Fig. 45.

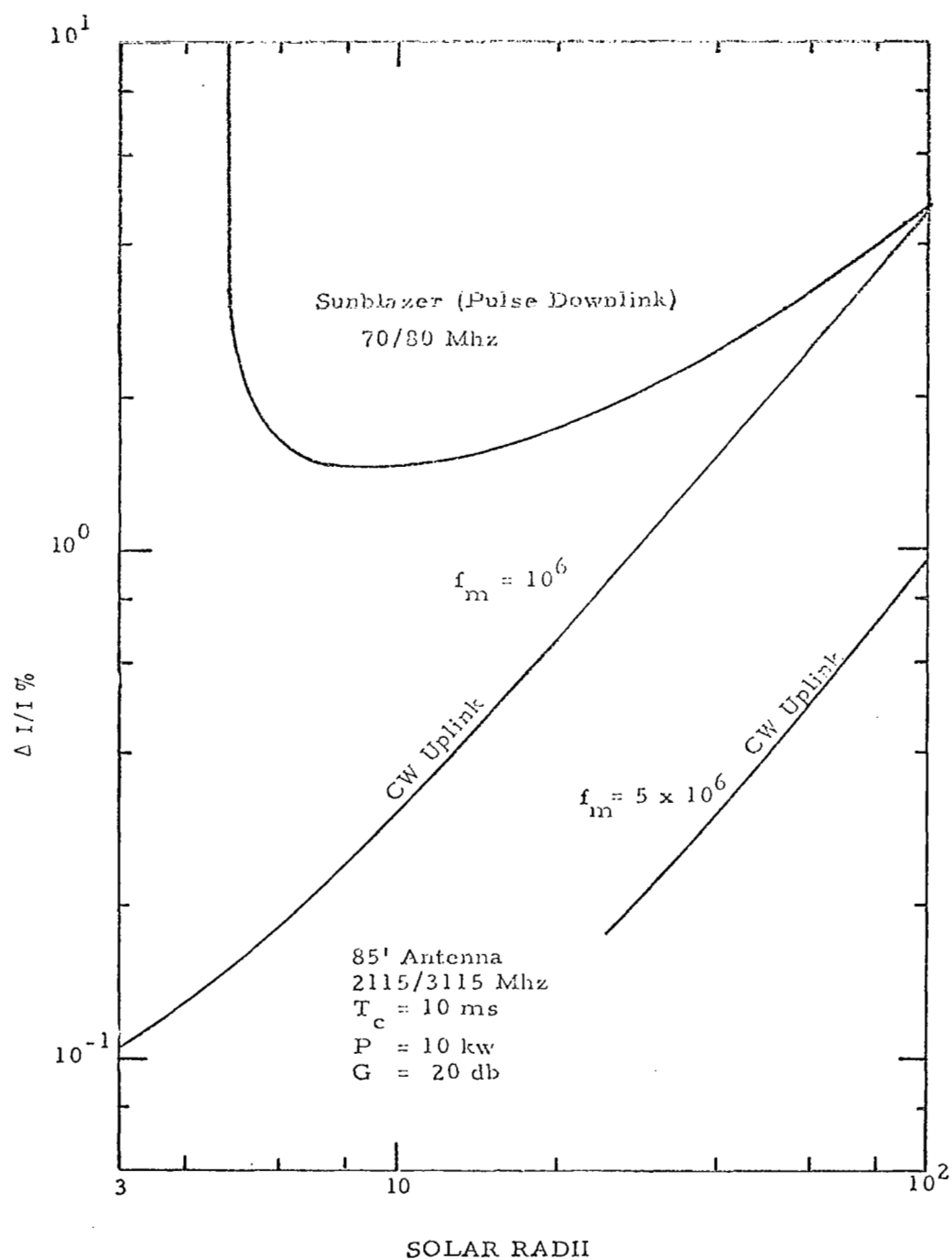


Figure 48 Uplink Error in Measurement of Integrated Electron Density

Note in Fig. 48 there are two curves shown for the S-band system. One curve is for a modulation frequency of 10^6 Hz and the other for 5×10^6 Hz. The phase modulation system has the advantage of increasing resolution by increasing the modulation frequency without seriously increasing system complexity. Near the Sun a lower modulation frequency can be used, at larger path offset where higher resolution is required, the modulation frequency can be increased. In this manner an S-band uplink can always measure I with greater accuracy than that obtained with Sunblazer.

The S-band uplink is expending considerably more energy per measurement than the Sunblazer downlink. Energy, however, is of little importance on the uplink, since high power transmitters are available, and may as well be used. This is not true on the downlink where primary power is severely limited.

It remains to determine if cycle ambiguities can be resolved, a problem discussed in the Spacecraft Propagation Experiments section in connection with Fig. 18. This figure shows the group delay in terms of the number of cycles of the modulation frequency. In order to resolve the cycle ambiguities the modulation frequency must be changed and the phase shift noted at each frequency. In the example of Fig. 18 modulation frequencies of 10^6 Hz and 9×10^5 Hz are used. As the example indicates the phase shift measured on each frequency is unique to an integral number of cycles of phase shift. The phase resolution is given in Eq. (29). Since the S/N is equal to 160 the resolution is 3.2° . This resolution (equal to about 10^{-2} cycles) is sufficient to resolve the ambiguity problem.

Telemetry

Telemetry from the spacecraft is required whether an uplink or downlink is used. In the uplink case telemetry requirements are more stringent since solar corona data in addition to any command/control information must be telemetered.

Assuming an uplink experiment is employed there are two possible methods of retrieving the solar corona data. One method is to continuously telemeter the data as the experiment progresses (Continuous Mode) and the second method is to record the data aboard the spacecraft and then at an advantageous orbital position "dump" the data (Data Dump Mode). A comparison between the two modes is shown in Table VII.

For the Continuous Mode X-band telemetry will be required to minimize signal/solar corona interaction. The Data Dump Mode could use S- or X-band. Assuming X-band and binary phase modulation (coherent phase shift keying) is used in both cases the bit error probability versus data rate (bits/sec) can be determined. Figure 49 gives the bit error probability

vs E/N_0 (ratio of bit energy to noise energy). E/N_0 versus bit rate can be determined from the range equation and the parameters of Table IV which in turn yields Fig.50 , the bit rate versus bit error probability.

Table VII Telemetry Mode Comparison

| | Advantage | Disadvantage |
|-----------------|-------------------------------------|---|
| Continuous Mode | No data recording aboard spacecraft | Low data rate as propagation path nears Sun |
| Data Dump Mode | Recording equipment required | High data rate |

Table VIII Parameters to Determine E/N_0 vs. Bit Rate

| | Continuous Mode | Data Dump Mode |
|--------------------------|--|-------------------------------------|
| Radiated Power | 5W | 5W. |
| Transmitter Antenna Gain | 10 | 10 |
| Receiving Antenna | 210' Antenna ($A_e = 1900 \text{ m}^2$) | at Goldstone |
| Noise Temp. | 100°K^* | 20°K^{**} |
| Range | $3 \times 10^{11} \text{ m}^*$ | $2.1 \times 10^{11} \text{ m}^{**}$ |

* Propagation path 3 solar radii from Sun

** Propagation path 100 solar radii from Sun

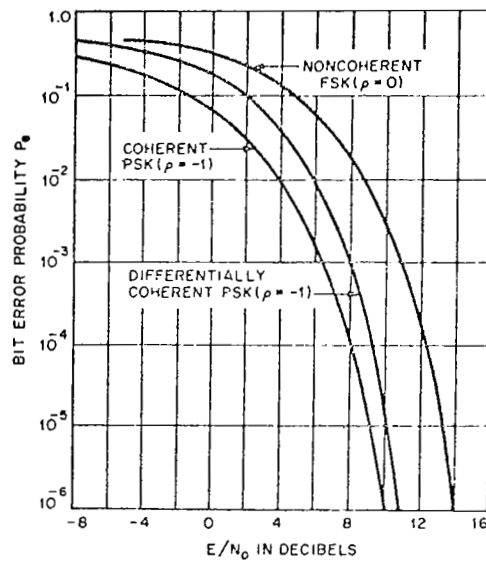


Figure 49. Error Rates for Binary Phase Modulation.
 From J. G. Lawton, "Comparison of Binary
 Data Transmission Systems," Proceedings of
 the Second National Conference on Military
 Electronics; 1958.

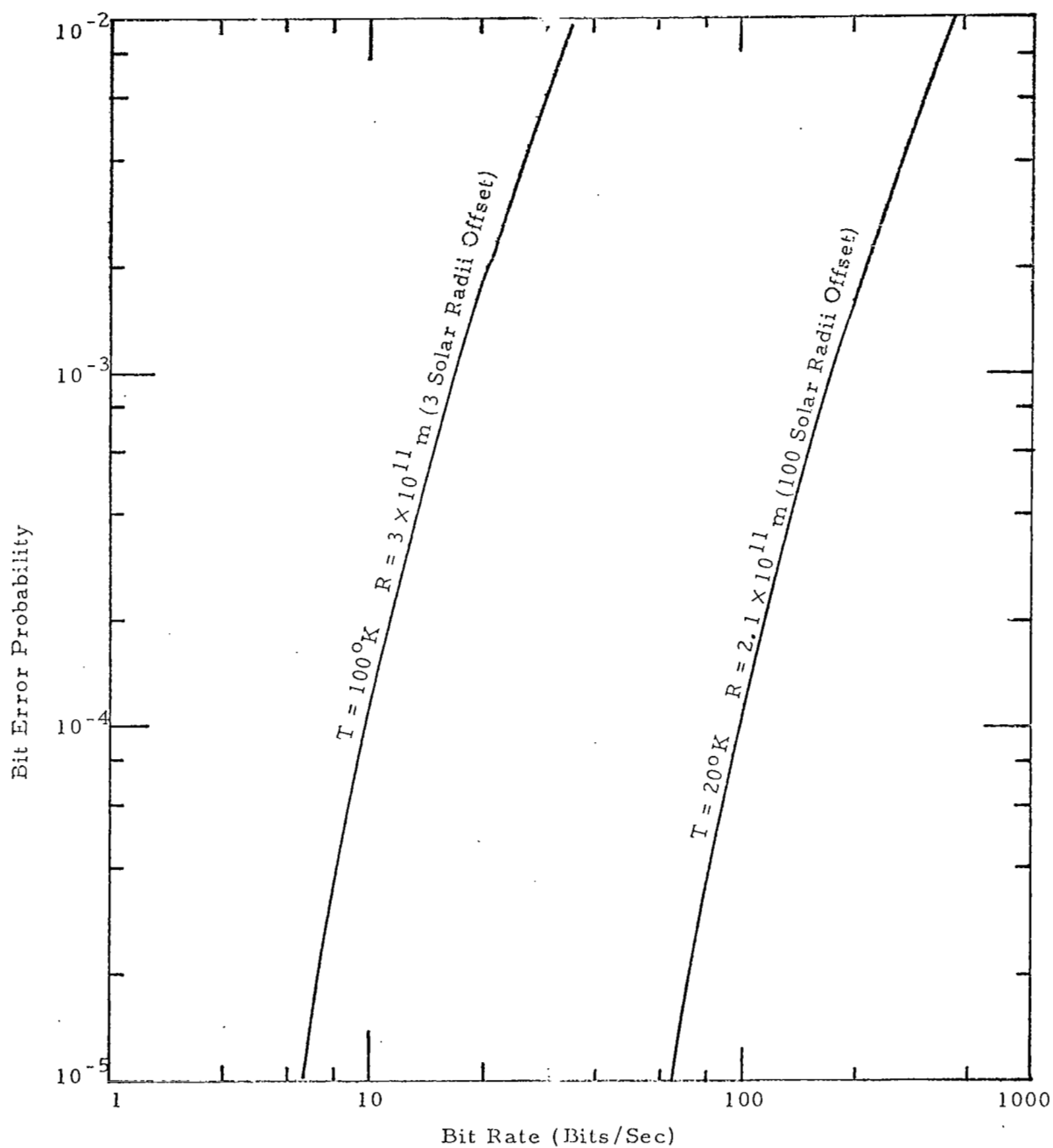


Figure 50 Telemeter error rates

Assuming an error probability of 10^{-4} is adequate for the telemetry link data rates of 10 and 100 bits/sec are shown for the Continuous and Data Dump Modes respectively in Fig. 50 . It remains to trade off these bit rates with the penalties incurred (recording equipment, etc.) by each system before a selection can be made. This involves the overall spacecraft design and weight budget.

Telecommunication Link Calculation

Using available antenna performances, noise figures and system losses from the Viking experiment we have compared a proposed S-X band uplink with the MIT-El Campo downlink. The calculation and results listed in Tables IX and X show clearly that if radio probing is to be done as close as 3 solrads only S-X band has sufficient signal-to-noise-ratio. Processed data signal for S-X band is almost 13db above noise while El Campo's signal is more than 30db below noise.

Table IX
TELECOMMUNICATION LINK CALCULATION

MIT - EL CAMPO DOWNLINK
At 3 Solar Radii

| PARAMETER | VALUE |
|--|------------|
| Total Transmitter Power 2KW | 63 dbm |
| Receiving Antenna Gain El Campo | 50 db |
| Space loss 2 AU | -241.5 db |
| Transmitting Antenna Gain | 1.8 db |
| Receiving Antenna Pointing Loss | -3 db |
| Receiving Circuit Loss | -1.5 db |
| Net Circuit Loss | -194.2 db |
| Total Received Power | -131.2 db |
| T System = 4×10^{60} K $kT = 5.6 \times 10^{-17}$ | |
| Receiver Noise Spectral Density (N/B) | -132.5 dbm |
| Received Data Subcarrier Power | -131.2 db |
| Bit Rate $(1/T) = \frac{1}{3 \text{ msec}} = 333 \text{ Hz}$ | 25.2 db |
| Required ST/N/B | 10 db |
| Threshold Subcarrier Power | -97.3 db |
| Performance Margin | -33.9 db |

Table X

TELECOMMUNICATION LINK CALCULATION

PROPOSED S/X BAND UPLINK WITH ONBOARD DATA REDUCTION

At 3 Solar Radii

| PARAMETER | VALUE FOR S- BAND |
|--|----------------------|
| Total Transmitter Power 100 KW | 80 dbm |
| Transmitting Antenna Gain 85 ¹ | 51.8 db |
| Space Loss 2 AU | - 269.2 db |
| Receiving Antenna Gain | 20 db |
| Receiving Antenna Pointing Loss | - 3 db |
| Receiving Circuit Loss | - 1.5 db |
| Net Circuit Loss | - 201.9 db |
| Total Received Power | 121.9 db |
| T System = 980°K (based on Viking) effective system noise temperature based on 6.5 db noise figure | |
| Receiver Noise Spectral Density (N/B) | - 168.7 dbm |
| Carrier Modulation Loss: 10 log. 59 (based on $\Delta\phi = 1$ radian, $J_0^2(1) = .59$) | - 2.3 db |
| Received Carrier Power | - 124.2 db |
| Carrier APC Noise BW ($2B_{LO} = 14$ HZ) | 11.5 db |
| CARRIER PERFORMANCE-TRACKING (one-way) | |
| Threshold SNR in $2B_{LO}$ | 8 db |
| Threshold Carrier Power | - 149.2 db |
| Performance Margin | 25 db |

Table X (Continued)

TELECOMMUNICATION LINK CALCULATION

PROPOSED S/X BAND UPLINK WITH ONBOARD DATA REDUCTION

At 3 Solar Radii

(continued)

| PARAMETER | VALUE FOR S-BAND |
|--|------------------|
| DATA CHANNEL | |
| Modulation Loss: $10 \log_{10} \frac{39}{2J_1^2(1)} = .39$ | -4.1 db |
| Received Data Subcarrier Power | -120.0 db |
| Bit Rate (1/T) 100 BZ (Appendix 3) | 20.0 db |
| Required ST/N/B | 10 db |
| Threshold Subcarrier Power | -138.7 db |
| Performance Margin | 12.7 db |

CRITIQUE OF THE MIT SUNBLAZER STUDY

This topic is conveniently divided into four parts: the study of suitable orbits, the design of the spacecraft configuration and attitude controls, the choice of frequency and hardware for the experimental propagation link, and finally the coordination of the other three.

Orbit

We consider the selection and description of orbits to be the best contribution of this report. In the recommended orbits the spacecraft's aphelion occurs when it is behind the Sun as viewed from Earth. This produces a triple conjunction, which is illustrated in the various Sunblazer orbit figures. Three advantages result. First and most important is that by prolonging the conjunction period a great deal more data can be gathered which has a much greater chance of including unusual solar events. Second, the probe will spend nearly 50 days in the vicinity of each of the two reversals in the solar encounter profile (see Fig. 51). The Sun rotates twice in this time and allows one to separate persistent phenomena from the transient ones that are missing the second time around. Third, and least important, the triple conjunction provides two reversals in the velocity of the line-of-sight with respect to the Sun. This provides a greater variety of relative velocities between the line-of-sight and the solar wind for statistical studies of the fluctuations in the corona.

Spacecraft Configuration

The Sunblazer study recommended a spacecraft that is spin stabilized with the spin axis pointed at the Sun. The solar panels on the sunlit sides would then be in the sunlight at all times. The recommended attitude control system is based on a simple Sun direction sensor, and the thrust necessary to precess the spin axis is achieved with the aid of solar vanes or sails. These basic principles are sound, and we have adopted them. However, there is room for improvement by using a passive attitude control technique for the steady state condition as discussed in the Attitude Control section of this report.

Propagation Experiment

This portion of the Sunblazer study is unsatisfactory. The choice of frequencies on the order of 100 MHz is inept for many reasons, most of which are listed below:

1. The Pioneer VI solar occultation experiments showed that the Sun's disc has an S-band radius four times the visible

radius. Near 100 MHz the interaction with the corona will be much stronger and the effective radius for that frequency will be at least as large and probably a great deal larger. This means that the effective disc size for 100 MHz will obscure most of the region of interest! A likely cause for the S-band "radius" is excess phase jitter that spreads the signal in frequency until its spectral density was below the noise. If this interpretation is correct, we expect a 100 MHz radius of at least 7 solrad, where a bandwidth increase starts to be perceptible in Goldstein's S-band data for Pioneer VI.

2. The large Sunblazer ground antenna array for 100 MHz and the pulse receiver system (not continuously phase locked) involve hardware and techniques which are new to deep space. This cost and associated development risk is unnecessary in view of the very successful S-band uplink to Mariner IV which employed only standard deep space equipment.
3. Our communications link analysis shows that even in a theoretical sense the MIT choice is not optimum. They conveniently chose a one million °K corona, or quiet Sun, and on this basis neglected solar noise compared to galactic noise. A disturbed Sun can be 40 db noisier. Our link analysis assumes 20 db noisier (geometric mean), or about 10^8 deg. K. This solar noise would equal galactic noise at about 15 solrad of path offset and would exceed galactic noise by 10 db at about 8 solrad.
4. The very limited tracking facilities, mainly one very large array, would provide only a few hours tracking per day, even if the huge complex thing could operate without failure. Such intermittent tracking is unsatisfactory in view of the large number of interesting but infrequent solar events which are likely to be missed. Moreover, such intermittent tracking cannot even determine the time constants of routine events within the important range of about 6 to 12 hours. The frequency and duration of events were noted in the Propagation Experiments section and in the Present Knowledge Section of this report.
5. Strong scattering at low frequency is less informative than weak scattering at high frequency, because: (a) the equations for strong scattering are too difficult to solve with any confidence; and (b) multiple scattering blurs the details of the single scattering function.

Coordination

The Sunblazer project staff was not properly coordinated; at least those who studied orbits did not talk to those who did the link analysis, or vice versa. From an orbital point of view the orbit based on a July launch was selected for special attention as a leading candidate. This orbit would cause a period of conjunction to occur 18 months later during the latter part of January. However, at this time of year a downlink receiving antenna on the ground would be looking almost directly at the center of the galaxy and would be picking up as much as 10 db excess noise! The following three figures (Figs. 51, 52 and 53) demonstrate this. Moreover, the declination of the Sun is lowest in January, so the effect of the secant of the zenith distance is to aggravate the ionospheric errors. Finally, the days are shorter, hence also the tracking time for the craft behind the Sun, and we have seen that Sunblazer tracking time is critically short under the best circumstances !

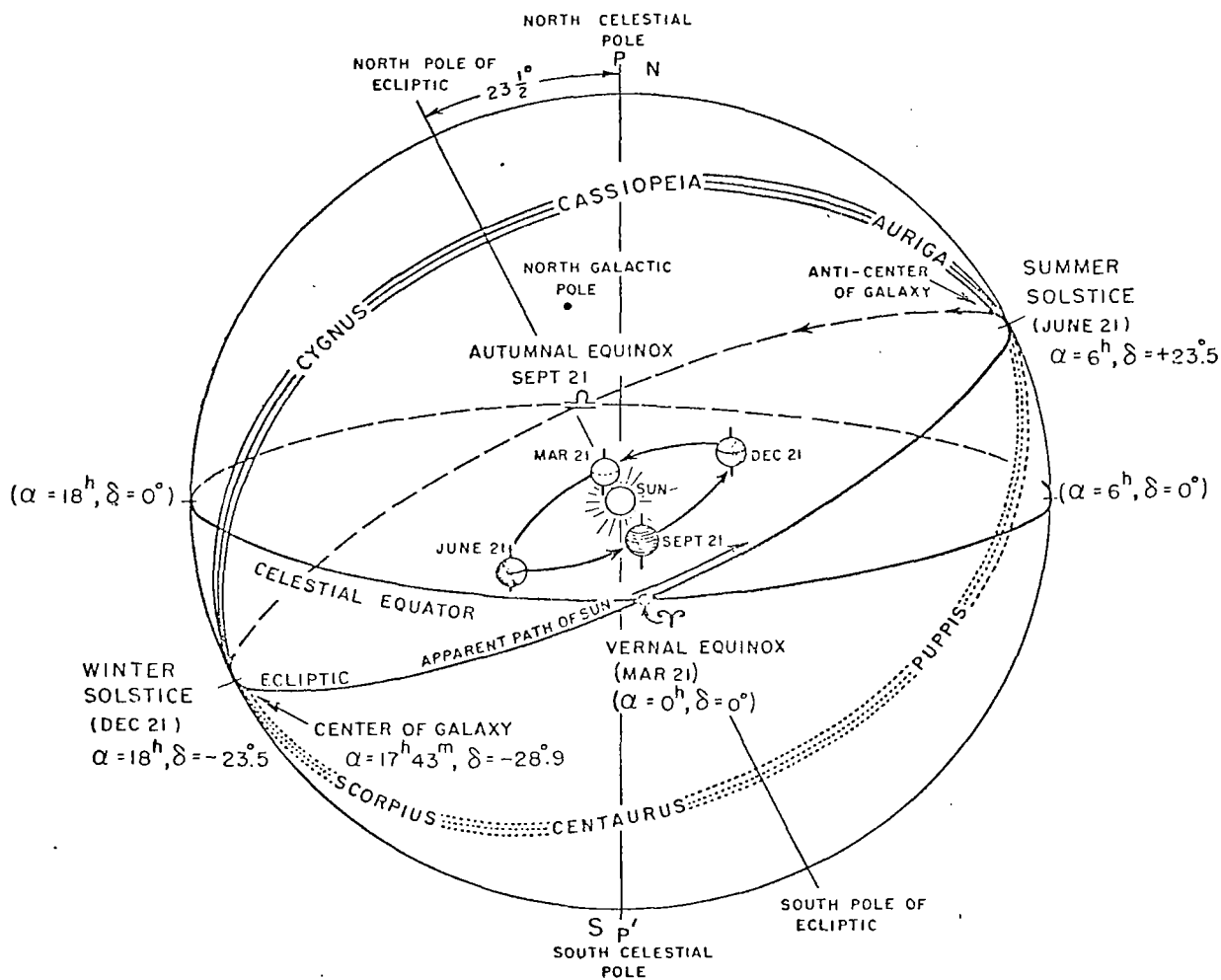


Figure 52 Projection of the earth's orbital motion on the celestial sphere is the ecliptic; this will be unchanged throughout the 26,000-yr precession of the north celestial pole about the north pole of the ecliptic. The galactic circle (for which a few constellations are indicated) is for the 20th century, when P is located within about 1° of α Urae Minoris (Polaris). The north galactic pole is located on the far side of the celestial sphere (away from the reader), as is the dotted portion of the galactic circle. The dates for the equinoxes and solstices are approximate. (Fig. by Gordon W. Wares.) (Ref. 10)

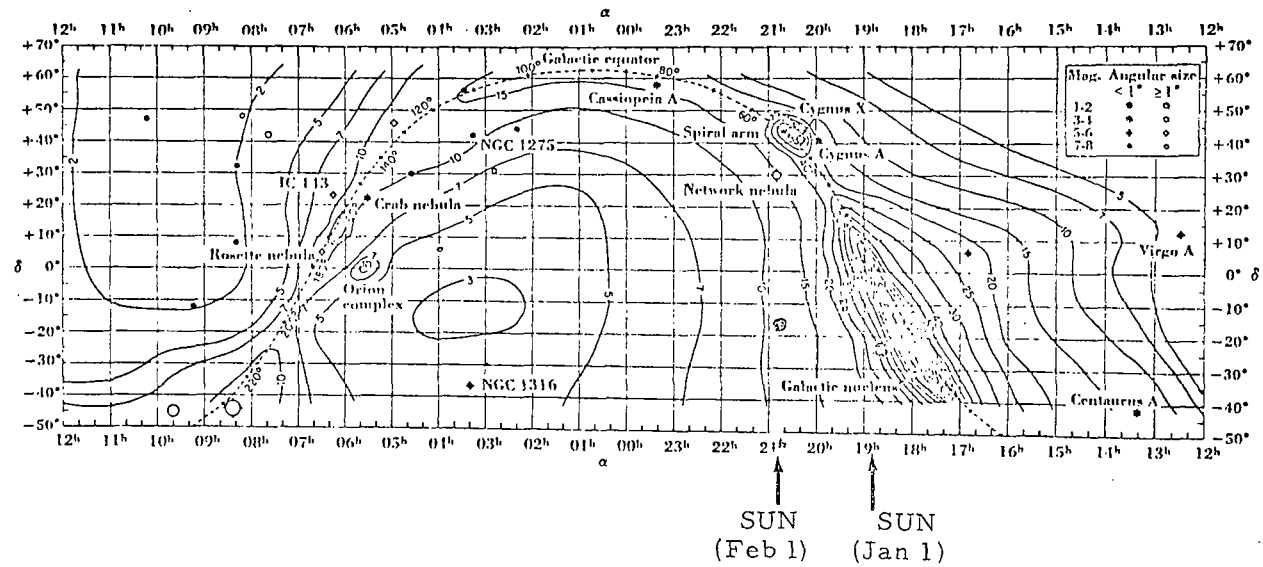


Figure 53 Radio Sky at 250 Mc as Observed with the Ohio State University 96-helix Radio Telescope. (Ref. 11)

PASSIVE SPACECRAFT ATTITUDE CONTROL

The usual technique for passively stabilizing a deep space probe is to spin it like a planet, i. e., spin it about an axis perpendicular to the plane of the ecliptic. This is the familiar technique for stabilizing Pioneer spacecraft. However, in the case of spacecraft launched by the Scout booster, the last stage of the Scout does not know which way the ecliptic plane is oriented. This is because the uppermost Scout stage is a simple unguided spin-stabilized stage. Therefore a system that would find the ecliptic or retain memory of the direction of the ecliptic throughout the staging process would consume valuable weight otherwise allotted to the payload. The MIT Sunblazer studies proposed a good solution to this problem, viz, a spinning spacecraft with its axis pointed at the Sun. The sun direction is the one obvious direction that a simple sensor can find and follow. The MIT study discussed specific means for guiding on the Sun, both active and passive. However, we have devised a new scheme which we believe to be superior to theirs as regards longevity, simplicity, weight and volume of the necessary equipment. The possible uses of this novel attitude control extend beyond the specific mission of the solar probe, so we describe the attitude control system in a general way that will be applicable to any spacecraft that is spin stabilized with its axis pointed at the Sun.

The first requirement of a spin-stabilized spacecraft is that its axis of rotation be the axis of maximum moment of inertia. It is well known that this is the only axis about which a nearly rigid body will rotate stably for an indefinite length of time. If the spacecraft is symmetrical about its axis, this gives it the general shape of a pillbox as opposed to the unstable cigar-shaped configuration.

Figure 54 illustrates the preferred attitude control technique in a schematic way. The eight vanes shown take advantage of solar pressure to achieve passive attitude control. The number, size and shape of the vanes may be altered in a wide variety of ways, apart from the essential features described below. During detailed design, some suitable modifications will permit the vanes to be folded during launch. Eight vanes are shown, but a final design may have four, six, or even ten. The vanes attached to the back surface are shown hatched to avoid confusion with those attached to the front. The top view shows the back vanes tilted so that light reflected from them does not strike the back side of the front vanes. The front faces the Sun so that each front vane shades approximately half the corresponding back vane. The latter are slightly shorter than the front ones in the radial dimension so that the outer edge of each back vane is shaded just as much as the rest of the vane, even when the spacecraft is tilted a few degrees away from the Sun.

We now show that the solar pressure develops torque in the proper direction to track the Sun. Suppose that the tilted position shown in the front view of Fig. 54 is the way the craft appears to an imaginary

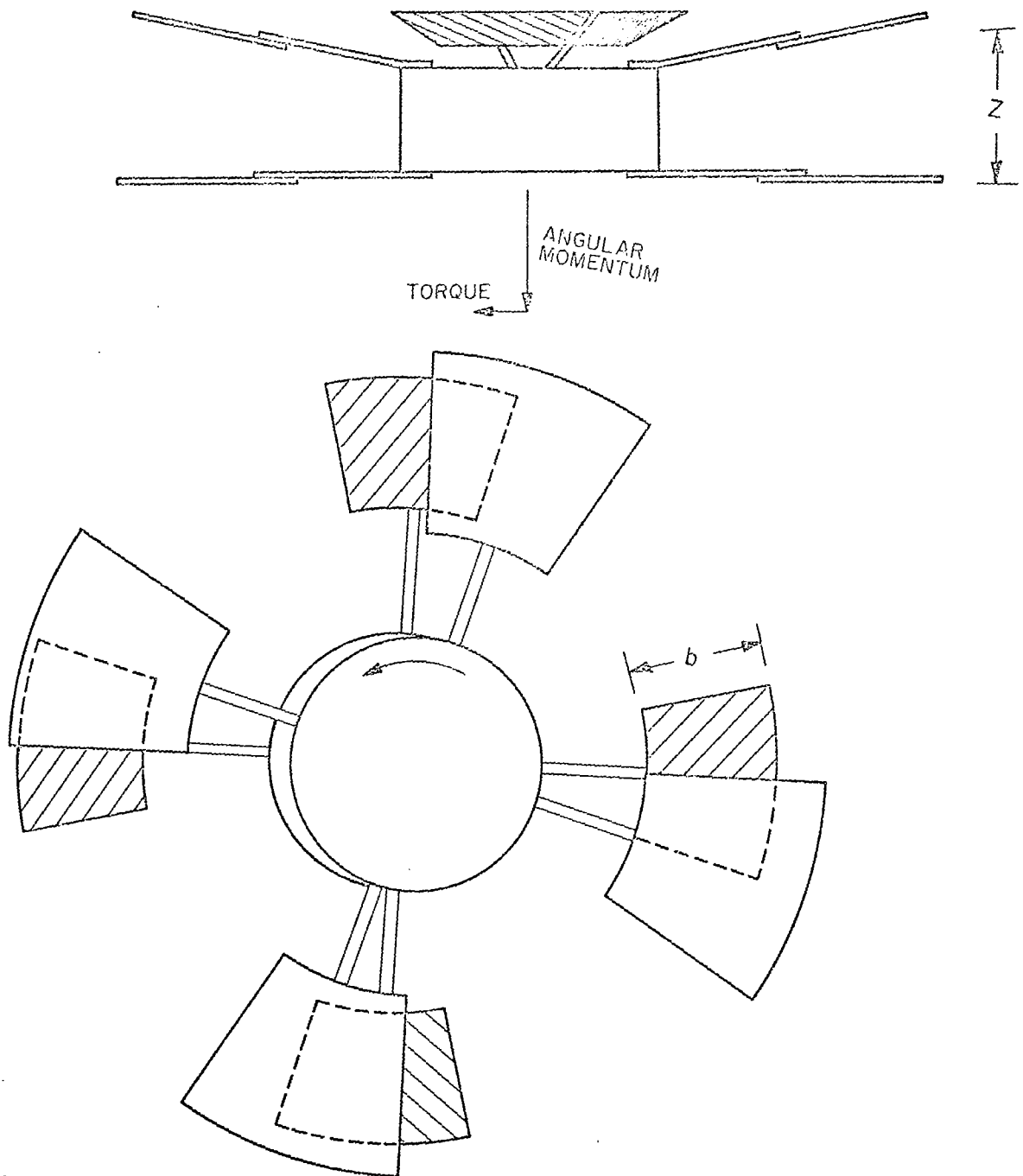


Figure 54 Prepared spacecraft configuration

observer at the Sun. The problem is to show that solar pressure causes torque in the proper direction to precess the axis of the spacecraft in the direction that removes the tilt. Note the effect of the tilt on the amount of vane area exposed to the sunlight. In particular, note in the front view that the back vane at the bottom is more than half shaded, while the back vane at the top of the view is less than half shaded, as a result of the tilt. Therefore, there is a net excess of solar pressure on the top half of the spacecraft, which by the right hand rule causes a net torque vector pointing to the left as illustrated. When the satellite is spinning in the direction indicated, this torque is in the proper direction to precess the spin axis and remove the tilt, as indicated in the small vector diagram in the same figure.

The basic equation for precession under torque is

$$\vec{N} = d\vec{L}/dt \equiv \dot{\vec{L}}, \quad (31)$$

where \vec{L} is the angular momentum vector and \vec{N} is the torque. When the torque and the angular momentum vectors are perpendicular, as they are in this case, then

$$\Omega = N/L = N/I\omega, \quad (32)$$

where Ω is the angular velocity of precession, i. e., the changing direction of the spin axis, I is the moment of inertia, and ω is the spin rate. The torque that results from total reflection at normal incidence is given by

$$N = 2rF a/c, \quad (33)$$

where a (a function of the tilt angle) is the area imbalance between the top and bottom halves of the front face, r is the average vertical moment arm of the area a , c is the velocity of light, F is the solar constant, 1.35 kw/m^2 at 1 a. u., and the factor of two comes from the assumption of total normal reflection.

When the spacecraft is in a 3/4 year orbit, it sees the direction of the Sun changing at the rates

$$\Omega_s = 4.35 \times 10^{-7} \text{ rad/sec at perigee,}$$

$$\Omega_s = 1.7 \times 10^{-7} \text{ rad/sec at apogee.}$$

These rates set an upper limit on the spin rate ω , since the torque is insufficient to keep up with the sum if ω is too large [Eq.(32)]. In the steady state condition in which the spacecraft is locked onto the sun direction and is following it steadily, a small lag angle θ develops between the spacecraft axis and the Sun's direction, since the latter is changing at the rate Ω_s . In the following we derive an expression for θ as a function of ω , and then note that the spin ω is too large when the lag angle θ is excessive.

In this steady state we have $\Omega = \Omega_s$, and Eqs. (2) and (3) give

$$\Omega_s = \Omega = \frac{2rFa}{cI\omega} \quad (34)$$

Next we express a in terms of θ . Using the geometry in Fig. 54 gives

$$a = 2zb\theta, \quad (35)$$

where z is the distance between the front and back sets of vanes measured from the plane passing through the centers of each set, b is the length of each of the back vanes in the radial direction, and θ is the lag angle in question. Eliminating a between the above equations and solving for θ gives

$$\frac{\theta}{\omega} = \frac{c}{2Fr} \frac{\Omega_s I}{2zb}. \quad (36)$$

Let us assume the following reasonable values for the parameters on the right side of Eq. (36)

$$z = 20 \text{ cm (8")}$$

$$b = 20 \text{ cm (8")}$$

$$I = 0.45 \text{ kg m}^2 \text{ (e. g., 44 lbs. at a 6" radius of gyration)}$$

$$r = 35 \text{ cm. (= 13.8")}$$

and the values above for Ω_s and F at apogee and perigee. Now the evaluation of Eq. (36) gives

$$\theta/\omega = 1.86 \text{ deg/rpm}, \quad (37)$$

independent of the spacecraft's position in orbit. This is because both F and Ω_s in Eq. (36) vary inversely with the square of the distance from the Sun, and so the two inverse square dependencies cancel out. From Eq. (37) it is clear that spin rates as high as 1 to 2 rpm are permissible because these allow a reasonably small lag angle of only 1.9 to 3.7 degrees. The dynamic range of preferred spin rates is from about 0.1 to 2 rpm for the dimensions assumed.

As described above, the attitude control scheme appears to be completely passive. However, we tacitly assumed that the vanes have exactly zero propeller pitch. An investigation of the effect of very small residual propeller pitch shows that the effect is strong enough that the roll component of torque must be taken into account. The spin rate of the satellite will accelerate or decelerate in proportion to the roll component N_r :

$$\dot{L} = \omega I = N_r, \text{ and}$$

$$N_r = 2\alpha r F A / c, \quad (38)$$

where α is the average residual pitch angle, A is the sunlit area of the vanes, and r is the average moment arm of A , assumed the same as the moment arm of a . The time required to stop the spin (or double it depending on the sign of α) is given by

$$\tau = I\omega / N_r. \quad (39)$$

We have calculated the time τ using the following

$$A = 20 \times 25 \frac{\text{cm}^2}{\text{vane}} \times 4 \text{ vanes} = 0.2 \text{ m}^2$$

$$\omega = 1.0 \text{ rpm} \quad \alpha = 3^\circ = 0.05 \text{ rad}$$

The result is $\tau = 16.6$ days. This means that a residual propeller pitch as large as the assumed 3° requires some correction to the spin rate about once every week or two.

Fortunately, there is a very simple and completely passive way to control the spin rate by a small amount of bend in each of the back vanes. Recall that these vanes are on the average half shaded and half sunlit when the satellite is steadily tracking the Sun. For spin control we give the sunlit halves a very slight positive propeller pitch to increase the spin rate, and the shaded halves a much larger negative pitch. This combination acts to control the spin rate in the following way. When ω is too high, the precession rate Ω [Eq.(32)] will be too low to keep

up with the Sun. This means that the spin axis of the craft will lag behind the Sun by an angle θ that is larger than normal. Now the increased lag angle lets the Sun illuminate some of the portion of the back vanes that is normally shaded; see the upper vanes in the front view of Fig. 54. Then the sunlight strikes the part with the large pitch that slows the spin and restores its normal rate. Conversely, if the spin is too slow the satellite points closer to the Sun and the only exposed surfaces are those which have the pitch to increase the spin rate. Perhaps other means of passive spin control can be devised by allowing light from the back vanes to reflect against the back side of the front vanes.

An important feature of this form of passive stabilization is that it allows one to monitor variations in the solar pressure. In the brief history of precision tracking of satellites and space probes, there has been a great deal of scientific fallout from the precise orbit determinations. With spacecraft that do not employ gas jets for active attitude control, experience has shown that the largest error in orbit determination is that caused by the uncertainty and changes in the solar pressure. With the passive stabilization scheme described here, an increase in solar pressure will cause an increase in the restoring torque. The torque in turn reduces θ , the angle by which the roll axis lags the Sun; see Eq. (36). Conversely, a decrease in solar pressure causes an increase in the lag angle. Therefore, by monitoring θ with a small sun sensor one has a means for monitoring changes in the solar pressure.

From the point of view of the spacecraft the Sun will appear to move around its axis in a small cone of half angle θ , which may or may not exceed the angular diameter of the disc. In either event a few simple light sensors behind one or more small apertures will provide means to monitor θ precisely. Suppose the spin rate is adjusted to about 1 rpm so that the lag angle equals about 2° . Then it would be desirable to monitor and telemeter the lag angle with an accuracy of about 1 minute of arc, since this represents 1/120 of the total lag angle. The solar pressure is known to fluctuate about 10%, and so this permits measurement of about 1 part in 12 of the fluctuating component.

Sun Acquisition

So far we have discussed only the steady state precession by which the spacecraft follows the sun. Next consider the spacecraft's condition at launch and the problem of turning it toward the Sun so that the passive attitude control system will lock on. At the moment of injection the spacecraft is pointed roughly 90° from the Sun and is spinning at a rate between 140 and 180 rpm.* So the problem falls naturally into two parts, first reducing the spin rate by a factor of 100 to 200, and second precessing the satellite through an arc of about 90° .

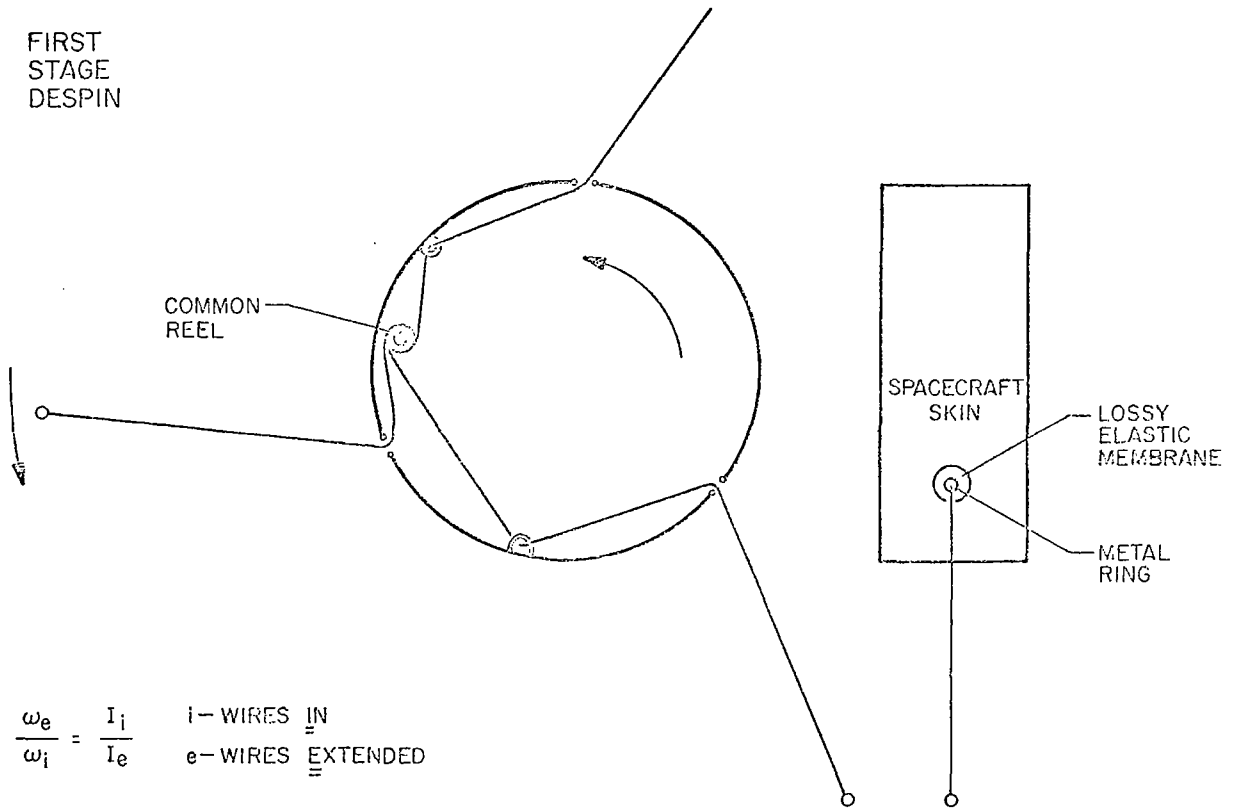
*Scout User's Manual

Undoubtedly most of the spin will be removed by the now-standard yo-yo despin mechanism illustrated in the lower part of the figure on the following page. However, it is risky to remove 99% or more of the spin in a single stage despin mechanism. A small error in the length of the wire or the release of one of the two weights before the other could cause a serious error in the amount of final spin. More important is the behavior of the despin mechanism when the angular velocity vector does not coincide exactly with the principal axis of inertia in the spacecraft. In this case the motion of the body is not a simple spin but a wobbly type of precessional movement (rather like a spinning coin about to stop on a flat surface). To the best of our knowledge no one has analyzed the yo-yo despin mechanism under these conditions, and such an analysis would be well worthwhile since this mechanism is used from time to time in various spacecraft. When the craft is precessing, the movement of the wires will be complicated with waves propagating down the wires to the weights on the end and reflecting back.

However, the safe and conservative way to insure the proper functioning of the despin mechanism is to avoid the issue by first insuring that the craft rotates about its principal axis. Recall that a non-rigid body will ultimately rotate only about its axis of maximum inertial moment, and so the spacecraft should be equipped with small non-rigid parts that dissipate energy as rapidly as possible to speed the spacecraft's approach to its ultimate condition, spinning about the roll axis. To accomplish this we recommend that the yo-yo despin be preceded by a first stage of despin as illustrated in the top portion of Fig. 55. This particular scheme was devised to achieve two benefits. First, it provides a dissipation that will damp out the precessional movement as discussed above, and second it removes a large fraction of the initial spin so that the yo-yo does not have to remove quite such a large percentage of the spin; and therefore, its tolerances are not so critical. Unlike the yo-yo the first stage despin does not allow the wires to spin free and then automatically come off of the craft. Instead the wires reel out slowly and are not released until long after the wires and spacecraft are rotating as though they were a single rigid body in the steady state condition. The dissipative component is the lossy elastic membrane labeled in the figure. The precessional movement damps out because it works the membrane back and forth against the tension in the wires, which are extended under centrifugal force. The elastic constants of the membrane may be selected for proper impedance matching so that the precession damps as rapidly as possible. The first stage despin is less efficient than the yo-yo mechanism; in particular it cannot stop or reverse the spin. However, this is of minor concern, since its main function is to ensure that the craft is not precessing when the yo-yo weights release. The formula for the first stage despin is given on the figure.

There are innumerable ways in which two sets of despin wires and two sets of solar vanes can become entangled. Therefore, we suggest a launch configuration in which the vanes are initially folded and the

FIRST
STAGE
DESPIN



$$\frac{\omega_e}{\omega_i} = \frac{I_i}{I_e}$$

i - WIRES IN
e - WIRES EXTENDED

SECOND
STAGE Yo-Yo
DESPIN

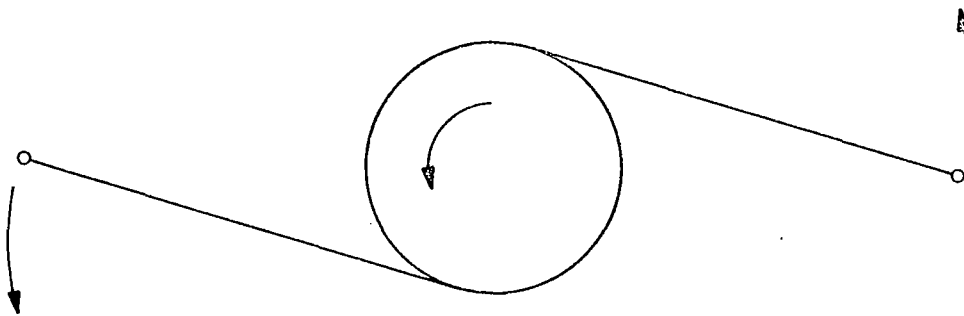


Figure 55 Two stage despin mechanism

spacecraft is enclosed in a cylindrical container with the two-stage despin mechanisms on the outside of the container. After injection the following sequence then takes place. The first stage despin wires extend and plenty of time is allowed for the precession to damp, days if necessary. Next the first stage wires are released followed quickly by the yo-yo wires. This drops the spin rate to the range of $1/2$ to 2 rpm. In this condition a suitable spring loaded mechanism is activated to push the payload out of its container and extend the various vanes in a sequence carefully planned to prevent them from snagging one another. This leaves the spacecraft in a condition that is ready to track the Sun as soon as it points at the Sun, although initially it points in the wrong direction.

Sun acquisition probably requires active control of the pitch of the vanes by means of an electric motor, which will not be used after the acquisition phase. Fig. 56 is a view that would be seen by an observer at the Sun. It shows the pitch of the vanes required to precess the spacecraft toward the Sun. This figure is a bit difficult to visualize; the pitch is like that of a fan blowing air to the right. The pitch is sufficiently great that the back sides of the two vanes at the bottom of the figure are exposed to the sunlight, while the fronts of the other vanes are sunlit. The various vectors for sun rays, force, angular momentum and torque are self-explanatory when the X marks are interpreted as vectors pointing into the plane of the paper, and a circled dot is interpreted as a vector pointing out of the paper. As the spin axis precesses toward the Sun it is necessary to adjust the pitch of the vanes instantaneously at the bottom of the figure, and the front side of the vanes at the top of the figure.

When the axis finally points close enough to the Sun, the front set of vanes will shade a significant portion of the back set of vanes. Then the active control of the pitch is no longer needed, and the vanes may be set and left in their steady state condition with nominally zero pitch on the front ones. A more detailed study of this sun acquisition system is needed, but from the present preliminary results it seems that active control of a single variable will suffice, namely the pitch angle of all vanes, which may be geared together to change pitch when driven by a single motor. We emphasize that this motor will never be used after sun acquisition and so its life is not a factor in the longevity of the spacecraft.

Comparison to Other Attitude Control Schemes

We are aware of only two other attitude control schemes which have been suggested and partially analyzed in the course of MIT Sunblazer studies. In this subsection we show evidence that our technique is superior to both of these. The first would employ active attitude control

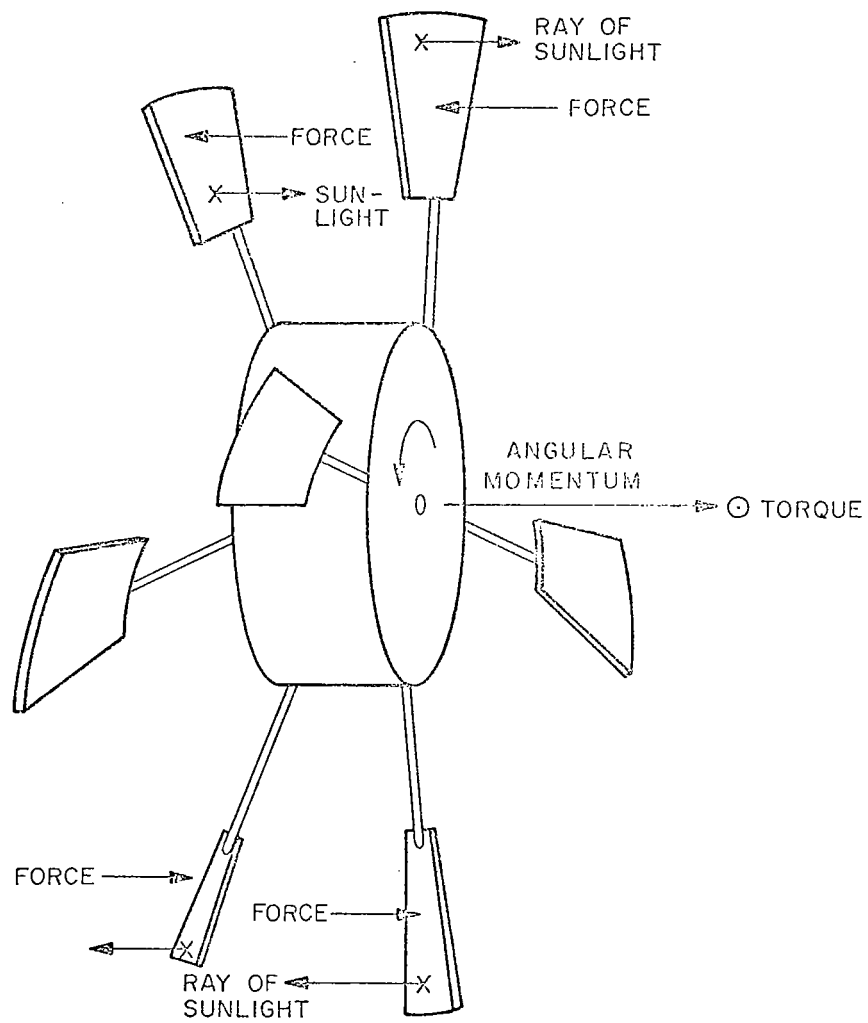


Figure 56 Spacecraft force/angular momentum vectors

of a spinning spacecraft. The scheme resembles ours except that there is only one set of vanes and no partial shading. The spacecraft would monitor the lag angle θ to the Sun, and when θ exceeds some threshold, the craft automatically adjusts the pitch of the vanes in a manner that precesses the spin axis toward the Sun. The main problem with this scheme may be seen by referring to Fig. 54 and imagining that the back vanes are missing. Consider the two vanes at the top and bottom of the front view. The required control must cause the solar pressure into the plane of the paper to be greater on the top vane than on the bottom one. Therefore each vane has at least two orientations, one with large and one with small projected area. But these vanes are continuously trading places as the spacecraft rotates, and so the active control mechanism must tilt each vane from one position to the other at least twice each revolution of the spacecraft. That is, each vane position cycles at a rate on the order of once or twice per minute. Note that this attitude control system resembles that of a helicopter. Clearly a motor producing this much movement year in and year out is a liability to the life of the spacecraft. Moreover, as the vanes move, the solar pressure on the spacecraft as a whole is constantly changing in a manner that would make it practically impossible to accurately estimate the effects of solar pressure on the orbit. Hence precision orbit determination is sacrificed in this attitude control scheme.

The only other attitude control system of which we are aware is those that would eliminate spin stabilization and orient the spacecraft toward the Sun in the manner that a weather vane points into the wind. In other words this scheme employs some form of sail or tail behind the spacecraft. The tail would have to employ some form of dissipative movement, since, like a pendulum, the motion toward equilibrium is governed by a second order differential equation and the spacecraft will swing past the equilibrium position over and over in an oscillation that must be damped. By contrast the spinning systems enjoy an important advantage: their attitude control is governed by a first order differential equation; i. e., Eq. (1) involves a first rather than a second derivative with respect to time. This means that the restoring motion, the precession of the axis, stops dead in its tracks the moment the torque vanishes at the equilibrium position in which the spacecraft's axis points directly at the Sun. The motion exhibits no tendency to coast past equilibrium as is the case with the weather-vane stabilization.

The really severe problem for the nonspinning system is how to maintain zero spin for a long period of time once it has been achieved. Small errors in the shape and reflectivity of various parts of the spacecraft will have the effect of a residual propeller pitch and will cause the spacecraft to spin up slowly in one direction or the other. The maximum amount of residual spin that is tolerable before the spacecraft begins to be spin stabilized and ceases to function as a weather vane is given by

$$\omega < \frac{2I}{I_1} \sqrt{\ddot{\theta}_{\max}} ,$$

where I is the moment of inertia about axes perpendicular to the roll axis, and $\ddot{\theta}_{\max}$ is the maximum angular acceleration of the spacecraft as it executes its pendulum motion about the equilibrium position. With a reasonable set of assumptions about the spacecraft the right side of this inequality was evaluated as 0.066 rpm. This is an order of magnitude more severe limitation than the tolerance discussed above for a spinning spacecraft.

The nonspinning or weather-vane configuration faces further complications, since a ratio of inertial moments suitable for despin is not suitable in the steady state. Recall that the roll moment should be the largest of the three during precession damping and despin. However, when the tail (sail) is deployed, the other moments are likely to be larger, say $I_1/I = 3$. This means that the tail must be deployed after despin, especially since the tail includes some form of damping. Thus the sun acquisition sequence for the weather-vane configuration is about as complex as unfolding the vanes for a spinning attitude control system; although it may seem simpler at first thought.

A final and important disadvantage of the nonspinning system is the fact that the angular position of the craft about its roll axis is indeterminate. This implies an unknown orientation of various sensors or experiments in the spacecraft that may be measuring anisotropic properties of the interplanetary medium, or Faraday rotation of the polarization of a radio signal in the solar probe case. In its equilibrium position the nonspinning spacecraft is pointed directly at the center of the Sun's disc, so a sun sensor is of no value in determining the roll angle. Even in missions without Faraday rotation the polarization angle of a linearly polarized signal has little value as a roll angle indicator, because this angle is ambiguous by 180° . By contrast the axis of a spinning spacecraft always lags behind the changing angular position of the Sun by the angle θ of Eqs. (36) and (37). In that case a solar sensor may be used to read apparent sun position, from which a logic circuit determines and telemeters the information on instantaneous orientation about the roll axis.

A spin-stabilized spacecraft could even employ a high-gain transmitting antenna on the telemetry downlink*, provided that communications on a short duty cycle once each rotation is acceptable. To the craft, the line-of-sight to Earth appears to move in a cone about its axis (like stars about the North Star). An antenna cocked off axis by the half-angle of this cone will point at the Earth once each rotation.

*High gain is not necessary or desirable for the uplink.

RECOMMENDED MISSION

The recommended mission is one employing S and X-band uplinks over an extended period of time, i. e., years, and employing at least one and preferably a few spacecraft. Whenever possible more than one spacecraft at different path offsets from the Sun should be tracked so that solar events can be clocked as they pass from one line-of-sight to the other.

The duration and number of spacecraft surely involves scheduling conflicts, so as many groups as possible spaced around the world should participate. Eighty-five foot antennas and 10 kw transmitters, or equivalent capability, suffices to qualify a facility.

An orbit similar to the December (Fig. 3)or February launch (June or August superior conjunction) orbits of Sunblazer are recommended. At least one spacecraft should have an orbit that takes it as far as possible out of the ecliptic plane, even though the payload has to be simplified, and capability sacrificed to lighten the craft. Alternatively, a more powerful booster than the Scout could be used at greater expense.

The spacecraft per se should have the form shown in Fig. 54 for stable passive attitude control. The vanes will be covered with solar cells and the front face will have antennas for the following functions:

- S-band uplink, omni and 20 db
- X-band uplink, 20 db
- X-band telemetry downlink.

The omnidirectional antennas are for the times before and after superior conjunction when the Earth is not within the 11° beam of the 20 db antennas. For launch and despin, the vanes should be folded and spacecraft enclosed in a suitable container. The two stages of despin shown in Fig. 55 should be part of this container. After injection and despin, the container is discarded. Before the final phase of passive attitude control, there is a phase lasting about 2 weeks or less in which the vanes are positioned on command to precess the spacecraft into its final Sun-oriented attitude.

The payload weight should be allotted to the following functions:

- S-band receiver
- X-band receiver
- X-band transmitter
- Power system
- Housekeeping functions, i. e., thermal control, etc.
- Roll axis angle sensor (based on Sun sensor)
- Data reduction
- Data storage and retrieval.

Temptations to add more experiments should be resisted; i. e., this is a dedicated spacecraft, and even the closely related general relativity experiment should not be allowed to compete for weight. Any surplus in unallotted weight should not be assigned; rather a lighter spacecraft should be launched into an orbit further out of the ecliptic plane.

Data storage in a memory core is required for two reasons. First, the weak downlink for telemetry requires a formidable ground antenna, usually an 85' paraboloid, but a 210' is required near conjunction. It is most unlikely that a world-wide net of these can be made available to maintain continuous track. Second, the telemetry link probably will be interrupted at conjunction (passage behind the Sun) before the experimental uplink is interrupted.

The data reduction logic deserves much attention and a sizable weight allotment. The logic must interpret, and telemetry must fully describe, a wide variety of corona parameters and solar events, since the investigators on the ground have no other access to the data. The following list gives desirable data reduction functions.

- Average statistical moments of the signal strength and phase of the carrier and its modulations.
- Polarization data.
- Time at which rare events occurred as determined by exceeding various thresholds in the derivatives of signal strength and phase.
- Special modes for special experiments such as the interferometer lobes sweeping across the craft.
- Samples of raw data recorded for transmission at a reduced rate, especially samples of rare events or loss of S-band phase-lock behind the Sun.

APPENDIX 1

DERIVATION OF PULSE RISE TIME CAUSED BY PLASMA DISPERSION

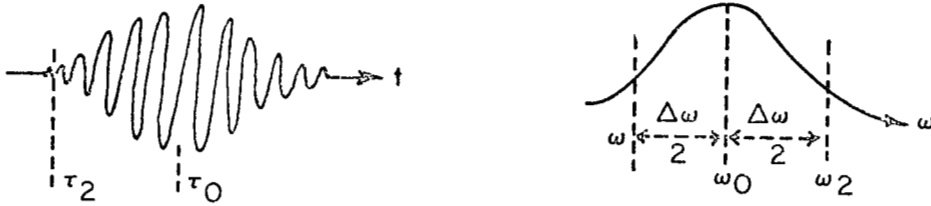
The phase of the signal pulse after traversing a path length z is

$$\phi(\omega) = \frac{\omega n(\omega) z}{c} \quad (40)$$

with

$$n = \sqrt{\epsilon} = \sqrt{1 - \omega_p^2 / \omega^2}$$

In the regime $\omega > \omega_p$, although the received dispersed pulse exhibits unknown bandwidth $\Delta\omega$, the rise time can be calculated as the difference between arrival times of the bulk of the energy and the precursor contribution.



The former is the time of arrival, τ_0 , of the group of frequencies centered around the carrier, ω_0 . The latter, τ_2 , is made up by the incremental group of frequencies that travel the fastest, namely the ones at the upper end of the spectrum, $\omega_0 + \Delta\omega/2$. Since arrival time is the derivative of phase, the rise time is

$$\tau = \tau_0 - \tau_2 = \phi'(\omega_0) - \phi'(\omega_0 + \Delta\omega/2) \quad (41)$$

Note that $\omega_0 + \Delta\omega/2$ corresponds to the high frequency portion of the pulse spectrum since this incremental group travels with the highest group velocity. Expanding $\phi'(\omega_0 + \Delta\omega/2)$ up to second derivative yields

$$\tau = -\phi''(\omega_0) \Delta\omega/2 = -\pi\phi''(\omega_0)\Delta f \quad (42)$$

Rise time and pulse bandwidth are related by

$$\Delta f = 1/\tau \quad (43)$$

so

$$\tau = \sqrt{-\pi \phi''(\omega_o)} = \sqrt{\frac{\pi z}{c \omega_p} \frac{1}{\left(\omega_o^2/\omega_p^2 - 1\right)^{3/2}}} \quad (44)$$

At frequencies above 10 MHz

$$\left(\frac{\omega_o}{\omega_p}\right)^2 \gg 1 \quad (45)$$

Equation (44) reduces to

$$\tau^2 = \frac{z}{2c} \frac{f_p^2}{f_o^3} \quad (46)$$

f_p is a function of electron density and is given as

$$f_p = 81 N_e \left(\frac{m^{-3}}{\text{sec}} \right) \quad (47)$$

Since we are interested in integrated electron density (el/m² for a given path) we substitute Eq. (47) into Eq. (46) and integrate along the propagation path

$$\tau^2 = \frac{1}{2c f_o^3} \int N_e d\ell \quad (48)$$

The electron density within 20 radii is given as

$$N_e \approx \frac{10^{12}}{p^2} m^{-3} \quad (49)$$

where p = radial offset from the Sun in solrads, as usual

$$d\ell = r_o \frac{p dp}{\sqrt{p^2 - b^2}} \quad (50)$$

where r_o = Sun radius in m

b = perpendicular path offset in solrads

Substituting Eq. (49) in Eq. (48) and integrating yields channel limited pulse rise time

$$\tau = \frac{1.38 \times 10^7}{f_o^{3/2}} \sqrt{\frac{\cos^{-1}\left(\frac{b}{215}\right)}{b}} \quad (51)$$

APPENDIX 2

INTEGRATED ELECTRON DENSITY

The electron density as a function of radial offset from the Sun in solrads is given as

$$N_e \approx \frac{10^{12}}{p^2} \text{ (el/m}^3\text{)} \quad (52)$$

Integrated electron density is given as:

$$I = \int N_e d\ell \quad (53)$$

where $d\ell = r_o \frac{p dp}{\sqrt{p^2 - b^2}}$

r_o = Sun radius in m

b = perpendicular path offset in solrads

Substituting Eq. (53) in Eq. (52) yields

$$I = 1.4 \times 10^{21} \frac{\cos^{-1}\left(\frac{b}{215}\right)}{b} \quad (54)$$

I is plotted in Fig. 57

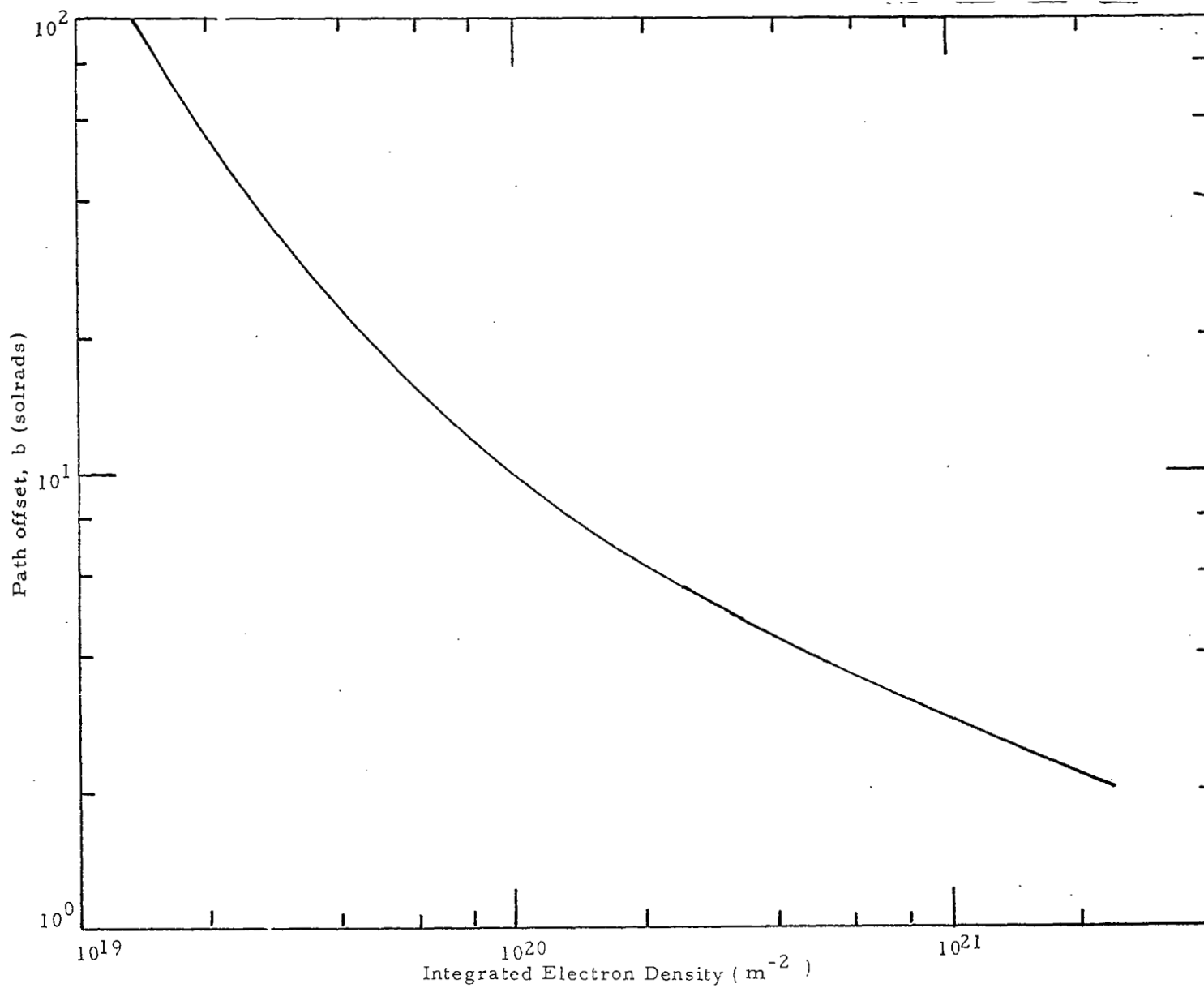


Figure 57 Integrated electron density vs. path offset

APPENDIX 3

ANGULAR ENERGY DISTRIBUTION IN THE LARGE SCATTERING REGIME

We show that for large scattering, $\Phi_0 \gg 1$, most of the energy is concentrated in the higher diffraction orders, m according to the relation

$$\frac{1}{\left(1 - \frac{m^2}{2}\right)^{\frac{1}{4}} \Phi_0}$$

We start off by expressing the amplitude of the m -th order in integral form,

$$J_m(\Phi_0) = \frac{1}{2\pi} \int_0^{2\pi} \cos \Phi_0 \left(\sin \theta - \frac{m}{\Phi_0} \right) d\theta = \frac{1}{2\pi} \int_0^{2\pi} \cos [\Phi_0 f(\theta)] d\theta \quad (55)$$

Since $\Phi_0 \gg 1$, $\cos [\Phi_0 f(\theta)]$ oscillates rapidly. Integral (55) is significant near stationary values $\theta = \theta_s$ where $f'(\theta_s) = 0$. The following functions are used in the development,

$$f(\theta) = \sin \theta - \frac{m}{\Phi_0}$$

$$f'(\theta_s) = \cos \theta_s - \frac{m}{\Phi_0} = 0 \quad \text{yields two stationary values}$$

$$\theta_s = \pm \cos^{-1} \frac{m}{\Phi_0}$$

$$f''(\theta_s) = -\sin \theta_s = \pm \sqrt{1 - \frac{m^2}{\Phi_0^2}}$$

We now expand $f(\theta)$ to second order

$$f(\theta) = f(\theta_s) + f''(\theta_s) \frac{(\theta - \theta_s)^2}{2} \quad (56)$$

so that

$$\begin{aligned} \cos [\Phi_0 f(\theta)] &= \cos [\Phi_0 f(\theta_s)] \cos \left[\Phi_0 f''(\theta_s) \frac{(\theta - \theta_s)^2}{2} \right] \\ &\quad - \sin [\Phi_0 f(\theta_s)] \sin \left[\Phi_0 f''(\theta_s) \frac{(\theta - \theta_s)^2}{2} \right] \end{aligned}$$

change variable

$$\sqrt{\frac{\Phi_0 f''(\theta_s)}{2}} (\theta - \theta_s) = u$$

and (55) becomes, after extending limits to ∞ since $\Phi_0 \gg 1$,

$$J_m(\Phi_0) = \frac{1}{2\pi} \cos[\Phi_0 f(\rho_s)] \sqrt{\frac{2}{\Phi_0 f'''(\theta_s)}} \int_{-\infty}^{\infty} \cos u^2 du - \frac{1}{2\pi} \sin[\Phi_0 f(\rho_s)] \sqrt{\frac{2}{\Phi_0 f'''(\theta_s)}} \int_{-\infty}^{\infty} \sin^2 u du \quad (57)$$

Contribution from the two stationary values are included within those limits. Note that terms in (57) go as $1/\sqrt{\Phi_0}$. Had we retained the next higher order term $(\theta - \rho)^3$ in Taylor's expansion (56) additional terms in (57) would decay as $(1/\sqrt{\Phi_0})^2$.

The well-known Fresnel's integrals

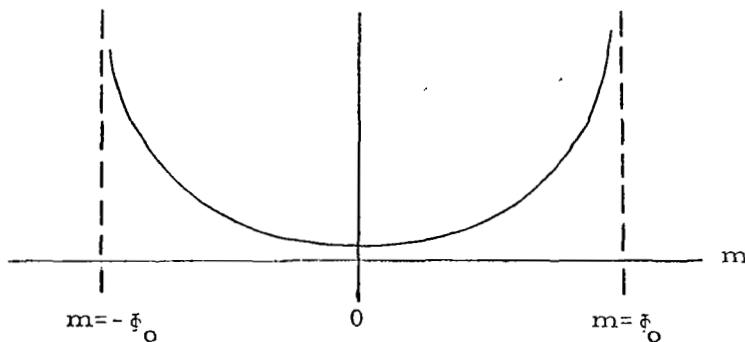
$$\int_{-\infty}^{\infty} \cos^2 u du = \int_{-\infty}^{\infty} \sin^2 u du = \sqrt{\pi/2}$$

yields after substitution in (57)

$$J_m(\theta_0) = \frac{1}{2} \sqrt{\frac{\pi}{\Phi_0}} \frac{\cos[\Phi_0 f(\rho_s)] - \sin[\Phi_0 f(\rho_s)]}{\sqrt{f'''(\theta_s) - (1 - m^2/\Phi_0^2)^{\frac{1}{4}}}} \quad (58)$$

The envelope of $J_m(\Phi_0)$ varies as $\frac{1}{(1 - \frac{m^2}{\Phi_0^2})^{\frac{1}{4}}}$

and is sketched below



APPENDIX 4

PHASE JITTER BANDWIDTH

The frequency fluctuations or phase jitter bandwidth are caused by the random changes in phase path length that occur over a coherence time. The coherence time is the time during which the random phase function discussed in Sec. 4.2 is correlated. The coherence time is of the order of the time it takes for a blob of size a and velocity u normal to the propagation path to cross that path, i. e., $T_c \sim \frac{a}{u}$.

The jitter bandwidth B is easily derived if we assume the following ρ dependence [Ref. 24, 25] of u and a to hold over the entire integration path. We choose the following expressions

$$\begin{aligned} u &= 14 \times \rho^{1.25} \text{ Km/sec} \\ a &= 1.17 \rho^{1.05} \text{ Km} \\ \langle \Delta N_e^2 \rangle &= 13.1 \times 10^8 \rho^{-5.14} \text{ cm}^{-6} \end{aligned}$$

which substituted in

$$B^2 \approx \frac{\omega_o^2}{T_c^2} = \frac{K^2 \pi^2}{c^2 f^2} \int \frac{u^2 \langle \Delta N_e^2 \rangle}{a} df \quad (59)$$

yield after integration,

$$B(\text{Hz}) = \frac{23}{f(\text{GHz}) b^{1.35}} \quad (60)$$

The integration procedure is identical with the one used in the angular scintillation calculation. Recall the limited validity of this expression, since it is based on scale size models for a which do not extend below $b = 8$. The plot for u in Fig. 58 shows rapid change in velocity as we approach closer to the Sun. We would expect analogous changes for a , so if we apply expression (2) at offset distances b smaller than 8 we underestimate the phase bandwidth jitter by possibly an order of magnitude. This is well confirmed by Fig. 24 in the text which compares theoretical prediction based on the above expression against Pioneer and Mariner's data.

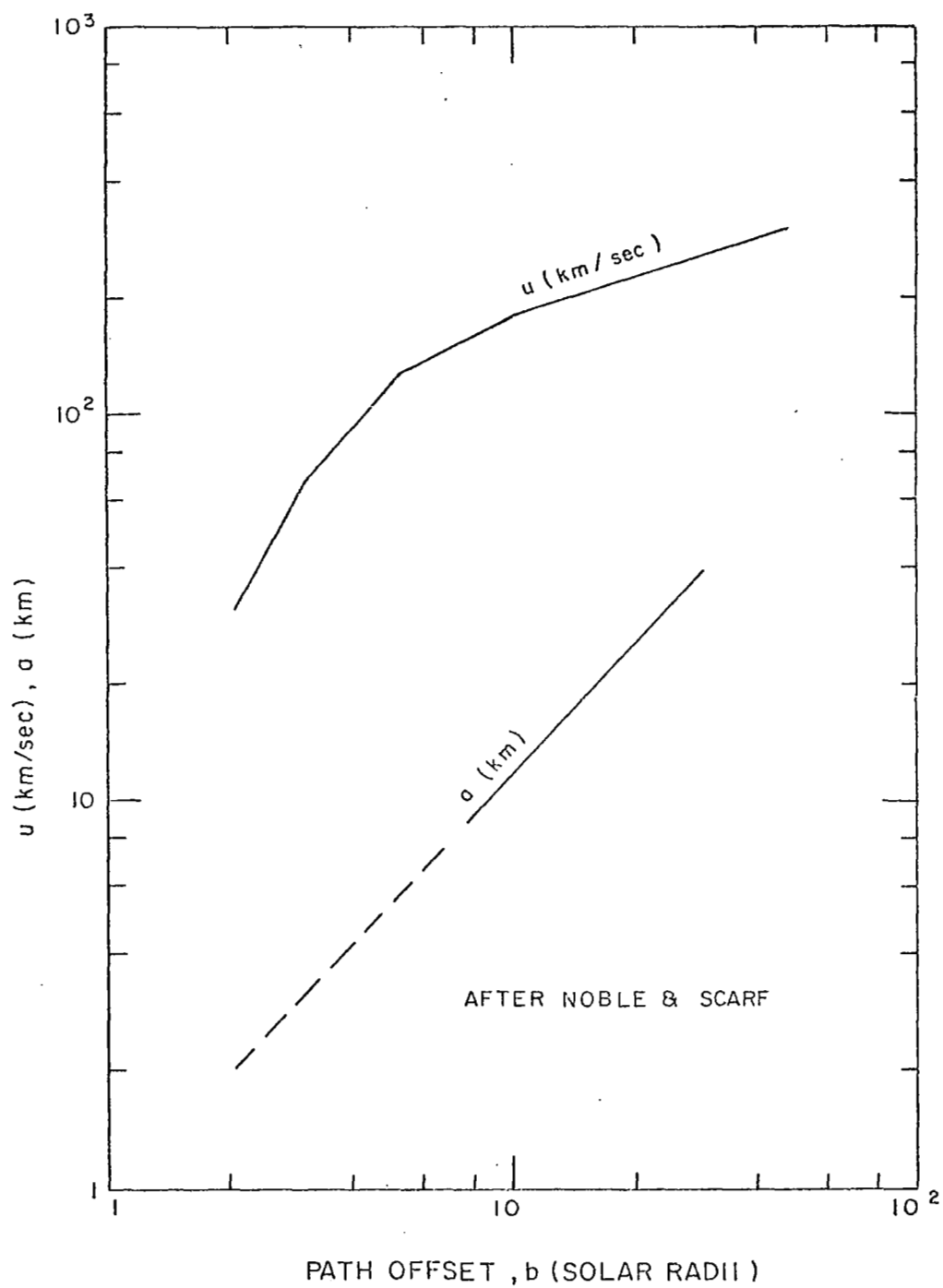


Figure 58

APPENDIX 5

Angular Scattering

Consider a blob having a diameter (correlation length) a and refractive index less than average by an amount Δn . A wavefront through the center is advanced a distance of $a\Delta n$ relative to the ray that barely misses the bulk of the blob. Therefore the angular deviation for one blob $\Delta\theta_1$ is about $a\Delta n/(a/2) = 2\Delta n$. The coefficient 2 is by no means exact. It depends on unknown details about the shape of blobs and how their density tapers off.

To analyze the deviation of a ray that passes through many blobs, we can add the variances $\langle \Delta\theta_1^2 \rangle$ along the path, since the directions of the deviations are random and since very small rotations act like vectors in that components may be added. The blobs are generally assumed to be dense, so there are about $\Delta x/a$ of them in a distance Δx along a ray. Integrating along a ray passing through the whole corona we find

$$\langle \Delta\theta^2 \rangle = \int \langle \Delta\theta_1^2 \rangle \frac{dx}{a} = 4 \int \frac{\langle \Delta n^2 \rangle}{a} dx \quad (1)$$

Both $\langle \Delta n^2 \rangle$ and a in Eq. (1) are functions of ρ , the distance from the Sun to a general point along the line-of-sight as shown in Fig. 1 in the text.

Next the refractive index n must be expressed in terms of N_e the electron density, since n depends on the frequency f as well as the property of the corona. The relation is

$$n^2 = 1 - \frac{KN_e}{f^2}, \quad \text{where } K = 80.6 \times 10^{-6}$$

N_e is in cm^{-3} , and f in MHz. Differentiating $(1 - \frac{KN_e}{f^2})^{1/2}$ gives approximately

$$\Delta n \approx -\frac{K\Delta N_e}{2f^2}, \quad (2)$$

which in turn gives

$$\langle \Delta\theta^2 \rangle \approx \frac{K^2}{f^4} \int \frac{\langle \Delta N_e^2 \rangle}{a} dx$$

when Eq. (2) is substituted in Eq. (1). Let us change the integration variable from x to ρ , since $\langle \Delta N_e^2 \rangle$ and a are simple functions of ρ .

$$x = (\rho^2 - b^2)^{1/2}, \quad dx = \rho(\rho^2 - b^2)^{-1/2} d\rho,$$

$$\langle \Delta \theta^2 \rangle = \frac{2K^2}{f^4} \int_1^\infty \frac{\langle [\Delta N_e(\rho)]^2 \rangle}{a(\rho)(\rho^2 - b^2)^{\frac{1}{2}}} \rho d\rho \quad (3)$$

where the 2 comes from integrating only over half the symmetrical path, Fig 1, and the upper limit was called infinity merely to say that the outer reaches of the corona are unmeasurable, and therefore the exact upper limit is unimportant.

Cohen and Gundermann [Ref. 25] give a and $\text{rms } \Delta N_e$ as functions of ρ , their Eqs. (5) and (9), which read

$$a(\rho) = \begin{cases} 1.17 \text{ km } \rho^{1.05} = 1.68 \times 10^{-6} \text{ sol. rad. } \rho^{1.05}, & \rho < 30 \\ 6.35 \text{ km } \rho^{0.55} = 9.13 \times 10^{-6} \text{ sol. rad. } \rho^{0.55}, & \rho > 30 \end{cases}$$

$$\Delta N_e(\text{rms}) = \begin{cases} 10.4 \times 10^3 \text{ cm}^{-3} \rho^{-2.08}, & 8 < \rho < 30 \\ 4.43 \times 10^3 \text{ cm}^{-3} \rho^{-1.83}, & 30 < \rho < 40 \end{cases}$$

where ρ is distance measured in solar radii. With these empirical formulas we readily evaluate the quantity $\rho \langle N_e^2 \rangle / a$ in the integrand of Eq. (3):

$$10^{12} \begin{cases} 64.4 \rho^{-4.21}, & \rho < 30 \\ 2.15 \rho^{-3.21}, & 30 < \rho < 40 \end{cases}$$

For ease of integration, we changed to another empirical form,

$$\frac{\rho \langle \Delta N_e^2 \rangle}{a} = 10^{12} \left(\frac{64.4}{\rho^{4.21}} + \frac{0.31}{\rho^{3.21}} \right), \text{ all } \rho,$$

which has the added advantage of making a smooth fit at $\rho = 30$. Using the integral identity

$$\int_b^\infty \frac{dt}{t^p \sqrt{t^2 - b^2}} = \frac{\sqrt{\pi}}{2} \frac{\Gamma(\rho/2)}{\Gamma((\rho+1)/2)} \frac{1}{b^\rho},$$

we find

$$\Delta \theta(\text{rms}) = \frac{107.84}{f^2} \left(\frac{47.1}{b^{4.21}} + \frac{0.27}{b^{3.21}} \right)^{\frac{1}{2}},$$

where f is in MHz, $\Delta \theta$ in radian, and b is in solar radii.

REFERENCES

1. Brandt, J. C.: *Ann. Rev. Astron. & Ap.*, vol. 6, 1968, p. 267.
2. Parker, E. N.: *Space Sci. Revs.*, vol. 9, May 1969, p. 325.
3. Parker, E. N.: *Space Sci. Revs.*, vol. 4, 1965, p. 666.
4. Axford, W. I.: *Observations of Interplanetary Plasma. Space Sci. Rev.*, vol. 8, 1968, pp. 331-365.
5. Ness, Norman F.: *Observed Properties of the Interplanetary Plasma. Annual Review of Astronomy and Astrophysics*, vol. 6, 1968, pp. 79-114.
6. Allen, C. W.: *Astrophysical Quantities. Second ed.*, Athlone Press, London, 1963.
7. Ney, E. P.; Huch, W. F.; Kellogg, P. J.; Stein, W.; and Gicell, F.: *Ap. J.*, vol. 133, 1961, p. 616.
8. Neugebauer, M.; and Snyder, C. W.: *Ann. Rev. Astron. Ap.*, vol. 5, 1967, pp. 213-266.
9. McCracken, K. G.; and Ness, N. F.: *J. Geophys. Res.*, vol. 71, 1966, p. 13.
10. Strong, I. B.; Asbridge, J. R.; Bame, S. J.; and Hundhausen, A. J.: *Trans. Am. Geophys. Union*, vol. 48, 1967, p. 191.
11. Brandt, J. C.: *Ap. J.*, vol. 144, 1966, pp. 1221-1222.
12. Ness, N. F.; and Wilcox, J. M.: *Phys. Rev. Ltrs.*, vol. 13, 1964, pp. 461-464.
13. Wolfe, J. H.; Silva, R. W.; and Myers, M. A.: *J. Geophys. Res.*, vol. 71, 1966, pp. 1319-1340.
14. Pai, L. G.; Bridge, H. S.; and Lyon, F. F.: *Trans. Am. Geophys. Union*, vol. 48, 1967, p. 176.
15. Erickson, W. C.: *Ap. J.*, vol. 139, 1964, pp. 1290-1311.
16. James, J. C.: Chap. 7 in *Radar Astronomy*, ed. by J. V. Evans & Tor Hagfors, McGraw-Hill, New York, 1968.
17. Bohlin, J. D.; Hansen, R. T.; and Newkirk, G. A., Paper presented at October meeting A. A. S., 1966.

18. Newkirk, Gordon, Jr.: Structure of the Solar Corona. Annual Review of Astronomy and Astrophysics, vol. 5, 1967, pp. 213-266.
19. Whang, Y. C.; Liu, C. K.; and Chang, C. C.: Ap. J., vol. 145, 1966, p. 255.
20. Wyndham, J. E.: in The Solar Wind, Jet Propulsion Lab. and Calif. Inst. Tech., Pasadena, pp. 109-122, 1966.
21. Slec, O. B.: Monthly Notices Roy. Astron. Soc., vol. 123, 1961, p. 223.
22. Malitson, H. H.; Erickson, W. C.: Ap. J., vol. 144, 1966, pp. 337-351.
23. Hewish, A.: Mon. Notices Roy. Astron. Soc., vol. 118, 1958, p. 534.
24. Hewish, A.; and Symonds, M. D.: Planet. Space Sci., vol. 17, 1969, p. 313.
25. Cohen, M. H.; and Gunderman, E. J.: Interplanetary Scintillations IV. Observations Near the Sun. Astrophys. J., vol. 155, Feb. 1969, p. 645.
26. Salpeter, E. E.: Astrophys. J., vol. 147, 1967, p. 433.
27. Cohen, M. H.; Gunderman, E. J.; Hardebeck, H. E.; and Sharp, L. E.: Astrophys. J., vol. 147, 1967, p. 449.
28. Dennison, P. A.; and Hewish, A.: Nature, vol. 213, 1967, p. 343.
29. Campbell, D. B.; and Muhleman, D. O.: J. Geophys. Res., vol. 5, March 1, 1969, p. 1138.
30. Levy, G. S.; Sato, T.; Seidel, B. L.; Stelzried, C. T.; Ohlson, J. E.; and Rusch, W. V. T.: Pioneer VI Faraday-Rotation Solar-Occultation Experiment. Science, vol. 166, Oct. 31, 1969, pp. 596-598.
31. Goldstein, R. M.: The Superior Conjunction of Pioneer VI. Science, vol. 166, Oct. 31, 1969, pp. 598-601.
32. Goldstein, R. M.; et al: The Superior Conjunction of Mariner IV. Technical Report 32-1092, Jet Propulsion Lab., Pasadena, California, April 1, 1967. (Available as NASA CR-83957.)

33. Koehler, Richard L.: Radio Propagation Measurements of Pulsed Plasma Streams from the Sun Using Pioneer Spacecraft. J. Geophys. Res., Space Physics, vol. 73, August 1, 1968, p. 4883.
34. Eshleman, E. V.: Science, vol. 158, 1967, p. 585.
35. Little, A.; and Hewish, A.: Monthly Notices Roy. Astron. Soc., vol. 34, 1966, p. 221.
36. Kraus, John D.: Radio Astronomy. McGraw-Hill, New York, 1966.